

---

# A Mechanistic Study of Tabular Foundation Models

---

Marin Biloš, James T. Wilson, Anderson Schneider, Yuriy Nevmyvaka  
Machine Learning Research, Morgan Stanley  
{firstName.lastName}@morganstanley.com

## Abstract

Tabular foundation models with different architectures converge in accuracy across a range of classification and regression tasks. This raises questions a leaderboard cannot answer: (i) whether the models execute the same in-context algorithm, (ii) where row, column, and class-permutation invariances originate, and (iii) how robust they are under perturbations engineered against the inferred mechanism. We characterize all three. The model families realize qualitatively distinct similarity-based readouts: from an attention-weighted vote over context labels to a class-conditional mean readout, each confirmed by causal intervention. We find that the representation collapse highlighted in prior work is not a practical concern for them. Each model’s permutation invariances trace to specific positional parameters whose removal preserves accuracy and makes approximate invariance exact. Perturbations engineered against each readout reproduce predicted failure modes; hub and rank attacks isolate them from refit baselines. Together these results give a mechanistic account of contemporary tabular foundation models and identify which inductive biases govern both their accuracy and characteristic failures.

## 1 Introduction

Tabular foundation models such as TabPFNv2 [Hollmann et al., 2025], TabICLv2 [Qu et al., 2025], and Mitra [Zhang et al., 2025] match or surpass specialized models on tabular classification and regression without task-specific training. Given a labeled table at inference time, each model predicts labels for held-out query rows entirely through in-context learning [Dong et al., 2024]. All three are transformer-based [Vaswani et al., 2017] and reach comparable benchmark accuracy despite differing substantially in architecture. This convergence leaves open mechanistic questions.

First, since the architectures differ in non-trivial ways, we ask whether the learned in-context algorithm is shared. We find that each model forms its prediction at a qualitatively different depth and through a mechanistically distinct readout—the way each model turns its internal representations into a prediction (§2). These recipes are implemented in different parts of each network and are only partly interchangeable across backbones: transplanting one’s readout onto another collapses accuracy (§3).

A second question concerns a property any tabular model should have: reordering rows or columns or renaming the classes should not change the prediction. No model enforces this by construction, yet we isolate the architectural components that break each symmetry and show that the pretrained models have largely learned to ignore them. Simple surgical edits restore exact invariance at no cost to accuracy, and large-scale pretraining experiments further contextualize how invariance interacts with accuracy (§4). We also revisit the representation collapse concern from Qu et al. [2025] and find it does not materially affect the released models. We prove a fundamental expressiveness barrier for column-invariant architectures on collapse-prone data, then validate this with minimal prototype models and stress tests on the released models. We find that each model’s architectural mitigations sidestep the failure mode in practice (§5).

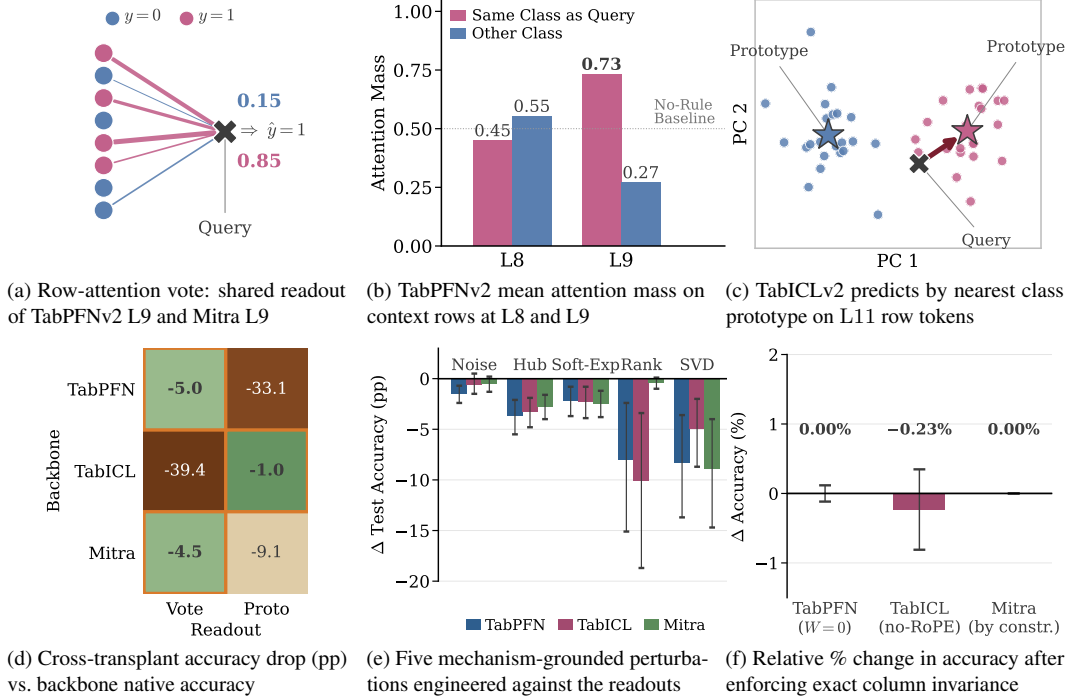


Figure 1: **Subset of results.** *Illustration of readout mechanisms:* (a) attention-weighted vote for TabPFNv2 and Mitra, both on layer 9; (b) TabPFNv2 L9 puts most of its attention mass on same-class context rows; (c) nearest class prototype for TabICLv2, at L11. *Causal evidence:* (d) each backbone’s native readout stays within a few pp of end-to-end accuracy, while cross-backbone readouts collapse; (e) five mechanism-grounded perturbations engineered against these models cut test accuracy; (f) enforcing exact column-permutation invariance does not change the accuracy on all three backbones.

Finally, we turn the mechanistic findings into targeted attacks. We design data perturbations that should be invisible to a sensible learner but strike the specific machinery each model relies on, exposing distinct, readout-specific weaknesses that confirm the mechanistic picture (§6).

Together, these results show that models which score alike on benchmarks disagree on how they form predictions, which symmetries they respect, and where they break under pressure. The audit surfaces many additional findings along the way; among them, that some models have a large number of layers that carry little load and can be removed without hurting accuracy (§2). Many of our results apply directly to existing checkpoints, from restoring exact invariance to diagnosing fragilities, while the patterns that emerge across the three families offer concrete guidance for designing future tabular foundation models with stronger invariances and fewer redundant components.

**Related work.** The three architectures we audit, per-cell attention (TabPFNv2), row-token attention (TabICLv2), and a factorized label-slot design (Mitra), span the dedicated-architecture tabular foundation model class and set the current SOTA [Landgesell and Knoll, 2026]; LLM-based tabular models [Sui et al., 2024] inherit a textual prior rather than a tabular one, and same-architecture retrains on real data [Ma et al., 2025] reuse a backbone we already audit. Prior empirical work on these models is limited: [McElfresh et al., 2023] catalogues their permutation invariances without locating the responsible parameters, [Gupta et al., 2026] traces task-relevant logic into the middle layers, and Hu and Ghelichi [2025] maps signal-vs-noise separation in late TabPFNv2 layers on synthetic tasks. We work on more families, datasets, and interventions than prior work, pinning down what current models actually do and flagging design choices for future work.

In-context learning has been cast as gradient descent [Von Oswald et al., 2023, Akyürek et al., 2023], Bayesian inference under a prior [Müller et al., 2022], or function-class learning [Garg et al., 2022]; our recipes (§3) make precise which view each backbone instantiates. The expressiveness limit we use in §5 builds on the permutation-invariance bottleneck of set and context-based architectures [Zaheer et al., 2017, Garnelo et al., 2018], applied here to the column-permutation case.

## 2 Where representations form

The goal of this section is to locate, layer by layer, where each model builds representations that carry enough class information for a simple classifier to read off the answer.

All three models process a table formed by labeled context rows and unlabeled query rows. TabPFNv2 [Hollmann et al., 2025] treats each cell of this table as a separate token: its 12-block stack alternates row-wise attention (mixing information across rows within each column) with column-wise attention (mixing across columns within row). Mitra [Zhang et al., 2025] resembles TabPFNv2 in its per-cell layout but differs in two important ways: labels live in a separate per-row slot rather than being mixed into feature tokens, and there is no positional encoding on either axis. TabICLv2 [Qu et al., 2025] takes a different route: a column-embedding network first compresses each row’s features into a single vector, producing one token per row. A 12-block ICL transformer then mixes these row tokens, with context labels injected before the first ICL block. Full architectural details are in §A.1.

We denote the  $k$ th layer of any model with  $L_k$  and inspect the row representations at that layer by taking activations for both the context and query rows. This allows us to train a simple classifier on context rows using the known context labels, and evaluate the fit using query rows. This linear probe tells us at which depth the model has organized its representations to be linearly separable. We complement this probe with three other measurements: a silhouette score on frozen activations, dimensionality summaries of the activation matrix, and per-block knockout experiments. The probe protocols and dataset lists are in §A. A compact summary of all findings appears in Table 90.

### 2.1 Layerwise probes

The three models reach linearly readable class structure at very different depths. TabPFNv2 keeps mean probe accuracy near chance through most of the layers, then jumps sharply between L8 and L9, from 0.47 to 0.78 on the 49-dataset benchmark, closing most of the gap to its original accuracy (§B.1.1; Figure 2). The regression version of the model behaves identically, with the peak shifted one layer earlier (§E). Mitra follows a similar late-jump profile, peaking at L9 (§D.2).

TabICLv2 inverts this picture entirely. Its column-embedding network plus the first ICL block already produce per-row vectors that a  $k$ NN classifier reads at 0.824 accuracy (within 4 pp of end-to-end: 0.864) so most class structure is laid down before the deep ICL trunk runs (§C.1.3). This means the  $\sim 26$ M-parameter ICL transformer, roughly 95% of TabICLv2’s parameters, adds only marginal accuracy on top of what the column embedder provides, suggesting that a lighter cross-row architecture could recover most of the performance at a fraction of the cost.

TabPFNv2 and Mitra build class-readable representations late and at a single layer; TabICLv2 is readable throughout and has an inefficient design. This contrast motivates the readout analysis of §3.

### 2.2 How the geometry evolves through the stack

The models reshape their internal geometry in opposite directions, as measured by effective rank, participation ratio, and the twoNN intrinsic dim. [Facco et al., 2017] on per-layer activations (§B.1.4).

TabPFNv2 compresses early: effective rank drops from  $\sim 40$  at blocks 0–1 to  $\sim 10$  at block 2. At the final layer, rank correlates with the number of classes ( $r=0.64$  at L11,  $r=0.46$  at the readout layer L9; §I.17), meaning the model uses more representational directions when more classes must be distinguished. Because TabPFNv2’s readout operates on attention patterns rather than feature-space geometry (§3), low rank need not be a bottleneck for the native prediction.

TabICLv2 runs the other way: effective rank expands monotonically through two thirds of the stack. This is consistent with our proposed readout rule (§3.3); it benefits from well-separated class means, though geometry alone does not determine when class structure becomes readable (§C.1.3).

### 2.3 One dominant early block per model

Knocking out individual blocks reveals that in each model, one early block matters far more than any other: the first transformer block in TabPFNv2 and Mitra (block 0), and the final block of the column-embedding network in TabICLv2 (ColEmb-2) (§B.1.2). Each plays the same role: it sets up a coordinate frame that the downstream layers rely on.

**TabPFNv2.** Skipping block 0’s MLP in the residual stream cuts the frozen-probe accuracy at L9 by 37.6 pp, yet a probe retrained from scratch on the post-knockout activations still recovers labels above chance: class information survives but in a frame the rest of the network cannot read. Removing block 9 instead costs little with a retrained probe but cuts the frozen probe by 32.9 pp (§B.1.3). Block 0 sets up the coordinate system; block 9 organizes it into the form the readout expects.

**Mitra.** Replacing the first interleaved row/feature block with the identity costs 15.8 pp on v1 and 41.1 pp on v1.1, the largest single-block drop in both versions of the model. The next-worst block costs  $\leq 2$  pp on v1 and 19.6 pp on v1.1 (§D.3). The gap between versions suggests that different training procedures make one lean more heavily on its first block.

**TabICLv2.** ColEmb-2 is a SetTransformer that compresses per-feature into per-row vectors. Zeroing it cuts final accuracy by 28 pp, yet a probe retrained on the post-knockout ICL-input representations still recovers labels at 0.752 (vs. 0.812 baseline). The same probe frozen from the intact model collapses to 0.555 (§C.1.1). ColEmb-2 plays the same coordinate-setting role as block 0 does for TabPFNv2. There is no analogous late organizing block: knocking out any ICL block costs  $< 3$  pp.

Across all three measurements, the same two-way split emerges. TabPFNv2 and Mitra concentrate their critical computation in one early and one late block, compressing geometry in between; TabICLv2 spreads the work across a large, mostly interchangeable stack whose individual blocks contribute little. This split sets up the readout analysis of §3.

### 3 Readout mechanisms

In §2 we located *where* class-readable representations form in each stack; this section establishes *how* each model turns those representations into predictions. Pinning down the readout tells us what each model actually computes, and predicts where it will break. For all models we state a simple, falsifiable surrogate rule, test it causally with interventions, and transplant it onto the other backbones. The classification numbers below aggregate the full 49-dataset benchmark; details are in §B, §C, and §D.4.

**Faithful surrogate.** A candidate rule is *faithful* when (i) its predicted probabilities track the model’s predicted probabilities at Pearson  $r \geq 0.85$  on the 49-dataset mean, (ii) its accuracy lies within  $\leq 3$  pp, (iii) argmax-agreement reaches Cohen’s  $\kappa \geq 0.8$  on a held-out test split, and (iv) it survives an intervention that preserves only the components named by the rule. Per model, the joint criterion is met on 40/49 datasets for TabPFNv2 and on 43/49 for TabICLv2. These cut-offs are conventional thresholds, but to demonstrate the robustness of our claims, we jointly vary  $r$  and  $\Delta_{\text{acc}}$  within  $\pm 0.05$ , which shifts dataset counts by a few datasets, preserving the original conclusions (§I.18). We find the following rules: an attention-weighted vote at L9 for TabPFNv2 and Mitra, and a class-mean prototype on the final representation for TabICLv2. The linear-prototype rule fails on the TabICLv2 regression model.

#### 3.1 TabPFN: an attention-weighted vote at a late layer

At layer 9 of TabPFNv2, row-attention sharpens abruptly: L9 is the sharpest layer on all 49 datasets, and the attention distribution at that layer concentrates on a handful of training rows (mean maximum weight 0.925; entropy roughly half its L0 value; §B.2.1). Figure 2 (middle, §B.1) shows that L9 is the first layer whose attention pattern strongly correlates with TabPFNv2’s predictions.

**The rule.** Read off the attention weights at L9 and take a weighted vote over context labels. The vote tracks the model’s predicted probabilities at mean Pearson  $r = 0.89$  (§B.2.3). The same picture holds on regression at the same late readout layer (§E). The fidelity decreases monotonically with class count ( $\rho = -0.60$ ), from binary mean 0.93 to ten-class mean 0.80; in that regime, the late MLPs at L9-L11 carry the residual signal. The rule is therefore strongest on binary and few-class problems.

**Causal test.** Replacing the L9 attention pattern with a uniform one collapses accuracy from 0.87 to 0.49 (the majority-class baseline; §B.2.5). The vote thus relies on the same block that §2.3 identified as the readout-building block. The vote signal spreads across all six attention heads at L9 rather than concentrating in one (§I.16). A  $k$ NN classifier on TabPFNv2’s final-layer features agrees with its predictions on only about half of test points, well below input-space  $k$ NN (§B.2.6). The L9 attention pattern itself is best predicted by representation distance at L8 ( $R^2 \approx 0.48$ , §I.9). The rule therefore acts as a *learned similarity* over the context set, not a metric  $k$ NN on the final features. Uniform attention intervention establishes necessity: MLPs at L9-L11 may still contribute on multi-class problems.

### 3.2 Mitra: an attention-weighted vote at a late layer

Mitra’s probe peaks at the same late layer as TabPFNv2’s vote (we report L9 for v1 here, L12 for v1.1 in §D.4). We find the attention-weighted vote is the closest similarity-based surrogate to native, though it does not fully meet the faithful-surrogate bar.

**The rule.** At L9, read off the row-attention weights from each query to context rows, and take a weighted vote over context labels. Mean Pearson  $r$  between vote and native probabilities is 0.89; and the accuracy gap is 4.5 pp (§D.4). This gap exceeds the  $\leq 3$  pp faithful-surrogate threshold. The residual error likely reflects Mitra’s column-attention pathway, which mixes  $y$ -slot and feature-slot information across observations before the row-attention vote and is not captured by the vote rule alone (§D.4). Cosine  $k$ NN at the same layer lies 7.0 pp behind the original and within  $\sim 1.5$  pp of the L9 linear probe. The prototype rule trails by a further 9.0 pp. Despite the gap, the vote dominates all other surrogates and the causal ablation in §D.6 confirms that row attention is the load-bearing path, placing Mitra in the same “retrieval over context rows” family as TabPFNv2.

### 3.3 TabICL: a nearest-prototype readout in the final representation

TabICLv2’s final-block representation is class-clustered enough that a parameter-free class mean readout reproduces its predictions, while the attention vote from TabPFNv2 fails on TabICLv2.

**The rule.** Form one *prototype* per class by averaging the final-block representations of context examples sharing that label, then assign each query to the nearest prototype (Euclidean or cosine). This rule recovers nearly all of TabICLv2’s accuracy (§C.3.1); a small- $k$   $k$ NN on the same representation matches predictions on most queries (§C.3.5). The ordering replicates across all three released versions (Table 31). A linear head also reaches 0.859, but the prototype is parameter-free and reveals the geometric structure the model builds, not merely that the representation is linearly separable.

**Built early, refined distributedly.** The class-clustered geometry is laid down before the ICL stack: within-class proximity sits significantly above chance already at the column-embedding output, and a linear probe here reaches 0.812 versus 0.864 native (§C.1.1). No *individual* ICL block is necessary (§C.2.2), but forcing uniform attention across all twelve drops accuracy by 29 pp (§C.2.3), worse than the probe. For regression, the readout is non-linear: no simple surrogate reproduces the model’s predictions, though the final representation retains useful local structure (§I.1, §F.3).

Where TabPFNv2 retrieves specific rows through sharp attention, TabICLv2 uses no sharp attention at any layer and instead pools entire classes into prototypes: same accuracy with a different algorithm.

### 3.4 Mechanism transplantation: each readout needs its own backbone

If the three models implement distinct readouts, then a readout fit to one backbone should fail on the others. We pass the final-block representation of one backbone through each candidate readout and score on the full benchmark (§I.3).

Swapping readouts across backbones is catastrophic (Table 1). The prototype rule on TabPFNv2 drops by 33 pp; the vote on TabICLv2 drops by 40 pp. On Mitra, which shares TabPFNv2’s vote family, every alternative readout (prototype,  $k$ NN, linear head) falls 7 to 9 pp behind native. A freshly fit logistic head on frozen representations closes the gap on TabICLv2 (0.859 vs. 0.864) but not on TabPFNv2 (0.582 on the shared 42-dataset subset, well below the 0.78 probe at L9; §B.3.8); a nonlinear MLP head gains only  $\sim 1.6$  pp more. TabICLv2 admits a class-clustered linear readout family; TabPFNv2 does not.

**Why surrogate rules matter.** The readout rules are not claims about internal computation; they are simple, falsifiable descriptions that reproduce each model’s input-output behavior. Their value is threefold. First, they predict failure modes: because TabPFNv2 acts as if it performs a weighted vote over neighbors, hub poisoning (flipping labels of the most-attended points) directly corrupts the vote; because TabICLv2 classifies by nearest prototype, rank warp destroys the absolute distances its prototypes are calibrated to (§6). Second, the transplant confirms that readout and backbone are jointly designed: each model builds geometry matched to its own rule, and swapping rules across backbones costs 33 to 40 pp. Third, the rules localize the critical computation: TabPFNv2’s prediction hinges on L9 attention, TabICLv2’s on the column embedder, giving concrete targets for pruning, debugging, and future architecture design.

Table 1: Readout-rule transplantation on the full 49-dataset classification grid (over 5 seeds). Each readout column is applied to the row backbone’s frozen representations at the readout’s preferred layer. Column headers list the model each rule is reported as the surrogate for. Brackets contain the percentage-point drop vs. the row’s native accuracy. Bold marks each backbone’s reported surrogate. Per-dataset numbers, bootstrap CIs, preferred layers, and the MLP variant are in §I.3, I.14, B.3.8, D.4.

Backbone	Native	Vote (TabPFNV2/Mitra)	$k$ NN5	Prototype (TabICLV2)	Linear head
TabPFNV2	0.854	<b>0.804</b> (−5.0)	0.547 (−30.7)	0.523 (−33.1)	0.617 (−23.7)
TabICLV2	0.864	0.470 (−39.5)	0.856 (−0.8)	<b>0.854</b> (−1.1)	0.859 (−0.5)
Mitra	0.860	<b>0.815</b> (−4.5)	0.789 (−7.0)	0.769 (−9.0)	0.776 (−8.3)

## 4 Models want to be permutation invariant

A model is *permutation-invariant* along an axis if its predictions do not depend on the order in which inputs are presented along that axis: shuffling rows of the context set, reordering the columns of every row consistently, or relabelling classes each leave predictions unchanged. Invariance is the dual of the collapse question of §5: collapse asks when distinct inputs become identically encoded; invariance asks when permutation-related inputs receive identical predictions. We ask whether each model acquires invariance natively and, where it does not, whether the missing symmetry can be installed without retraining and without sacrificing accuracy. We find that most models can achieve all forms of invariance, leaving the benchmark accuracy intact. These edits are free because the positional devices are barely used on real data, but they exist for a reason: §5 stress-tests what happens when the defenses they provide are truly needed.

**Architectural starting point.** The three architectures begin from different positions on the column-permutation axis. TabPFNV2 applies feature grouping and a learned positional embedding to every group. TabICLV1 and TabICLV2 apply RoPE along the feature dimension; v2 additionally enforces circular feature grouping. Mitra, in contrast, has *no* positional encoding on either axis and uses a single shared cell embedding applied identically to every column, making it exactly column-invariant (§D.1). All models are row-invariant, though TabPFNV2 has a row signature that can be disabled at no cost to performance. No classification model in the three families is class-invariant by construction.

### 4.1 Making pretrained models invariant

**TabPFNV2: zeroing the per-feature positional weight matrix.** Setting the per-feature positional weight matrix  $W$  to zero while keeping the bias grants *exact* invariance to within-pair swaps and pair permutations and leaves benchmark accuracy unchanged on the benchmark suite. Interestingly, replacing the bias with only its sign also suffices (§G.3).

**TabICLV2: removing RoPE.** Removing RoPE in v2 grants *exact* invariance to circular column shifts and leaves benchmark accuracy essentially unchanged on every dataset (§G.4). The same ablation in v1 is catastrophic (~15 pp drop), because v1 lacks v2’s circular grouping fallback (§5.2). In §4.2 we pretrain an invariant TabICLV1 model from scratch.

**Mitra: column invariance is exact by construction.** With a single shared cell embedding and no positional encoding on either axis, column attention sees feature tokens as a set, so feature reordering is a no-op up to numerics. Across all datasets, both released checkpoints produce mean  $|\Delta p| \leq 0.3\%$  on row and column permutations and predicted-label agreement  $\geq 99.5\%$  (§D.1). The same protocol on TabPFNV2 and TabICLV2 v1/v2 *before* the edits above produces order-of-magnitude larger column drift; our edits then close that gap.

In summary, we verify that: TabPFNV2 with  $W=0$  is group-permutation invariant, TabICLV2 without RoPE is circular-shift invariant, and TabICLV1 without RoPE is arbitrary-column invariant (§G.2).

**Class invariance via One-vs-All.** All classifiers depend on class order through in-context target embeddings and a fixed output head. Wrapping any of them in a One-vs-All classifier grants *full* class-order agreement on every dataset and leaves benchmark accuracy unchanged (§G.6). This works because the models were trained to solve many different tasks, including binary classification. Our solution does not change models’ weights but introduces a simple data processing step. It requires calling the model  $C$  times for  $C$  distinct classes, which can be trivially parallelized.

**The cost of not being invariant.** Our edits eliminate any variability in model predictions at zero accuracy and runtime cost; One-vs-All adds linear-in- $C$  inference (§A.3). Without these edits, permuting columns in a dataset causes up to 8 pp accuracy difference (Figure 5; §G.7). This is one of the reasons why released models rely on ensembling. While it is a valid strategy to obtain approximate invariance, we argue that it is better to include invariance from the start, as Mitra does. The ensembling is then done over different model checkpoints instead of different column orderings.

## 4.2 Pretraining an invariant TabICLv1 from scratch

Can an invariant model be *trained* from scratch at no cost? We conduct a large pretraining experiment of the TabICLv1 model under the stage-1 protocol of Qu et al. [2025] (100k iterations, batch size 512) using four combinations of two switches: (i) RoPE on or off along the feature axis; (ii) the class-conditional output head replaced by a class-invariant head (one-hot label columns, shared per-class decoder, see §G.9).

Each lever alone is essentially free (RoPE removal  $-0.8$  pp, class-invariant head  $-0.3$  pp); combined they cost  $-2.6$  pp. The fully invariant model trains stably and stays close to the non-invariant baseline, confirming that invariance is compatible with ICL pretraining. In §5, we identify which architectural components are missing in TabICLv1’s design, which prevent it from achieving better performance when invariant. Mitra demonstrates that the remaining gap can be closed entirely: column invariance is a property of its architecture, and the trained model is competitive on benchmark accuracy and exhibits no representation collapse (§5). Together, the two results suggest the path forward is architectural invariance rather than positional hacks.

Table 2: TabICLv1 retrained from scratch. Win rate is the per-dataset fraction at which each configuration is best of four.

Class-inv.	RoPE	Acc.	Win
No	Yes	0.829	0.327
No	No	0.821	0.249
Yes	Yes	0.826	0.282
Yes	No	0.803	0.141

## 5 On representation collapse

*Representation collapse* [Qu et al., 2025] is a per-sample within-row identifiability failure: when several columns share the same marginal and the row aggregator is fully column-permutation invariant, two rows that are permutations of each other along those columns receive identical representations even when their labels differ. The canonical illustration is balance-scale (4 features, 5 equally frequent values; Fig. 4 in Qu et al., 2025). In §4, we showed that removing one positional device is free; this section asks what these devices actually defend against and identifies which architectural component shields each model from collapse. As we have seen in §4, TabICLv1 adds RoPE along columns, TabICLv2 additionally enforces repeated circular feature grouping with a target-aware embedding; TabPFV2 uses random per-feature embedding together with feature grouping; and Mitra does not use either positional encoding or feature grouping.

### 5.1 Hand-crafted models pin down what each device does

To explain *why* different approaches succeed, we strip the architectures down to single attention layers we analyze by hand. All results are computed in closed form and reproduced numerically.

**Setup.** A row  $x \in \{0, 1\}^m$  is presented as  $m$  cell tokens, one per column. We study three label rules with shared Bernoulli column marginals (so column-marginal information alone is useless): (A)  $y = x_1$  (one column is the label); (B)  $y = x_1 \oplus x_2$  (label depends jointly on two columns); (C)  $y = \text{majority}(x)$  (a multiset-decidable control). Each model is one attention layer plus a hard-argmax readout, and we report accuracy on the full  $2^m$ -row enumeration with  $m=3$ . Any model whose row representation is invariant to all column permutations is constant on the orbits of  $S_m$  and so cannot exceed the orbit-counting bound: for the binary targets of Tasks A and B at  $m=3$  this bound equals 0.75 (Lemma 1 for Task A in its general orbit-majority form; Proposition 2 for Task B for orbit-wise majority of  $x_1 \oplus x_2$ ; §B.3.4). The bound applies to the toy models M0-M3 below under their assumed query-side invariance; the mapping to the released backbones is by analogy.

**The models.** **M0** is a naive shared-cell-embedding mean-pool: every cell gets the same embedding, the row token averages them, and the readout sees a column-permutation-invariant statistic. M0 hits the 0.75 multiset bound on Task A (§B.3.3). The other three models break the symmetry differently.

**M1 (content route, TabPFNv2-style)** attaches an explicit column identifier to each cell embedding, so cell-level cross-attention conditions on *which column* as well as *which value*. **M2 (structural route, TabICLv2-style)** uses no positional encoding but masks attention so each head sees only one column; on this task family M1 and M2 produce identical predictions. **M3 (pair-grouped)** uses tokens that are super-cells over unordered feature pairs  $(j, k)$  carrying a 4-way value and a pair identifier: the construction we exhibit that also solves Task B (XOR). The released models implement variants of these routes. Accuracies for all four models on Tasks A-C appear in Figure 4 (§B.3.3).

**Mapping to the released models.** TabPFNv2’s feature-grouping (groups of two) is the M3 analogue and its positional embeddings are the M1 analogue. TabICLv1 pairs the M2 analogue (column-stream attention) with RoPE as a within-row symmetry-breaker. TabICLv2 pairs the M2 analogue with the M3 analogue (circular grouping) and adds target-aware embeddings. Each v2 architecture therefore carries two within-row routes, while TabICLv1 carries only one. This matches the benchmark pattern of §4.1: removing any single v2 mitigation is free, while removing RoPE in v1 is catastrophic.

## 5.2 Direct stress test on collapse-prone data

The released v2 checkpoints carry redundant within-row defenses; collapse only appears when we strip them. We probe *which* mitigations are load-bearing on the balance-scale dataset ( $n=625, d=4$ ) and a  $d=12$  balance-like synthetic stress dataset with identical marginals (§I.7).

**One vs. two within-row devices removed (v2 backbones).** Removing any *single* within-row defense on a v2 backbone is approximately free for  $W=0$  on TabPFNv2 and no-RoPE on TabICLv2 (both within  $|\Delta| \leq 0.001$ ); the M3 pair-channel ablation (2nd-slot=0) costs up to  $\sim 14$  pp on the most stressed slice (Tables 78 and 79). Removing *both* exposes the latent collapse: TabICLv2 with RoPE and circular grouping removed drops to the majority baseline on the  $d=12$  stress ( $-50$  pp), and TabPFNv2 with both within-row routes off ( $W=0$  and pair second-slot= 0) drops by 7–12 pp (Table 79). Each v2 architecture therefore carries a *redundant* within-row stack, not a single defense.

**TabICLv1 versus stripped v2.** TabICLv1 no-RoPE drops 44 pp on balance-scale, larger than stripped v2. Under the harder  $d=12$  stress, stripped TabICLv2 also collapses by 50 pp. The buffer that delays v2’s collapse is the target-aware embedding, which v1 lacks and which survives both v2 ablations. Both ICL backbones collapse to the majority baseline once their within-row defenses are gone.

**What makes Mitra special.** Mitra has no within-row symmetry-breaker by design and still matches TabPFNv2 with all its defenses in place (0.96/0.97 vs. 0.96/0.97 on balance-scale and balance-like  $d=12$ ). The relevant counterfactual is v2 *stripped* of its within-row defenses: TabPFNv2 with both routes off only drops to 0.89/0.86, well above majority and in the same regime as Mitra. Compared to TabICLv2, Mitra and TabPFNv2 are more robust to combined within-row stripping. We posit that introducing the context label earlier in the stack and the lack of row compression are the main drivers of this phenomenon. The attacks of §6 follow from the resulting structural difference.

**A recipe for the next generation of models.** When designing the next tabular foundation model, we suggest adopting all three of the following: (i) make the model jointly column-invariant by construction; (ii) inject the label early, as a slot visible to column attention from the first layer; (iii) read out from the in-context labels rather than from a fixed class-conditional head, for example via one-hot labels. Built-in invariance is the more principled design: it makes the predictor a deterministic function of the context, removes the need for permutation ensembling (§4), and closes the symmetry-attack surface that the released models exhibit (§6). The three are complementary, not interchangeable. Mitra adopts all three and reaches benchmark accuracy without any within-row positional device. Adopting only (i) and (iii) leaves an unrecovered gap: TabICLv1 retrained from scratch in this configuration loses 2.6 pp relative to its non-invariant baseline because it lacks (ii) (§4.2).

## 6 Mechanism-grounded adversarial tests

If the readouts of §3 describe what each model computes, they predict which context-set perturbations should hurt which model. We design eight perturbations (§H.1) grouped by what they target; the readouts’ geometry: *hub poison* flips the labels of context points that sit closest on average to all others, and *rank warp* replaces values by their per-column rank, preserving order but destroying absolute scale; context corruptions that affect any flexible classifier: *noise padding*, *centroid* and *boundary* label injection, and *SVD burial* (joint reweighting of high and low-variance directions);

Table 3: Mechanism-grounded attacks on a common 24-classification grid ( $\times 5$  seeds): within-model  $\Delta$  pp with bootstrap CIs. Clean accuracies are 0.882 (TabPFNV2), 0.888 (TabICLV2), and 0.881 (Mitra v1.1; v1 within 1 pp). \* marks Holm-corrected signif. ( $\alpha=0.05$ ). See §H, D.5 for more results.

Attack	TabPFNV2 $\Delta$ pp [95% CI]	TabICLV2 $\Delta$ pp [95% CI]	Mitra $\Delta$ pp [95% CI]
Noise pad	-1.5* [-2.4, -0.7]	-0.6 [-1.5, +0.5]	-0.5 [-1.3, +0.2]
Hub poison	-3.7* [-5.5, -2.1]	-3.3* [-4.8, -1.9]	-2.8* [-4.0, -1.6]
Centroid inj.	-0.2 [-0.9, +0.6]	-0.3 [-1.2, +0.5]	-0.3 [-0.9, +0.4]
Boundary poison	-1.7* [-2.5, -1.0]	-1.2 [-2.2, -0.1]	-1.5 [-3.3, +0.4]
Cube warp	-1.1 [-2.5, +0.1]	-0.3 [-1.4, +1.2]	-0.3 [-0.8, +0.0]
Soft-exp warp	-2.2* [-3.7, -0.8]	-2.3* [-3.9, -0.8]	-2.5* [-3.8, -1.2]
Rank warp	-8.0* [-15.1, -2.4]	-10.1* [-18.7, -3.4]	-0.4 [-1.0, +0.1]
SVD burial	-8.3* [-13.7, -3.6]	-5.0* [-8.7, -2.0]	-8.9* [-14.7, -4.0]

smooth monotone warps: *cube* and *soft-exp*, a Bayesian average over context-conditional predictors should largely absorb them; and a null-space PGD diagnostic (§H.9). All three foundation models are run on the same grid; Ridge, XGBoost, MLP baselines fit fresh on the same poisoned context (§H).

The drops in Table 3, set against the refit baselines of §H, follow this split. The two geometry attacks hurt TabPFNV2/TabICLV2 substantially more than a tuned MLP refit on the same poisoned context, isolating the readouts as the source; Mitra matches the MLP on hub poisoning and is immune to rank warp by virtue of its quantile front-end. The four context corruptions hurt the MLP at least as much as the foundation models, so the drops there—including the large SVD burial drops on TabPFNV2 and Mitra—reflect sensitivity any flexible classifier inherits from a corrupted context. The two monotone warps hurt the MLP roughly twice as much as the foundation models, consistent with their pretraining prior already covering smooth monotone warps that a freshly fit MLP has to learn from a single context. A pre-specified Wilcoxon test on (rank warp, hub poison) vs. (cube warp, centroid injection) rejects at  $p < 10^{-3}$  for TabPFNV2/TabICLV2; the 16-dataset mixed-type slice and the 49-dataset Mitra sweep reproduce the ordering.

## 7 Discussion and limitations

The audit covers 49 classification and 10 regression datasets, multiple permutation and perturbation grids and paired bootstrap intervals throughout: in aggregate, tens of thousands of evaluation points across the three foundation models. TabPFNV2 and Mitra read out through an **attention-weighted vote at a late layer** and TabICLV2 through a **nearest-prototype rule** in its final representation, and swapping these heads across backbones costs 33 to 40 accuracy points: readout and backbone are **jointly designed**. Much of each backbone is **not** load-bearing: the v2 models carry a **redundant within-row stack**, per-block knockouts cost little at almost every layer, the TabPFNV2 readout is nailed at one late block, and on TabICLV2 most of the class signal is already present at the ICL input. Mitra contains *no* within-row symmetry-breakers yet matches the others, proving representation collapse is not fundamental but **architectural**. On the permutation axis, TabPFNV2 and TabICLV2 admit a **one-line edit to exact column invariance** and a One-vs-All wrapper grants **exact class invariance** on any of the three; a from-scratch invariant TabICLV1 trains stably but gains no accuracy, providing further evidence for our prescribed model. The same story predicts the readout-specific breakages: **rank warp** and **hub poisoning** hurt TabPFNV2/TabICLV2 more than a refit MLP does; Mitra is immune to cube and rank warps but shares the  $k$ NN-style hub weakness.

**Limitations.** Two directions are out of scope. We hold the pretraining mixture fixed and do not probe how the synthetic data generator itself shapes the mechanisms we audit, and we do not cover the very large dataset regime, where in-context inference becomes infeasible.

**Future work.** Our findings suggest a hypothesis for a next-generation tabular foundation model: combine Mitra’s backbone (column invariance), an early label-as-column slot, and a One-vs-All output head (class invariance). Each ingredient is accuracy-neutral or better in isolation. Two further follow-ups remain open: (i) the training data itself, where varying the synthetic prior might isolate which behaviors are properties of the architecture versus the data; (ii) mechanism-grounded adversarial defenses, where hub-aware context reweighting and robust quantile transforms can be evaluated under the same paired protocol. Each direction promises foundation models that are simultaneously more accurate, more robust, and more interpretable than the current generation.

## References

- Ekin Akyürek, Dale Schuurmans, Jacob Andreas, Tengyu Ma, and Denny Zhou. What learning algorithm is in-context learning? Investigations with linear models. In *International Conference on Learning Representations*, 2023.
- Qingxiu Dong, Lei Li, Damai Dai, Ce Zheng, Jingyuan Ma, Rui Li, Heming Xia, Jingjing Xu, Zhiyong Wu, Baobao Chang, et al. A survey on in-context learning. In *Proceedings of the 2024 conference on empirical methods in natural language processing*, 2024.
- Elena Facco, Maria d’Errico, Alex Rodriguez, and Alessandro Laio. Estimating the intrinsic dimension of datasets by a minimal neighborhood information. *Scientific Reports*, 7(1):12140, 2017.
- Peiran Gao, Eric Trautmann, Byron Yu, Gopal Santhanam, Stephen Ryu, Krishna Shenoy, and Surya Ganguli. A theory of multineuronal dimensionality, dynamics and measurement. *bioRxiv*, 2017.
- Shivam Garg, Dimitris Tsipras, Percy S Liang, and Gregory Valiant. What can transformers learn in-context? A case study of simple function classes. In *Advances in Neural Information Processing Systems*, 2022.
- Marta Garnelo, Jonathan Schwarz, Dan Rosenbaum, Fabio Viola, Danilo J Rezende, SM Eslami, and Yee Whye Teh. Neural processes. In *ICML Workshop on Theoretical Foundations and Applications of Deep Generative Models*, 2018.
- Aviral Gupta, Armaan Sethi, and Dhruv Kumar. TabPFN through the looking glass: An interpretability study of tabPFN and its internal representations. *arXiv*, 2026.
- Noah Hollmann, Samuel Müller, Lennart Purucker, Arjun Krishnakumar, Max Körfer, Shi Bin Hoo, Robin Tibor Schirrmeyer, and Frank Hutter. Accurate predictions on small data with a tabular foundation model. *Nature*, 2025.
- Jingnan Hu and Sina Ghelichi. Understanding TabPFN: An interpretability analysis of tabular prior-fitted networks. *arXiv*, 2025.
- Jonas Landsgesell and Pascal Knoll. Scoringbench: A benchmark for evaluating tabular foundation models with proper scoring rules. *arXiv*, 2026.
- Junwei Ma, Valentin Thomas, Rasa Hosseinzadeh, Alex Labach, Hamidreza Kamkari, Jesse C Cresswell, Keyvan Golestan, Guangwei Yu, Anthony L Caterini, and Maksims Volkovs. TabDPT: Scaling tabular foundation models on real data. In *Advances in Neural Information Processing Systems*, 2025.
- Duncan McElfresh, Sujay Khandagale, Jonathan Valverde, Vishak Prasad C, Ganesh Ramakrishnan, Micah Goldblum, and Colin White. When do neural nets outperform boosted trees on tabular data? *Advances in Neural Information Processing Systems*, 2023.
- Samuel Müller, Noah Hollmann, Sebastian Pineda Arango, Josif Grabocka, and Frank Hutter. Transformers can do Bayesian inference. In *International Conference on Learning Representations*, 2022.
- Jingang Qu, David Holzmüller, Gaël Varoquaux, and Marine Le Morvan. TabICL: A tabular foundation model for in-context learning on large data. In *International Conference on Machine Learning*, 2025.
- Olivier Roy and Martin Vetterli. The effective rank: A measure of effective dimensionality. *European Signal Processing Conference (EUSIPCO)*, 2007.
- Yuan Sui, Mengyu Zhou, Mingjie Zhou, Shi Han, and Dongmei Zhang. Table meets llm: Can large language models understand structured table data? a benchmark and empirical study. In *Proceedings of the 17th ACM International Conference on Web Search and Data Mining*, pages 645–654, 2024.

- Ashish Vaswani, Noam Shazeer, Niki Parmar, Jakob Uszkoreit, Llion Jones, Aidan N. Gomez, Łukasz Kaiser, and Illia Polosukhin. Attention is all you need. In *Advances in Neural Information Processing Systems*, 2017.
- Johannes Von Oswald, Eyvind Niklasson, Ettore Randazzo, João Sacramento, Alexander Mordvintsev, Andrey Zhmoginov, and Max Vladymyrov. Transformers learn in-context by gradient descent. In *International Conference on Machine Learning*, 2023.
- Manzil Zaheer, Satwik Kottur, Siamak Ravanbakhsh, Barnabas Poczos, Russ R Salakhutdinov, and Alexander J Smola. Deep sets. In *Advances in Neural Information Processing Systems*, 2017.
- Xiyuan Zhang, Danielle C. Maddix, Junming Yin, Nick Erickson, Abdul Fatir Ansari, Boran Han, Shuai Zhang, Leman Akoglu, Christos Faloutsos, Michael W. Mahoney, Cuixiong Hu, Huzefa Rangwala, George Karypis, and Bernie Wang. Mitra: Mixed synthetic priors for enhancing tabular foundation models. In *Advances in Neural Information Processing Systems*, 2025.

## A Experimental protocol

All experiments use 49 classification datasets (4 synthetic, 3 from `sklearn`, and 42 from OpenML) and 10 regression datasets, listed in Tab. 8. We use 5 seeds for invariance experiments, the common 24-dataset attack grid, and the readout-grid calibration table; 10 seeds for the broader TabPFN-vs-XGBoost attack sweep; and 20 seeds for vote-decomposition permutation tests. Exact seed and dataset counts are stated in the relevant captions or subsections.

**Context/query partitions.** For real and OpenML classification datasets, each (dataset, seed) cell starts from an 80/20 stratified context/query split seeded by the seed index. Regression uses the same 80/20 split without stratification. Synthetic controls use their generator-defined train/test sizes. Unless stated otherwise, a given (dataset, seed) context/query partition is reused across the foundation models, surrogate readouts, classical baselines, and attacks.

### A.1 Architectures

This subsection specifies the released classification models audited in the paper, their parameter and shape accounting, the released versions used in each experiment, and the software environment.

**TabPFNV2** [Hollmann et al., 2025]. A per-cell transformer (hidden width  $D = 192$ , 12 blocks) operating on the  $(n_{\text{rows}} + 1) \times n_{\text{cols}}$  table formed by the context set plus the query row. Each block alternates row-wise attention (mixing across context rows for a fixed column) with column-wise attention (mixing across columns for a fixed row), interleaved with MLPs. Inputs are passed through a fixed three-copy preprocessing pipeline (raw, scaled, quantile-rotated). Numerical features are encoded via the per-feature positional matrix  $W$  and bias  $b$ ; class identity is read off the query cell at the output head. For a single query and  $n$  context rows with  $d$  row features, the stack therefore carries  $3(n+1)d$  cell tokens: row attention sees  $n+1$  entries in each of  $3d$  feature streams, and column attention sees  $3d$  entries in each row.

**TabICLv2** [Qu et al., 2025]. A row-then-ICL transformer. In the accounting of Table 4, the model splits into three column-embedding blocks, three pre-label row-interaction blocks (“Row 3”), and then the 12-block row-level ICL transformer (“ICL 12”). The first two stages process the table column by column and emit a single vector per row, i.e. a per-row embedding matrix in  $\mathbb{R}^{(n_{\text{context}}+n_{\text{query}}) \times D_{\text{row}}}$ ; the third column-embedding block is a SetTransformer readout that compresses per-feature into per-sample vectors before the row stage. The 12 ICL blocks then mix the context rows together with the query row after labels are injected. RoPE is applied along the feature dimension and circular feature grouping is applied to inputs. The class prediction is read off the final ICL block’s output for the query row. In shape terms, the ColEmb stack starts from  $d$  feature tokens per row, compresses them to  $(n_{\text{context}} + n_{\text{query}})$  row vectors by ColEmb-2, and from that point onward both the Row 3 and ICL 12 stages operate only on those row tokens.

**Mitra** [Zhang et al., 2025]. A 12-block transformer trained with mixed synthetic priors and released as part of AutoGluon. It differs from TabPFNV2 and TabICLv2 along axes the main analysis identifies as load-bearing: labels live in a *separate* per-row token slot rather than being added to feature tokens; the per-feature embedding is *shared* across columns; and the architecture has *no positional encoding* on either axis. Each block is an interleaved row/feature Layer: a row-attention call lets each query token attend to the context tokens for the same feature, and a column-attention call mixes across features within a row. Both released checkpoints (v1 and v1.1) share this 12-block structure; they differ in their training mixtures. We load Mitra as a single model with AutoGluon’s ensembling/stacking disabled, so the meta-ensemble defaults that would otherwise wrap it are turned off and we measure the model in isolation. Per-experiment Mitra details (invariance, layerwise probes, knockouts, readout fidelity, attacks, collapse) appear in §D.

For TabPFNV2, 7.08M of 7.24M parameters sit in the 12-block transformer stack; “no thinking rows” means this model does not prepend any extra synthetic rows before the context/query table. For TabICLv2, the split is 0.88M / 0.40M / 26.28M across the column, row, and ICL stages. For Mitra, 75.66M of 75.67M parameters sit in the 12-block interleaved row/column stack; the remainder is the per-feature  $1 \rightarrow 512$  embedding, the 10-class label embedding, and the final  $512 \rightarrow 10$  head. The released TabPFNV2 model used here is the 12-block PerFeatureTransformer, not the newer 24-block v2.5/v2.6 architectures, which are released under licenses that are not open-source compatible with this analysis pipeline and are therefore out of scope.

Table 4: Architecture accounting for the three main classification models, derived from the released model files used throughout this paper.

Model	Params	Core stack	Heads	FFN hidden	Normalization
TabPFNv2	7.24M	12 PerFeatureTransformer blocks, $d=192$ , no thinking rows	6 feature + 6 item	768	3 bias-free LN / block
TabICLv2	27.55M	ColEmb 3 + Row 3 + ICL 12, $d_{\text{row}}=128$ , $d_{\text{CL}}=512$	8 / 8 / 8	256 / 256 / 1024	pre-norm LN with bias
Mitra	75.67M	12 interleaved row/column blocks, $d=512$ , separate per-row label slot, no positional encoding	4 row + 4 col	2048	4 LN with bias / block

Table 5: Shape and accounting proxy for the three audited classification models on a single-query context set with  $n$  context rows and  $d$  row features. The ‘‘attention-work proxy’’ counts attention-matrix elements and ignores heads, MLPs, and constant factors; it is a scaling summary, not an exact FLOPs count.

Model	Serialized state	Attention-work proxy	Measured cost
TabPFNv2	$3(n+1)d$ cell tokens throughout the 12-block stack	$3d(n+1)^2$ from row attention + $(n+1)(3d)^2$ from column attention, per block	$\sim 1.0$ s, $\sim 3$ GiB
TabICLv2	$d$ feature tokens / row until ColEmb-2, then $n+1$ row tokens through Row 3 + ICL 12	$3(n+1)d^2$ in the ColEmb stage + $15(n+1)^2$ across Row 3 and ICL 12	$\sim 1.5$ s, $\sim 4$ GiB
Mitra	$(n+1)(d+1)$ tokens per layer ( $d$ feature cells + 1 label slot per row), through the 12-block stack	$d(n+1)^2$ from row attention + $(n+1)(d+1)^2$ from column attention, per block	—

**Software environment.** All experiments run under Python and PyTorch, using the official TabPFNv2 and TabICLv2 Python packages together with sklearn for the classical baselines and probes.

**Categorical features and missingness.** Categorical columns from OpenML datasets (e.g. car, tic-tac-toe, cmc, credit-approval, credit-g, cylinder-bands, eucalyptus) are ordinal-encoded once with a fixed seed and then passed identically to TabPFNv2, TabICLv2, Ridge, and XGBoost, so that any model differential is not driven by encoding choice. This equalises the inputs across baselines; it is not a benchmark of native-categorical CatBoost or native-categorical XGBoost, which use their own typed pathways. Missing values are median-imputed for numerical columns and mode-imputed for categorical columns at fetch time. The post-encoding feature count  $d$  in Tab. 8 reflects this encoding.

## A.2 Probes and separability measurements

This subsection specifies the linear probe, its random-init control, the silhouette score, and the three geometry summaries used to characterize per-layer representations.

**Linear probe.** Given a frozen activation tensor  $h \in \mathbb{R}^{n \times D}$  at some layer, we fit a logistic-regression classifier  $\hat{y} = \arg \max_c W_c h$  on a labeled subset of the context rows and report its accuracy on a held-out subset of the same dataset. Unless stated otherwise, the probe is trained per (dataset, layer, seed) using multiclass logistic regression with  $\ell_2$  regularization  $C=1$  and an L-BFGS solver, on an 80/20 train/eval split of the context rows under a per-seed shuffle. The maximum number of solver iterations is raised to 2000 to ensure convergence on the higher-dimensional probe inputs (semeion  $d=256$  and mfeat-pixel  $d=240$ ). We always report probe accuracy alongside two reference points: (i) the per-dataset chance baseline (the majority-class frequency, mean  $\approx 0.50$  across our 49 classification datasets), and (ii) the model’s own end-to-end accuracy on the same (dataset, seed) pair. A probe accuracy that approaches the second reference indicates that essentially all of the model’s classification-relevant information is already linearly readable at that layer.

**Random-init control.** Wherever a probe accuracy is reported, we also report the same probe trained on the activations of a copy of the model whose transformer weights have been replaced by random initialisations. This control isolates the part of separability that is due to the trained weights as opposed to the architecture or the probe’s own capacity.

**Silhouette score.** For a labeled point cloud  $\{(h_i, y_i)\}$ , the silhouette of  $h_i$  is  $(b_i - a_i) / \max(a_i, b_i)$ , where  $a_i$  is the mean distance from  $h_i$  to other points of the same class and  $b_i$  is the mean distance from  $h_i$  to points of the nearest *other* class. The dataset-level silhouette score is the mean over  $i$  and

lies in  $[-1, +1]$ ; values near  $+1$  indicate clean per-class clusters. We use cosine distance and report silhouette scores at every layer.

**Geometry summaries.** For a frozen activation matrix  $h \in \mathbb{R}^{n \times D}$  with mean-centered singular values  $\sigma_1 \geq \dots \geq \sigma_r > 0$ , define normalized squared spectrum  $p_i = \sigma_i^2 / \sum_j \sigma_j^2$ . We report three standard summaries:

- *Effective rank*  $\exp(-\sum_i p_i \log p_i)$ : the exponential of the spectral entropy [Roy and Vetterli, 2007]. Equals  $r$  for a flat spectrum and 1 when one direction dominates; insensitive to absolute scale.
- *Participation ratio (PR)*  $(\sum_i \sigma_i^2)^2 / \sum_i \sigma_i^4$ : a heavier weighting toward the leading directions [Gao et al., 2017]. PR equals  $r$  for a flat spectrum but drops much faster than effective rank when a few directions concentrate most of the variance.
- *2NN intrinsic dimension (2NN-ID)* [Facco et al., 2017]: estimated from the ratio of distances to the second and first nearest neighbour of each point. Captures the dimensionality of the local data manifold rather than of the global covariance, and is therefore typically smaller than effective rank.

Effective rank and PR are linear-algebraic measures of how the activation *covariance* is spread across directions; 2NN-ID is a geometric measure of how the activation *point cloud* fills its ambient space. They agree qualitatively but probe different things, which is why we report all three.

### A.3 Hardware and example costs

This subsection specifies the compute node, the approximate budget of the headline GPU-bound runs, and the per-prediction inference cost on that node.

All experiments were run on a node with  $4 \times$  NVIDIA H100 NVL GPUs (94 GiB each) and dual Intel Xeon CPUs (128 physical cores); preprocessing and CPU-only experiments use this CPU pool.

Table 6 gives the approximate cost of the headline GPU-bound experiment families measured on this node; many smaller CPU-bound or single-dataset sweeps are omitted because they do not materially affect the total budget.

Table 6: Approximate compute ledger for the headline GPU-bound runs in the paper. Costs are measured on the  $4 \times$  H100 node above and rounded to the nearest half GPU-hour.

Experiment family	Grid	Approx. cost
Full inference-only sweep with probes	49 cls $\times$ 10 seeds, all layers, sharded over 4 GPUs	$\sim 2$ GPU-hours total
Frozen probe after knockout	49 $\times$ 10, 4 KO points $\times$ 8 probe positions	$\sim 6$ GPU-hours
Vote decomposition with 1000 row-permutation null	49 cls $\times$ 20 seeds	$\sim 4$ GPU-hours
Activation patching	clean/corrupted pair enumeration on 49 cls	$\sim 18$ GPU-hours
Headline subtotal	—	$\sim 30$ GPU-hours

**Per-prediction inference cost.** On the same hardware, cold end-to-end inference for a single query is  $\sim 1.0$  s for TabPFNv2,  $\sim 1.5$  s for TabICLv2, and  $\sim 2.0$  s for TabICLv2-reg (numbers include preprocessing). Peak GPU memory for these calls is  $\sim 3$  GiB,  $\sim 4$  GiB, and  $\sim 5$  GiB respectively, well within a single H100. The OvA wrapper of §4.1 multiplies these by the class count  $C$ : no measured accuracy penalty for binary classification,  $\sim 10$  s and  $\sim 30$  GiB for the ten-class mfeat-\* family. Zeroing  $W$  in TabPFNv2 and removing RoPE in TabICLv2 are zero-overhead edits to fixed parameters and do not change wall-clock or memory.

All experiments, except for TabICLv1 are inference-only on released models.

### A.4 Seeds, dataset subsets, and XGBoost tuning

This subsection specifies the seed convention, the enumerated dataset subsets used by individual experiments, the attack-grid accounting, the calibration metric definitions, the XGBoost reference configuration, and the full attack hyperparameter values.

**Random seeds.** Whenever an experiment uses  $N$  seeds we use the integer seeds  $0, 1, \dots, N-1$ ; the 20-seed permutation null uses  $0, \dots, 19$ . Each (dataset, seed) cell is therefore deterministic given the software environment above. We disable TF32 matmul for both backbones and set deterministic cuDNN algorithms; forward passes through the released models match across consecutive runs to within  $10^{-6}$  in logits on H100.

**Explicit subset compositions.** The compute-intensive experiments are run on enumerated subsets of the full 49-classification grid; the exact lists are:

- *The 24-classification attack grid* (§6), defined as the intersection of the TabPFNv2 and TabICLv2 attack runs: LED-display-domain-7digit, MiceProtein, balance-scale, banknote-authentication, blood-transfusion-service-center, breast-w, breast\_cancer, car, climate-model-simulation-crashes, cylinder-bands, dresses-sales, eucalyptus, iris, mfeat-factors, mfeat-fourier, mfeat-karhunen, mfeat-morphological, mfeat-pixel, quadrant\_2d, random\_labels, sign\_1d, steel-plates-fault, wine, xor\_2d.
- *The 16-dataset mixed-type clean slice* (Tab. 67, §H.7): dresses-sales, car, cylinder-bands, eucalyptus, cmc, credit-approval, credit-g, analcatdata\_dmft, anneal, Fitness\_Club, Is-this-a-good-customer, qsar-biodeg, website\_phishing, MIC, tic-tac-toe, ilpd.
- *The mixed16 attack slice* (Tab. 68, §H.8): the same 16 datasets as the mixed-type clean slice above, but only the three highest-signal attacks (hub poison, rank warp, SVD burial) under the shared ordinalised numeric view.
- *The 10-classification head-resolved TabPFNv2 vote subset* (§B.2.4): balance-scale, breast\_cancer, credit-g, diabetes, ilpd, iris, mfeat-zernike, tic-tac-toe, vehicle, wine.
- *The per-block MLP knockout subset* (Tab. 13, §2.3): xor\_2d, quadrant\_2d, sign\_1d, random\_labels, balance-scale, banknote-authentication, breast-w, iris, wine, vehicle, and steel-plates-fault. This fixed subset keeps the four synthetic controls and adds binary, three-class, four-class, and seven-class real tasks so the mean drop table is auditable from the PDF alone.

**Attack accounting.** The attack results use two distinct reporting grids. The matched cross-model comparison in Table 3, Table 64, Table 65, and Table 66 uses the common 24-classification grid with 5 seeds per dataset (per-cell numbers may differ by up to  $\sim 0.2$  pp across the three tables because they were produced in independent runs over the same grid). The broader TabPFN-vs-XGBoost appendix comparison in Table 63 uses 49 classification datasets  $\times$  10 seeds, except MONO\_SOFTEXP where one dataset is dropped for numerical degeneracy and  $n=48$ . The null-space PGD diagnostic in §H.9 uses the 29 datasets with sufficient null-space dimension after the explicit exclusions in §H.9. The readout-grid calibration table (§I.14) uses 49 classification datasets  $\times$  5 seeds.

**Calibration metrics.** Expected calibration error (ECE) in Table 85 is computed per (dataset, seed) with 15 equal-width confidence bins and then averaged over seeds within dataset; negative log-likelihood (NLL) is the multiclass log loss on the same held-out query split. Unless stated otherwise, the readout-grid table reports means over the 49 per-dataset seed means.

**XGBoost reference.** The XGBoost baseline used throughout (Tab. 3, Apps. H.3, H.4, H.2) uses XGBoost 2.1.4 with 5-fold stratified-CV grid search over number of trees  $\in \{200, 500, 1000\}$ , maximum depth  $\in \{3, 6, 9\}$ , learning rate  $\in \{0.03, 0.1\}$ , and row subsample  $\in \{0.7, 1.0\}$ , with early stopping (patience 50) on a held-out 20% validation split. Categorical columns share the same ordinal encoding used for TabPFNv2/TabICLv2; the native-categorical XGBoost pathway is not used here so that the encoding is identical across baselines. The selected configuration is then refit on the full context set and evaluated on the same query partition each foundation model sees. The broader mixed16 clean-only native-categorical XGBoost control in Tab. 67 uses the same package version with the native-categorical pathway enabled; it is validation-tuned on the same 20% held-out split over depths  $\in \{4, 6\}$ , learning rates  $\in \{0.03, 0.10\}$ , and number of trees  $\in \{300, 600\}$ .

**Attack hyperparameters.**

Table 7: Complete hyperparameters for the eight attacks in Table 3, fixed before any model evaluation.

Attack	Parameter(s)	Value
Noise pad	$\sigma$ multiplier of feature std; pad fraction	$4\times$ ; 20% of $ S $
Hub poison	hub fraction; centrality metric	top 15%; rep-cosine kNN degree at L9
Centroid inj	injected counter-class examples per class	$\max(3,  S /100)$
Boundary poison	boundary margin (fraction of inter-centroid dist.)	0.20
Mono cube	exponent of signed cube root warp	1/3
Mono softexp	soft-exponential temperature $\tau$	1.0
Mono rank	per-column rank transform	deterministic, ties broken by index
SVD hide	null-space cutoff $\gamma$	$10^{-6} \cdot \sigma_{\max}$
Nullspace PGD	step $\eta$ , iters $T$ , budget $\varepsilon$	0.01, 200, 1.0 (in feature std units)

## A.5 Statistical reporting protocol

This subsection specifies the reporting unit, the bootstrap procedure, the permutation null, and the multiple-comparison correction used throughout the paper.

- *Primary reporting unit = dataset* for real-data benchmark tables. Whenever a metric is computed at the (dataset, seed) level, we first average across seeds within each dataset and then average across datasets. Because every dataset uses the same number of seeds, these values equal the corresponding dataset  $\times$  seed grand means printed in some appendix tables.
- *Bootstrap CIs on benchmark deltas* resample the vector of per-dataset paired differences after averaging seeds within dataset. This convention is used for vote decomposition, frozen probes, attacks, and transplantation (§3.4; §I.3).
- *Single-dataset synthetic sweeps* (e.g. the K8 collapse  $f$ -sweep) use seed as the reporting unit and state this explicitly; their CIs are paired bootstraps over the seedwise difference vector.
- *Permutation  $z$*  for vote decomposition: 1 000 row-permutation nulls per dataset  $\times$  20 seeds.
- *Multiple comparisons*: Bonferroni applied to the 10 regression tests; classification leaderboards report raw per-dataset numbers without family-wise correction (we report  $n$  explicitly).

## A.6 Dataset inventory

This subsection lists every classification and regression dataset used in the paper, together with the exact OpenML task and dataset identifiers and the asset-provenance record.

Table 8: All 49 classification (top) and 10 regression (bottom) datasets.  $n$  is the raw row count;  $d$  is the post-encoding feature count;  $K$  is the number of classes. Source codes: S = synthetic, K = sklearn, O = OpenML.

src name	$n$	$d$	$K$	src name	$n$	$d$	$K$	src name	$n$	$d$	$K$
O Fitness_Club	1500	6	2	O credit-g	1000	20	2	O pc3	1563	37	2
O Is-this-a-good-customer	1723	13	2	O cylinder-bands	540	37	2	O pc4	1458	37	2
O LED-display-domain-7digit	500	7	10	O diabetes	768	8	2	O qsar-biodeg	1054	41	2
O MIC	1699	111	8	O dresses-sales	500	12	2	S quadrant_2d	250	5	4
O MiceProtein	1080	77	8	O eucalyptus	736	19	5	S random_labels	150	5	2
O analcatdata_authorship	841	70	4	O hill-valley	1212	100	2	O red_wine	1599	11	6
O analcatdata_dmft	797	4	6	O ilpd	583	10	2	O semeion	1593	256	10
O anneal	898	38	5	K iris	150	4	3	S sign_id	150	5	2
O balance-scale	625	4	3	O kc2	522	21	2	O steel-plates-fault	1941	33	2
O banknote-authentication	1372	4	2	O maternal_health_risk	1014	6	3	O tic-tac-toe	958	9	2
O blood-transfusion-service-center	748	4	2	O mfeat-factors	2000	216	10	O vehicle	846	18	4
O breast-w	699	9	2	O mfeat-fourier	2000	76	10	O wdbc	569	30	2
K breast_cancer	569	30	2	O mfeat-karhunen	2000	64	10	O website_phishing	1353	9	3
O car	1728	6	4	O mfeat-morphological	2000	6	10	K wine	178	13	3
O climate-model-simulation-crashes	540	20	2	O mfeat-pixel	2000	240	10	S xor_2d	250	5	2
O cmc	1473	9	3	O mfeat-zernike	2000	47	10				
O credit-approval	690	15	2	O pci	1109	21	2				

10 regression datasets (all OpenML; K omitted):

src name	$n$	$d$	src name	$n$	$d$	src name	$n$	$d$
O Another-Dataset-on-used-Fiat-500	1538	7	O cars	804	17	O forest_fires	517	12
O Moneyball	1232	14	O concrete_compressive_strength	1030	8	O healthcare_insurance_expenses	1338	6
O QSAR_fish_toxicity	907	6	O energy_efficiency	768	8	O socmob	1156	5
O airfoil_self_noise	1503	5						

**Exact OpenML identifiers.** For the OpenML assets in Table 8, `task_id` fixes the supervised task and `dataset_id` fixes the local dataset version used in our cache.

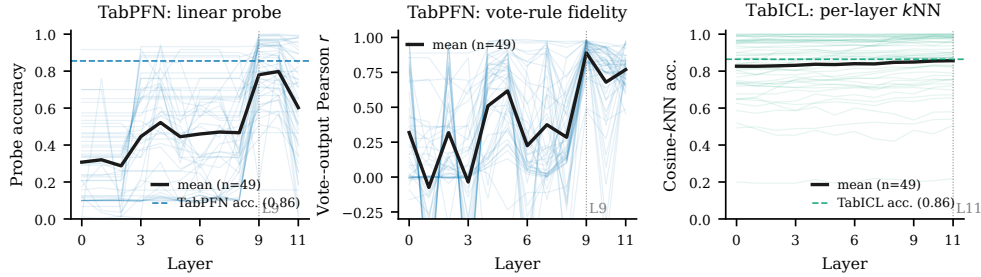


Figure 2: Per-layer profiles on the 49-dataset classification suite. Thin lines: seed-averaged per-dataset curves; thick black lines: means. **Left:** TabPFNv2 linear-probe accuracy converges late with a sharp jump at L8  $\rightarrow$  L9. **Middle:** Pearson correlation between an attention-weighted vote read off layer  $L$  and TabPFNv2’s predicted probabilities; the vote rule (§3.1) becomes faithful only at L9. **Right:** TabICLv2 cosine- $k$ NN accuracy on per-block representations runs high almost from the input.

Table 9: Exact OpenML identifiers for the 42 classification datasets in Table 8.

Name	task_id	dataset_id	Name	task_id	dataset_id	Name	task_id	dataset_id
Fitness_Club	363671	46927	cmc	23	23	mfeat-morphological	18	18
Is-this-a-good-customer	363682	46938	credit-approval	29	29	mfeat-pixel	146824	40979
LED-display-domain-7digit	125921	40496	credit-g	31	31	mfeat-zernike	22	22
MIC	363711	46980	cylinder-bands	14954	6332	pc1	3918	1068
MiceProtein	146800	40966	diabetes	363629	46921	pc3	3903	1050
analcadata_ownership	3549	458	dresses-sales	125920	23381	pc4	3902	1049
analcadata_dmft	3560	469	eucalyptus	2079	188	qsar-biodeg	363696	46952
anneal	363614	46906	hill-valley	9970	1479	red_wine	361250	44972
balance-scale	11	11	ilpd	9971	1480	semeion	9964	1501
banknote-authentication	10093	1462	kc2	3913	1063	steel-plates-fault	146817	40982
blood-transfusion-service-center	10101	1464	maternal_health_risk	363685	46941	tic-tac-toe	49	50
breast-w	15	15	mfeat-factors	12	12	vehicle	53	54
car	146821	40975	mfeat-fourier	14	14	wdbc	9946	1510
climate-model-simulation-crashes	146819	40994	mfeat-karhunen	16	16	website_phishing	363707	46963

Table 10: Exact OpenML identifiers for the 10 regression datasets in Table 8.

Name	task_id	dataset_id	Name	task_id	dataset_id
Another-Dataset-on-used-Fiat-500	363615	46907	concrete_compressive_strength	361237	44959
Moneyball	361616	41021	energy_efficiency	361617	44960
QSAR_fish_toxicity	361621	44970	forest_fires	361618	44962
airfoil_self_noise	361235	44957	healthcare_insurance_expenses	363675	46931
cars	361622	44994	socmob	361264	44987

**Asset provenance.** Table 11 records the released artifacts used.

Table 11: Asset provenance.

Asset class	Identifier in this PDF	Terms / license status
OpenML datasets	Tables 9 and 10	Upstream terms vary by dataset; we use the OpenML task and dataset IDs as published.
scikit-learn datasets	Table 8	Inherited from the scikit-learn distribution.
Released models	TabPFN v2 (release 7.0) and TabICL (release 2.0.3); see §A.1	Used as published; upstream terms apply.

## B TabPFN classification: full results

The full results for TabPFNv2 classification cover where class-readable structure forms (§B.1), what the readout computes at L9 (§B.2), and the collapse analysis built around the M0–M3 hand-crafted models (§B.3).

## B.1 Where class-readable structure forms

### B.1.1 Probe convergence

A logistic-regression probe trained per (dataset, layer, seed) on context-row activations and then averaged within dataset over 10 seeds gives the left panel of Figure 2. Across all 49 classification datasets, mean accuracy stays near chance through L0–L8 and then jumps from 0.467 to 0.780 between L8 and L9 (Table 12, Figure 2). The smaller L9 → L10 gain is a late refinement, not a second phase transition; the sharp L8 → L9 break is the crystallization point used throughout the main text. Silhouette scores rise in lockstep.

Table 12: Linear-probe accuracy at each TabPFN block, mean and std across the same 49 classification datasets shown in Figure 2, after averaging 10 seeds within dataset. The sharp +0.31 jump from L8 to L9 marks the onset of the late-readout regime used throughout the paper; L10 is a smaller follow-on refinement.

Block	-1	0	1	2	3	4	5	6	7	8	9	10	11
mean acc	0.394	0.307	0.320	0.287	0.446	0.522	0.445	0.460	0.470	0.467	0.780	<b>0.798</b>	0.602
std	0.271	0.209	0.218	0.210	0.271	0.277	0.266	0.264	0.265	0.246	0.198	0.173	0.282

### B.1.2 Block knockouts (retrained probes)

Zeroing each MLP sub-block in turn and retraining the linear probe at L9 isolates which blocks the readable structure depends on.

Table 13: TabPFN per-block MLP knockout: mean accuracy drop (pp) across  $n=11$  fixed classification datasets (the four synthetic controls plus `balance-scale`, `banknote-authentication`, `breast-w`, `iris`, `wine`, `vehicle`, and `steel-plates-fault`), baseline 0.907. Block 0 dominates; blocks 5–6 are a clear secondary cluster; the remaining blocks are individually replaceable.

Block	0	1	2	3	4	5	6	7	8	9	10	11
$\Delta$ acc (pp)	-48.1	-0.3	-0.9	-1.6	-0.9	-20.0	-19.6	-8.9	-2.9	-6.3	-1.5	-2.9
std (pp)	16.8	0.8	1.1	1.6	1.5	15.6	20.1	13.6	3.6	7.2	2.6	4.2

Block 0 is the most damaging on 38 of 49 datasets (probe drop  $\approx 40$  pp). A retrained probe still recovers labels at lower accuracy, so block 0 sets up the coordinate frame that the later blocks expect rather than destroying class information outright.

### B.1.3 Frozen probes after knockout (causality)

Frozen probes isolate the causal contribution of each block. Probes trained at  $\ell \in \{-1, 0, 3, 5, 7, 9, 10, 11\}$  on the intact model are frozen, then evaluated under  $\text{KO}@\{0, 5, 9\}$  on 49 datasets and 10 seeds.

Table 14: Frozen-probe accuracy under block knockout. Probes trained on clean model, evaluated without retraining after zeroing block 0 (KO@0) or block 9 (KO@9). Mean and std across 49 datasets  $\times 10$  seeds.

Layer	Baseline		KO@0		KO@9	
	Mean	Std	Mean	Std	Mean	Std
Input	0.394	0.274	0.394	0.274	0.394	0.274
L0	0.307	0.211	0.292	0.214	0.307	0.211
L3	0.446	0.274	0.415	0.253	0.446	0.274
L5	0.445	0.269	0.418	0.263	0.445	0.269
L7	0.470	0.268	0.313	0.171	0.470	0.268
L9	0.780	0.201	0.404	0.226	0.451	0.279
L10	0.798	0.175	0.499	0.255	0.496	0.241
L11	0.602	0.284	0.321	0.212	0.515	0.275

KO@9 drops L9 frozen-probe accuracy from 0.780 to 0.451 ( $\Delta = -0.329$ ); KO@0 cascades to 0.404 ( $\Delta = -0.376$ ). Two roles: block 0 sets the frame, block 9 writes the readable structure.

### B.1.4 Per-layer rank profile and intrinsic dimension

Effective rank, participation ratio (PR), and the two-NN intrinsic dimension of [Facco et al. \[2017\]](#), averaged over 49 classification datasets and 5 seeds (TabPFNv2-clf). TabPFNv2 bottlenecks early: rank and PR drop sharply at block 2 and recover only partially. The residual rank at the readout scales with the number of classes (mean L11 effective rank 21.6 for  $C \leq 3$  vs. 31.7 for  $C \geq 4$ ; Pearson  $r = +0.64$ ; §I.17). This is structurally different from the identical-representation collapse mode of [Qu et al. \[2025\]](#), tested in §B.3.

Table 15: TabPFN per-block geometry, mean over 49 datasets  $\times$  5 seeds. Block  $-1$  is the input row before any feature mixing.

Block	Effective rank	PR	2NN-ID
-1	0.00	0.00	0.00
0	40.37	2.53	4.62
1	41.97	1.87	8.76
2	10.20	1.47	4.52
3	19.99	2.13	5.76
4	22.51	2.01	5.87
5	21.69	1.88	5.25
6	23.92	1.82	5.60
7	20.56	1.87	5.33
8	16.15	1.99	4.86
9	22.81	2.80	4.41
10	25.28	2.98	4.48
11	25.21	3.25	4.77

## B.2 What the readout computes at L9

### B.2.1 Row-attention sharpness

L9 is the sharpest layer on all 49 datasets: mean max weight 0.925 (std 0.078), mean entropy 1.756 versus 3.126 at L0. IQR of max weights is [0.89, 0.97]; only two datasets fall below 0.80.

### B.2.2 Target-column attention vs. similarity

L9 attention tracks input similarity but is not reducible to it. The Spearman rank correlation between the L9 attention weight on each context row (restricted to the target column) and input-space  $\ell_2$  similarity is positive on 45 of 49 datasets (median  $r = 0.32$ , IQR [0.20, 0.48], tail to  $r > 0.70$ ). The representation-distance regression of §I.9, summarized in Table 16, sharpens this picture: input distance alone explains only a small fraction of the L9 attention pattern, L8 representation distance more than doubles that variance, and the full learned-similarity model nearly triples it.

Table 16:  $R^2$  of three predictors of L9 row-attention, across 49 classification datasets (5 seeds each). Input  $\ell_2$ : linear regression on raw input distance only. Rep  $\ell_2$  (L8): the same with L8 representation distance. Full: learned bilinear similarity from L8. Median, IQR, mean, and number of datasets exceeding  $R^2 = 0.5$ .

Predictor	median	q25	q75	mean	$n(R^2 > 0.5)/49$
Input $\ell_2$	0.168	0.051	0.345	0.218	2
Rep $\ell_2$ (L8)	0.488	0.339	0.627	0.477	21
Full learned sim.	0.606	0.487	0.728	0.600	35

### B.2.3 Vote decomposition (all 49 datasets)

Vote is

$$\hat{p}(c) = \frac{1}{H} \sum_{h=1}^H \sum_{i=1}^{N_{\text{train}}} \alpha_i^{(h)} \mathbf{1}[y_i = c],$$

with  $\alpha_i^{(h)}$  the L9 attention weight from the query to context row  $i$  in head  $h$ . Evaluated on 49 datasets (20 seeds each); the random-labels condition is a negative control.

Table 17: Vote decomposition: attention-weighted label vote at L9 vs. final output. Pearson  $r$ , Spearman  $\rho$ , and null-shuffle  $z$ -score per dataset (20 seeds each). Mean across all 49 datasets: Pearson  $r = 0.890 \pm 0.114$ , Spearman  $\rho = 0.849 \pm 0.138$ ,  $z = 6.79 \pm 3.79$ .

Dataset	Pearson $r$	Spearman $\rho$	$z$ -score
Fitness_Club	0.982	0.989	7.32
Is-this-a-good-customer	0.976	0.992	1.46
LED-display-domain-7digit	0.820	0.839	9.82
MIC	0.974	0.727	8.95
MiceProtein	0.799	0.665	11.58
analcatdata_authorship	0.960	0.737	10.70
analcatdata_dmft	0.495	0.451	1.99
anneal	0.935	0.774	12.90
balance-scale	0.919	0.888	6.52
banknote-authentication	0.971	0.807	2.44
blood-transfusion-service-center	0.963	0.977	5.13
breast-w	0.984	0.955	3.81
breast_cancer	0.978	0.938	3.53
car	0.913	0.900	13.51
climate-model-simulation-crashes	0.976	0.979	6.09
cmc	0.900	0.861	6.74
credit-approval	0.966	0.957	2.60
credit-g	0.971	0.976	6.36
cylinder-bands	0.896	0.918	4.49
diabetes	0.983	0.991	6.95

(First 20 of 49 datasets)

Population means: Pearson  $r = 0.888 \pm 0.114$ , Spearman  $\rho = 0.848 \pm 0.139$ ,  $z = 6.88 \pm 3.77$  (1 000 row-permutation nulls). Worst cases are ten-class digit datasets (mfeat-zernike  $r = 0.71$ , mfeat-factors 0.71, semeion 0.76): vote distributes mass over class indicators while accuracy uses an arg max. The optimal head-reweighting NNLS score gives an upper bound on what a fixed convex recombination of head votes buys.

**Multi-class fidelity scaling.** Per-dataset vote-fidelity  $\bar{r}$  decreases monotonically with class count  $C$  across the 49-dataset population: linear regression of  $\bar{r}$  on  $C$  yields slope  $-0.016$  per class (intercept 0.957, Pearson  $-0.43$ , Spearman  $\rho = -0.60$ ,  $p < 10^{-5}$ ,  $n = 49$ ), with binary-class mean 0.93, mid-class ( $3 \leq C \leq 8$ ) mean 0.88, and ten-class mean 0.80. The ten-class digit cluster ( $r \in [0.71, 0.76]$ ) lies within the residual spread of this trend: the multi-class gap reflects the vote rule’s finite per-class indicator capacity rather than a mechanism switch in TabPFNv2.

### B.2.4 Head- and layer-resolved vote

Table 18: Per-head vote Pearson  $r$  at L9. Each head’s vote is computed independently; mean across heads shown in last column. Results show no single head dominates the vote signal (10 datasets  $\times$  20 seeds).

Dataset	H0	H1	H2	H3	H4	H5	Mean
balance-scale	0.937	0.795	0.872	0.935	0.762	0.883	0.864
breast_cancer	0.988	0.166	0.889	0.968	0.600	0.979	0.765
credit-g	0.951	-0.432	0.615	0.910	0.820	0.938	0.634
diabetes	0.977	0.592	0.735	0.975	-0.400	0.973	0.642
ilpd	0.982	0.754	0.413	0.988	-0.624	0.805	0.553
iris	0.990	0.843	0.968	0.987	-0.085	0.968	0.779
mfeat-zernike	0.818	0.403	0.526	0.750	0.052	0.642	0.532
tic-tac-toe	0.820	-0.113	0.772	0.780	0.307	0.699	0.544
vehicle	0.887	0.149	0.760	0.873	0.109	0.779	0.593
wine	0.973	0.921	0.961	0.974	0.353	0.950	0.855

The six L9 heads span 0.05–0.10 Pearson units around the head-mean. The layer profile is flat through L8, jumps at L9, and is sustained through L11. The largest single-head zeroing drop is 3.9 pp at L9 (§I.16); the L9 peak is real and distributed across heads.

### B.2.5 Causal attention forcing

Replacing L9 softmax weights with  $1/N_{\text{train}}$  collapses accuracy from 0.874 to 0.488 ( $\Delta = -0.386$ ), matching the majority-class baseline (0.498, §I.11). MLP knockout at any block also collapses accuracy to the same vicinity (§E.5): L9 attention is one part of a working circuit, not the unique site of computation.

### B.2.6 $k$ NN agreement vs. TabPFN

Agreement between TabPFNv2’s prediction and  $k$ NN under input  $\ell_2$ , L9 rep  $\ell_2$ , L9 rep cosine, and L9 Mahalanobis,  $k \in \{1, 3, 5\}$ , on 49 datasets and 10 seeds (Table 19, top). Input-space  $k$ NN reaches 0.78–0.81 across  $k$ ; representation-space  $\ell_2$ /cosine  $k$ NN at L9 reaches only 0.54–0.56, and Mahalanobis is worse (0.37–0.41). Strengthening the test by reading from L11 (K1) does not change the picture (Table 19, middle). Even the strongest learned-metric variants (NCA-trained  $\ell_2$ , shrunk Mahalanobis, soft- $k$ NN with a fitted temperature, all at L9) max out around 0.84 (Table 19, bottom). A 1-hidden-layer GELU MLP head fit on the frozen final representation (§B.3.8) also fails to recover native accuracy on TabPFNv2 (−24.9 pp paired, 95% bootstrap CI  $[-32.5, -18.0]$ , worse on 38/42 shared datasets) while almost recovering it on TabICLv2 (−0.8 pp,  $[-1.5, -0.3]$ ): a non-linear head does not close the asymmetry. The model is not a  $k$ NN in its own representation. The accurate framing is the learned similarity of §I.9, where rep- $\ell_2$  at L8 explains  $R^2 \approx 0.48$  of the L9 attention pattern.

Table 19: Agreement between TabPFN’s argmax prediction and a  $k$ NN baseline under several distance metrics, mean across 49 datasets. Top: L9 representations. Middle: L11 representations (§I.4). Bottom: learned-metric variants at L9. Every representation-space variant agrees with TabPFN on a strict minority of test points; only soft- $k$ NN with a fitted temperature crosses 0.8.

Metric	$k = 1$	$k = 3$	$k = 5$
<i>Input space and L9 representations (49 datasets)</i>			
Input $\ell_2$	0.781	0.801	0.813
L9 rep $\ell_2$	0.540	0.556	0.561
L9 rep cosine	0.540	0.556	0.562
L9 Mahalanobis	0.367	0.393	0.414
<i>L11 representations (K1, 49 datasets)</i>			
L11 rep $\ell_2$	0.528	0.554	0.561
L11 rep cosine	0.528	0.554	0.561
L11 Mahalanobis	0.356	0.378	0.395
<i>Learned-metric L9 variants (L1, 49 datasets)</i>			
NCA-trained $\ell_2$	0.723	0.734	0.742
Shrunk Mahalanobis	0.632	0.683	0.717
Soft- $k$ NN ( $\ell_2$ , fitted $T$ )	0.837	0.837	0.837
Soft- $k$ NN (cos, fitted $T$ )	0.813	0.813	0.813

### B.2.7 Activation patching

Activation patching localizes the sites that carry the corruption. TabPFNv2 blocks  $\{0, 5, 9\}$  and TabICLv2 blocks  $\{\text{ColEmb-2, ICL-0, ICL-6, ICL-11}\}$  are patched on 10 datasets and 5 seeds, under block-0 KO and label-shuffle corruptions (Table 20). Every TabPFN block patch and every TabICL ICL-block patch recovers to baseline (recovery = 1.00). The single exception is TabICLv2’s ColEmb-2 under label-shuffle (recovery  $\approx 0.04$ ), consistent with ColEmb-2’s role as the compression bottleneck (§2.3). TabICL ICL blocks are unaffected by upstream block-0 KO because the column-embedding stack runs before the ICL stack and absorbs the perturbation, so corrupt and baseline are equal there (recovery is by definition 1.00).

Figure 3: **Where representation collapse appears in the public models.** Balance-scale accuracy (20 seeds, mean  $\pm$  s.d.) for each architecture (blue) and under symmetry-restoring ablations: removing TabPFNv2’s positional matrix or TabICLv2’s RoPE produces no measurable mean accuracy loss on this benchmark (green); disabling TabPFNv2’s pair channel or TabPFN v1’s RoPE reproduces the predicted collapse (red).

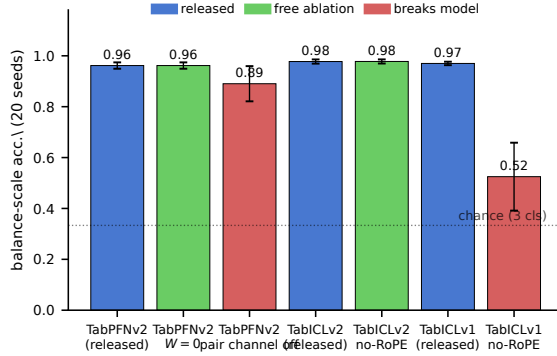


Table 20: Activation patching: replace activations at the named site in a corrupt run with those from a clean run, then read out accuracy. Mean across 10 datasets, 5 seeds. *Recovery* = (patched – corrupt)/(baseline – corrupt); 1.00 means the patched site fully restores baseline accuracy.

Site	Corruption	baseline	corrupt	patched	recovery
TabPFN B0	label-shuffle	0.874	0.497	0.874	1.000
TabPFN B5	label-shuffle	0.874	0.497	0.874	1.000
TabPFN B9	label-shuffle	0.874	0.497	0.874	1.000
TabICL ICL-0	label-shuffle	0.891	0.502	0.891	1.000
TabICL ICL-6	label-shuffle	0.891	0.502	0.891	1.000
TabICL ICL-11	label-shuffle	0.891	0.502	0.891	1.000
TabICL ColEmb-2	label-shuffle	0.891	0.502	0.538	0.043
TabPFN B0	block-0 KO	0.874	0.443	0.874	1.000
TabPFN B5	block-0 KO	0.874	0.443	0.874	1.000
TabPFN B9	block-0 KO	0.874	0.443	0.874	1.000
TabICL ICL-0	block-0 KO	0.891	0.892	0.891	1.000
TabICL ICL-6	block-0 KO	0.891	0.892	0.891	1.000
TabICL ICL-11	block-0 KO	0.891	0.892	0.891	1.000

### B.3 Representation collapse: stress tests, screen, and hand-crafted models

#### B.3.1 Stress test on collapse-prone data

Identical column marginals are the canonical setting in which TabPFNv2 and TabICLv2 risk producing indistinguishable row representations (cf. Qu et al., 2025). The stress test runs on three datasets: balance-scale; a synthetic identical-marginal benchmark ( $n = 1000, m = 20$ , fraction  $f \in \{0, 0.25, 0.5, 0.75, 1.0\}$  of columns drawn i.i.d. from the same 5-level discrete distribution, label a fixed nonlinear function of a labeled subset); and post-hoc real-data candidates from the JS-divergence screen of §I.6. The measured quantities are pairwise pre-readout cosine similarity, collapse rate (cross-class pairs with similarity  $> 0.99$ ), and KMeans- $C$  purity over 5 seeds. The conditions are: TabICLv1 (full vs. no-RoPE); TabICLv2 (full vs. no-RoPE vs. grouping-disabled); TabPFNv2 (full vs.  $W = 0$  vs. per-group feature count fixed to 1); and random-init controls. The full  $f$ -sweep with 10-seed paired-bootstrap CIs is in §I.7.

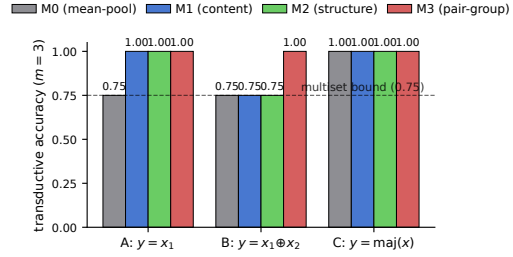
#### B.3.2 Marginal-similarity vs. invariance-cost correlation

Marginal similarity predicts the accuracy cost of removing the symmetry-breaker. For each of 49 datasets, pairwise JS divergence between column marginals identifies the maximum identical-marginal column set via thresholded clustering, and the accuracy gap between the full model and a strict permutation-invariant variant (TabPFNv2  $W = 0$ , TabICLv1 no-RoPE, TabICLv2 no-RoPE) gives the invariance cost. The prediction is a positive Spearman  $\rho$  on configurations whose ablation removes the symmetry-breaker, and  $\approx 0$  otherwise. Companion  $\rho$  at JS tolerances  $\tau \in \{0.01, 0.05, 0.10\}$  are reported in §I.6.

### B.3.3 Hand-crafted models: setup

The hand-crafted M0–M3 models referenced in §5.1 factor each architecture’s symmetry-breaking devices into a minimal single-layer setting.

Figure 4: **Hand-crafted models that isolate the three symmetry-breaking devices.** M0–M3 are single attention layers over  $m=3$  binary features (M0: shared-cell mean-pool; M1: column identifier; M2: per-column attention mask; M3: pair tokens). Transductive accuracy on Task A ( $y=x_1$ ), B ( $y=x_1 \oplus x_2$ ), C ( $y=\text{maj}(x)$ ). M0 is capped at the 0.75 multiset bound; M1, M2, M3 reach 1.0 on A; only M3 (pair tokens) breaks the bound on B; all four solve C. Derivations below.



The construction isolates the three symmetry-breaking devices (column identifier, column mask, pair grouping) on a task family where column-marginal information alone is useless. Let  $x \in \{0, 1\}^m$  and enumerate all  $2^m$  rows. Three tasks:

- Task A:  $y = x_1$  (one column is the label).
- Task B:  $y = x_1 \oplus x_2$  (two-column XOR).
- Task C:  $y = \text{majority}(x_1, \dots, x_m)$  (multiset-decidable control).

All features have identical Bernoulli(1/2) marginals. Each model is a single attention layer plus hard-argmax readout; transductive accuracy on the full  $2^m$ -row enumeration with  $m = 3$ . Numbers are exact rationals derived analytically and reproduced numerically; Table 21 records the verification.

### B.3.4 The multiset bound (Lemma 1)

**Lemma 1 (multiset bound, general orbit-majority form).** *Let  $r : \{0, 1\}^m \rightarrow \mathcal{R}$  be any row representation invariant to all column permutations:  $r(x) = r(\sigma x)$  for every  $\sigma \in S_m$ . Let  $g : \mathcal{R} \rightarrow \{0, 1\}$  be any deterministic readout, and let  $y : \{0, 1\}^m \rightarrow \{0, 1\}$  be any deterministic binary label rule. Then transductive accuracy of  $g \circ r$  on the  $2^m$ -row enumeration is at most*

$$\frac{1}{2^m} \sum_{O \in \{0,1\}^m / S_m} \max_{y_0 \in \{0,1\}} |\{x \in O : y(x) = y_0\}|,$$

*i.e. the orbit-wise majority of the label rule. The bound reduces to the formula previously stated for Task A ( $y(x) = x_1$ ); for  $m = 3$  binary targets it equals 0.75 and is exactly attained by M0.*

*Proof sketch.*  $S_m$ -invariance partitions  $\{0, 1\}^m$  into orbits on which  $r$ , and hence any deterministic readout  $g \circ r$ , is constant. Within an orbit  $O$  the readout cannot do better than the majority of  $\{y(x) : x \in O\}$ , contributing  $\max_{y_0} |\{x \in O : y(x) = y_0\}|$  correct predictions. Summing over the four  $m = 3$  orbits  $\{000\}, \{001, 010, 100\}, \{011, 101, 110\}, \{111\}$  for  $y(x) = x_1$  gives  $1 + 2 + 2 + 1 = 6/8 = 0.75$ .  $\square$

**Proposition 2 (Task B corollary).** *Any model with column-permutation-invariant row representation is capped at 0.75 on Task B for  $m = 3$ , even with an optimal linear readout: orbit  $\{001, 010, 100\}$  has XOR values  $\{1, 1, 0\}$  and  $\{011, 101, 110\}$  has  $\{1, 0, 1\}$ , so orbit-wise majority again caps at 6/8. The route assignment in Section 5.1 maps the M3 (pair-grouped) construction to the device that breaks this bound; M3 solves Task B at  $m = 3$  and is the smallest sufficient construction exhibited here.*

### B.3.5 M0–M3 model definitions

**M0 (shared embedding + mean-pool).**  $\phi(b) = b$ ;  $r(x) = \frac{1}{m} \sum_j x_j$ ; hard-NN readout.  $r$  is  $S_m$ -invariant. On Task A with  $m = 3$  each three-row orbit ties two labels against one, costing one error per orbit; transductive accuracy  $6/8 = 0.75$ , exactly meeting the bound.

**M1 (cell tokens with column identifier).** TabPFNv2-style: token  $t_{ij} = [v_{x_{ij}}; e_j; \ell_{y_i}]$  with column identifier  $e_j$ . With  $W_Q = W_K$  extracting (value, column) and cell-level scores  $s = 1[\text{value match}] + 1[\text{column match}]$ , argmax-with-ties readout followed by per-row mean over the  $m$  cells gives  $\hat{p}(100) = (1/3, 2/3)$ . Task A accuracy 1.0. Task B unsolved (single-cell attention cannot condition on two columns jointly).

**M2 (column-stream attention without identifiers).** TabICLv1-style: bipolar shared embedding  $\phi(b) = 2b - 1$ , per-column heads  $W_Q^{(j)} = W_K^{(j)} = e_j^\top$  (mask = column structure), per-row mean over  $m$  heads. M2 = M1 on this family: restricting M1 attention to matching columns and M2’s per-column head yield identical softmaxes, and per-row means coincide. Task A 1.0, Task B 0.5.

**M3 (pair-grouped tokens).** v2-grouping: each super-cell over an unordered feature pair  $(j, k)$  carries the joint value  $u_{(j,k)} = 2x_j + x_k \in \{0, 1, 2, 3\}$  and a pair identifier  $e_{(j,k)}$ . On Task A with  $m = 3$ , the super-cell at  $(x_1, x_2) = (1, 0)$  appears in five positives and one negative, so  $\hat{p}(100) = (1/6, 5/6)$  and Task A accuracy is 1.0. Conditioning on the joint value of  $(x_1, x_2)$  separates XOR; Task B accuracy 1.0.

### B.3.6 Verification table and architecture mapping

Table 21: Transductive accuracy of the four handcrafted models on Tasks A, B, C with  $m = 3$ , verified numerically.

Model	Task A	Task B	Task C
M0 naïve	0.75	0.75	1.00
M1 TabPFN-style	1.00	0.50	1.00
M2 TabICLv1-style	1.00	0.50	1.00
M3 pair-grouped	1.00	1.00	1.00

Table 22: Route assignment per architecture. Each model carries two of the three routes (M1: cell+col-ID; M2: column-stream; M3: pair-group); ablating one route leaves the other intact, predicting the small empirical ablation costs measured in §4.

Architecture	Routes	Missing route
TabPFN v2	M1 + M3	column-stream (M2)
TabICLv1	M2 + within-row RoPE	pair-group (M3)
TabICLv2	M2 + M3	cell+col-ID (M1)
Mitra	shared embedding + no PE	— (column-invariant by construction)

Mapping: TabPFNv2 pairs M1 (random per-feature identifiers) with M3 (pair grouping); TabICLv1 pairs M2 (column-stream attention) with RoPE; TabICLv2 pairs M2 with M3 (circular grouping) and adds target-aware embeddings. Each v2 architecture carries *two* of the three routes; TabICLv1 carries only one. This predicts the empirical pattern of §5.2: TabPFNv2 with  $W = 0$  and TabICLv2 without RoPE both show no measurable accuracy loss, while disabling TabPFNv2’s pair channel costs  $-7$  pp on balance-scale and  $-14$  pp under full identical-marginal stress (§1.7); TabICLv1 without RoPE loses  $-44$  pp on balance-scale and  $15$  pp on the benchmark mean. The load-bearing v2 mitigation is the M3 pair/circular-grouping route.

### B.3.7 Attention-mode ablation

A sweep over shared-embedding, oracle-attention, and attention-mode combinations (row-level ICL, cell-level cross-attention, column-stream) on Tasks A–C under leave-one-out separates the contributions of each mechanism. Row-level ICL on collapsed representations caps at 0.625 on Task A LOO; cell-level cross-attention without column identifiers drops to 0.25; column-stream reaches 1.0 on Task A even with shared embeddings. Task B remains at chance for every single-layer mode, consistent with XOR requiring at least one nonlinear interaction.

### B.3.8 Fresh non-linear head on the frozen final representation

A 1-hidden-layer GELU MLP head ( $d_{\text{hidden}}$  matched to the original decoder’s first hidden width: 192 for TabPFNv2, 512 for TabICLv2) is retrained on each backbone’s frozen final representation, using the context split for fitting and the held-out query split for accuracy (LBFGS / AdamW; protocol matches §A.2). The linear-head row of §3.4 is the same protocol with  $d_{\text{hidden}}=0$  (a bare logistic layer). Across the 42 shared datasets where both methods completed, the linear head reaches mean 0.582 on TabPFNv2 (−26.5 pp vs. native, 95% paired bootstrap CI [−34.7, −19.1], worse on 39/42) and the MLP head reaches 0.598 (−24.9 pp, [−32.5, −18.0], worse on 38/42, exact two-sided binomial sign test  $p \approx 3 \times 10^{-8}$ ); on TabICLv2 the same heads reach 0.849 (−0.7 pp, [−1.2, −0.3]) and 0.847 (−0.8 pp, [−1.5, −0.3]). The non-linear head gains roughly 1.6 pp on TabPFNv2 relative to the linear head while leaving a  $\sim 25$  pp gap to native, and is statistically indistinguishable from the linear head on TabICLv2. The fresh-head asymmetry between the two backbones survives the addition of a single-hidden-layer non-linearity.

## C TabICL classification: full results

This appendix collects the full TabICLv2 classification evidence behind the main-text claims of §2 and §3.3: column-embedding ablations, ICL-block knockouts and uniform-attention sweeps, label perturbations, the per-layer linear and  $k$ NN probes, and the readout grid that compares the end-to-end head against per-layer prototype,  $k$ NN, and per-block-vote decoders, including a cross-version comparison over the released TabICL v1, v1.1, and v2 classifiers.

### C.1 Where the class-readable representation is laid down

#### C.1.1 ColEmbedding knockouts

Zeroing each ColEmbedding block (ColEmb-0/1/2) on 49 datasets: ColEmb-2 is most damaging on 45 of 49. ColEmb-2 is the SetTransformer readout that compresses per-feature into per-sample vectors.

Table 23: TabICL ColEmbedding-block knockouts: mean accuracy drop across 49 classification datasets, baseline 0.86.

Knockout	$\Delta$ acc	most-damaging datasets
ColEmb-0	−0.03	4 / 49
ColEmb-1	−0.01	0 / 49
ColEmb-2	−0.28	45 / 49

**ColEmb-2 sets the coordinate frame.** To mirror the TabPFN block-0/block-9 analysis (§B.1.3) we evaluate two probe types under each early-block knockout: a *frozen* probe trained on the intact model and applied without retraining, and a *retrained* probe fit from scratch on the post-knockout train representations. Probes are read off at L−1 (input to the ICL stack) and L11 (final ICL block); 49 classification datasets, 5 seeds. Knocking out ColEmb-2 collapses the final accuracy by 28 pp and the frozen probe at L−1 by 26 pp, but the retrained probe at L−1 loses only 6 pp (0.812  $\rightarrow$  0.752, well above the multi-class chance level). Class information survives the perturbation; the downstream ICL stack cannot read the post-KO frame. At L11 the retrained probe (0.602) sits below the frozen probe (0.704) under ColEmb-2 KO, so the late representation no longer organizes class structure linearly even when refit. ColEmb-0 and ColEmb-1 produce the same qualitative pattern (frozen  $\ll$  retrained at L−1) at much smaller magnitude, consistent with their role as upstream contributors to the same coordinate-setting role. Knocking out a single ICL block (L0, L5, or L11) leaves both probe types within 3 pp of baseline, matching the redundancy reported in §3.3.

Table 24: TabICL frozen-vs-retrained probe under each early-block knockout, mean across 49 classification datasets  $\times$  5 seeds. Frozen probes are trained on the intact model and applied without retraining; retrained probes are fit from scratch on post-knockout train representations. L-1 is the input to the ICL stack (output of ColEmb+RowInteraction); L11 is the final ICL block.

Knockout	Final acc	$\Delta$	Frozen probe		Retrained probe	
			L-1	L11	L-1	L11
Baseline (intact)	0.864	—	0.812	0.859	0.812	0.859
ColEmb-0	0.836	-0.028	0.583	0.827	0.787	0.824
ColEmb-1	0.849	-0.014	0.655	0.843	0.806	0.843
ColEmb-2	0.583	-0.281	0.555	0.704	0.752	0.602
ICL-L0	0.860	-0.004	0.812	0.854	0.812	0.852
ICL-L5	0.845	-0.018	0.812	0.830	0.812	0.827
ICL-L11	0.863	-0.001	0.812	0.855	0.812	0.859

### C.1.2 RowInteraction skips

Skipping each RowInteraction block individually leaves the ICL-input linear probe at 81%, essentially unchanged from the intact representation: RowInteraction does not create the class structure. Two further checks corroborate this. The per-layer  $\ell_2$ - $k$ NN curve of Tab. 25 already sits within 4 pp of its L11 endpoint at L0, immediately after the first row-interaction attention. The uniform-attention combinations in §C.2.3 cost 5–13 pp on average when applied to contiguous halves of the stack. Both align with the main-text claim that removing between-row mixing in the column-embedding network costs only a few points.

### C.1.3 ICL input probe by dataset

We measure class-readability per layer with  $\ell_2$ - $k$ NN agreement on the representations rather than with geometry summaries: the TabICL stack does not bottleneck (the rank/PR profile in §2.2 is monotone-increasing through most of the stack) so geometry alone is uninformative about *when* class structure becomes readable, while  $k$ NN agreement directly tracks the quantity the prototype/ $k$ NN readout (§3.3) consumes. Across 49 datasets the  $k$ NN-on-representation accuracy is already 0.824 at the output of the first ICL block (L0), within 4 pp of end-to-end (0.864); the curve gains  $\leq 0.04$  over the entire stack.

Table 25: Per-layer  $\ell_2$ - $k$ NN on TabICLv2 representations across 49 datasets ( $k=5$ , mean  $\pm$  std across datasets). TabICLv2 baseline  $0.864 \pm 0.153$ . Class structure is laid down by L0 and only mildly sharpened.

Layer	L0	L1	L2	L3	L4	L5	L6	L7	L8	L9	L10	L11
$k$ NN acc	.824	.825	.827	.829	.835	.832	.837	.837	.847	.849	.855	.856
agreement	.885	.885	.890	.886	.897	.894	.901	.902	.923	.924	.935	.936

Per-dataset peak-layer (argmax of  $k$ NN accuracy across L0–L11): median peak L10; only 5/49 datasets peak at L0 and 1/49 at L1, while 27/49 peak at L10 or L11. Class structure is laid down by L0 (within 4 pp of end-to-end on average) and only mildly sharpened by the rest of the stack, consistent with the qualitative claim in the main text.

## C.2 Attention and label interventions

### C.2.1 Label interventions

Five context-set label perturbations are applied at inference on the 49-dataset classification suite. Tab. 26 reports the per-dataset change in TabICLv2 accuracy and in the linear probe of the ICL representation after each perturbation: labels are essential, their specific learned directions matter, and they act as class identities rather than positional indices.

Table 26: Label-perturbation effects on TabICLv2-cls.  $\Delta$  acc is the change in end-to-end accuracy; probe is the ICL-representation linear probe accuracy after the perturbation.

Intervention	$\Delta$ acc	probe	note
Remove (zero)	-44 pp	0.81→0.12	labels are essential
Cyclic shift $k \rightarrow k+1$	-0.01 pp (med.)	unchanged	41/49 within $\pm 1$ pp
Two-class swap	-76 pp <sup>†</sup>	—	<sup>†</sup> on swapped classes only
Random Gaussian	→ chance	collapsed	learned directions matter
Shuffle within context	→ chance	collapsed	order-agnostic role broken

### C.2.2 Single-block uniform attention

Single-block and two-block uniform row-attention leaves TabICLv2 within a few points of baseline. We force uniform row-attention at one ICL block (block 0 or block 11) or at one sliding two-block window (blocks  $X, X+1$  for  $X=0 \dots 10$ ). Across 49 datasets and 10 seeds, no single block and no two-block window costs more than a few points on average; at least 46/49 datasets stay within  $|\Delta| < 1$  pp at every window. The matching TabPFNv2 L9 uniform-attention drop is  $-0.39$  (§B.2.5).

Table 27: Single-block (top) and sliding two-block (bottom) uniform row-attention drops on TabICLv2, 49 datasets, 10 seeds. Drop is baseline–accuracy; the rightmost column counts datasets with  $|\Delta| < 0.01$ .

Block(s)	mean drop	median	worst	$n(\leq 1\text{pp})/49$
b0	+0.023	+0.009	+0.180	39
b11	+0.002	+0.000	+0.028	47
pair 0–1	+0.039	+0.013	+0.217	49
pair 1–2	+0.023	+0.007	-0.031	48
pair 2–3	+0.018	+0.007	-0.015	48
pair 3–4	+0.014	+0.006	-0.015	48
pair 4–5	+0.007	+0.003	-0.026	47
pair 5–6	+0.005	+0.001	-0.019	47
pair 6–7	+0.004	+0.002	-0.022	48
pair 7–8	+0.010	+0.004	-0.020	48
pair 8–9	+0.015	+0.007	-0.022	46
pair 9–10	+0.022	+0.011	-0.019	47
pair 10–11	+0.017	+0.008	-0.019	47

### C.2.3 Multi-block uniform attention

Forcing uniform attention on {first-6, last-6, all-12} blocks (49 datasets, 10 seeds, plus sign\_1d):

Table 28: TabICL accuracy under simultaneous uniform-attention knockout of contiguous block groups. Mean accuracy across 49 datasets  $\times$  10 seeds, with the sign\_1d synthetic control reported separately. Neither half of the stack alone breaks the model; only the all-12 condition collapses both real-data and synthetic accuracy.

Condition	Mean accuracy	sign_1d
Baseline	0.862	0.993
First 3 blocks	0.810	—
Last 3 blocks	0.804	—
First 6 blocks	0.789	—
Last 6 blocks	0.737	—
All 12 blocks	0.572	0.533

Last-6 is more damaging than first-6; neither half alone breaks the model. All-12 drops accuracy by  $-29$  pp and collapses sign\_1d from 0.993 to 0.533. Excluding sign\_1d, all-12 has max 0.777, median 0.290 across 48 datasets, above the majority baseline (mean 0.498, §I.11). The blocks are collectively necessary and individually redundant.

### C.2.4 MLP knockouts

Zeroing one ICL MLP (second linear layer) per block (49 datasets, 5 seeds). Mean accuracy drop  $\leq 2.0$  pp at every block; the single largest per-dataset drop anywhere in the stack is 8.7 pp (block 7) and 29.9 pp (block 8 on one outlier). No single MLP is critical. Regression shows a different pattern at L11 (§F.4).

Table 29: Per-block ICL-MLP knockout drops on TabICLv2-cls (49 datasets, baseline 0.864). Mean and median drops are sub-percent at every block; the worst single dataset drop never exceeds 0.30.

Block	mean drop	median	worst (min)	best (max)
b0	-0.001	-0.001	-0.028	+0.033
b1	-0.004	-0.001	-0.033	+0.022
b2	-0.004	-0.001	-0.059	+0.026
b3	-0.016	-0.006	-0.082	+0.015
b4	-0.007	-0.004	-0.056	+0.015
b5	-0.009	-0.005	-0.062	+0.012
b6	-0.009	-0.002	-0.061	+0.029
b7	-0.004	-0.001	-0.087	+0.020
b8	-0.020	-0.003	-0.299	+0.014
b9	-0.003	-0.002	-0.033	+0.047
b10	-0.002	-0.001	-0.031	+0.027
b11	+0.001	+0.000	-0.009	+0.009

## C.3 The final-representation readout

### C.3.1 Prototype-classifier readout

Prototype classifiers at each ICL layer ( $-1$ =ICL input,  $0 \dots 11$ =block outputs): per-class centroids decoded via  $\text{softmax}(-d(\mathbf{z}, \boldsymbol{\mu}_c))$  (49 datasets, 5 seeds; baseline 0.864).  $\ell_2$  and cosine prototypes track each other to  $\leq 0.002$  at every layer and reach 0.854/0.854 at L11 vs. 0.864 end-to-end; the learned head adds  $\leq 1.0$  pp. Calibration analysis (§I.14): learned head, L11-prototype, and L11- $k$ NN agree within  $\sim 1$  pp accuracy and 0.92–0.93 pairwise.

Table 30: Per-layer prototype classifier accuracy on TabICLv2-cls (49 datasets, 5 seeds; baseline 0.864). Layer  $-1$  is the ICL input (column-embedding output).  $\ell_2$ /cosine are interchangeable.

Layer	-1	0	1	2	3	4	5	6	7	8	9	10	11
$\ell_2$	.735	.761	.772	.790	.804	.814	.823	.830	.828	.834	.846	.852	.854
cosine	.734	.760	.772	.791	.802	.813	.822	.830	.831	.832	.845	.851	.854

### C.3.2 Cross-version readout checks: TabICL v1 and v1.1

We rerun the readout grid on the TabICL v1 and v1.1 classifiers over the full 49-dataset classification suite (5 seeds per dataset) to check whether the prototype/ $k$ NN picture is specific to the v2 release. The qualitative ordering survives across all three releases (Tab. 31): L11-prototype and L11- $k$ NN remain close to native accuracy, while the sharpest-block vote is far worse. Calibration is descriptive only: the v1 native / prototype /  $k$ NN / sharp-vote ECE–NLL pairs are 0.047/0.339, 0.416/1.022, 0.135/3.315, and 0.213/0.893; the matching v1.1 pairs are 0.050/0.336, 0.433/1.051, 0.130/3.186, and 0.196/0.821. The final-representation prototype/ $k$ NN picture holds across the released TabICL classifiers and is not an artefact of the v2 release.

Table 31: Readout-grid comparison across three released TabICL classification models on the 49-dataset classification suite (5 seeds / dataset). Values are means over per-dataset seed means.

Release	native	L11-prototype	L11- $k$ NN	sharp-vote
v2	0.864	0.854	0.856	0.470
v1.1	0.852	0.830	0.842	0.626
v1	0.852	0.828	0.836	0.590

### C.3.3 Proximity-corrected within-class preference

At each ICL block: raw within-class attention minus expected value conditioned on feature proximity (bootstrap resampling). Across 49 datasets, 0 show positive corrected preference; 43 are significantly negative ( $\alpha=0.05$ ). Attention does not seek same-class rows; geometry is laid down upstream.

### C.3.4 Distance correlations

Spearman  $\rho$  between attention weights and pairwise distances (feature-space  $\ell_2$ , representation-space  $\ell_2$ , label-embedding cosine):  $< 0.08$  at all ICL blocks. Attention does not implement distance-based retrieval.

### C.3.5 $k$ NN agreement with TabICL

$k$ NN on the L11 representation and on the raw input,  $k \in \{1, 3, 5, 10\}$ , four metrics, 49 datasets, 10 seeds. TabICLv2 accuracy:  $0.864 \pm 0.155$ .  $\ell_2$ /cosine on the final representation match TabICLv2 to within 1 pp and agree with it on  $\sim 94\%$  of test queries; Mahalanobis underperforms because of covariance estimation under small context; raw-input  $\ell_2$  is a non-trivial  $\sim 78\%$ . Converse pattern of TabPFNV2 (§B.2.6).

Table 32:  $k$ NN accuracy / agreement with TabICLv2 predictions, by metric and  $k$  (49 datasets, 10 seeds, baseline 0.864).

Metric	$k=1$	$k=3$	$k=5$	$k=10$
rep $\ell_2$	.855 / .933	.856 / .938	.857 / .938	.858 / .941
rep cosine	.855 / .932	.856 / .936	.857 / .939	.858 / .941
rep Maha.	.652 / .672	.678 / .702	.689 / .714	.700 / .729
input $\ell_2$	.749 / .788	.764 / .806	.772 / .817	.776 / .828

### C.3.6 Per-block vote refutation

Each ICL block decoded through final output projection as a per-block vote (10 datasets, 5 seeds):

Table 33: TabICL per-block vote refutation. Each block’s hidden state is decoded through the final output projection. Best block is L9 with Pearson  $r = 0.462$ , far below TabPFN’s vote correlation of 0.888. Mean across 10 datasets  $\times$  5 seeds.

Layer	Pearson $r$	Vote Acc	Agreement	$N$
L0	0.306	0.467	0.491	10
L1	0.376	0.525	0.552	10
L3	0.169	0.412	0.435	10
L6	0.367	0.554	0.582	10
L9	0.462	0.584	0.612	10
L11	0.230	0.442	0.468	10

Best block: L9,  $r(\text{vote, final})=+0.462$ , agreement 0.612, vote-acc 0.584 vs. true  $\approx 0.864$ . Other blocks:  $r=+0.169$  (L3) to  $+0.376$  (L1); vote-acc never exceeds 0.584. Refutes per-block vote hypothesis. Contrast TabPFNV2: L9 vote tracks final at  $r=0.888$  (§B.2.3). Regression confirms (§I.2).

## D Mitra audit details

This appendix collects the per-experiment details for Mitra referenced from the main text. Mitra’s architecture is described alongside TabPFNV2 and TabICLv2 in §A.1; the load-bearing differences for our analysis are the separate per-row label slot, the shared per-feature embedding, and the absence of positional encoding on either axis. We audit both released checkpoints (v1 and v1.1) on the same 49-dataset classification and 10-dataset regression suites used throughout the paper. All experiments are run offline against local checkpoints; Mitra is loaded as a single model with ensembling/stacking

disabled, so the AutoGluon defaults that would wrap it in a meta-ensemble are explicitly turned off and we measure the model in isolation.

### D.1 Permutation invariance (§4)

Mitra is exactly invariant to row *and* column permutations up to floating-point noise; per-class label invariance fails as expected because the label slot uses a per-class embedding.

Table 34: Permutation invariance summary. Quantitative measurements across 48 datasets that load under the per-class minimum-sample filter, 20 random permutations per dataset, fp32 inference: mean  $|\Delta p|$  is below 0.3% for both row and column on both Mitra versions; the mean per-dataset *maximum*  $|\Delta p|$  is 1–3%; predicted-label agreement is  $\geq 99.5\%$ . Per-class relabelling produces mean maximum  $|\Delta p| \approx 18\text{--}20\%$  with label agreement  $\approx 0.96$ .

	Row	Column	Label (per-class)
TabPFNv2	yes (architectural)	no	no
TabICLv2	yes (architectural)	no (RoPE)	no
Mitra v1	<b>yes (architectural)</b>	<b>yes (architectural)</b>	no
Mitra v1.1	<b>yes (architectural)</b>	<b>yes (architectural)</b>	no

The exact column invariance follows mechanically from the shared per-feature embedding plus the absence of any positional encoding: column attention sees feature tokens as a set, so feature reordering is exactly a no-op up to numerical reduction order. TabPFNv2 and TabICLv2 do not have this property because both inject feature identity (the TabPFNv2 per-feature embedding  $W_p$  and TabICLv2’s RoPE).

### D.2 Layerwise representation analysis (§2)

We attach forward hooks on each `Layer.forward` of Mitra’s transformer and capture both the context and query streams. Mean-pooling along the feature axis (skipping the  $y$ -slot at position 0) gives one vector per row per layer. We then evaluate four per-layer readouts on the resulting features: a logistic regression linear probe on standardised features, a class-mean prototype rule, cosine-distance 5-NN, and the agreement of the 5-NN prediction with Mitra’s native prediction. 45 of the 49 datasets load under Mitra’s per-class minimum-sample filter.

Table 35: Layerwise probe summary on the 45-dataset subset. Both Mitra versions peak at L9, mirroring the TabPFNv2 late-jump pattern rather than TabICLv2’s early convergence.  $k$ NN agreement at the peak is 0.82–0.83 and falls to 0.71–0.78 by L12 (Table 36).

version	$n_{\text{datasets}}$	e2e mean acc	peak-probe layer	$k$ NN-agreement @ L9
v1	45	0.827	L9 (0.777)	0.831
v1.1	45	0.825	L9 (0.784)	0.821

Table 36: Per-layer probe / prototype / cosine 5-NN / 5-NN-agreement on Mitra, mean over the 45-dataset subset. Probe peaks at L9 in both versions, with the characteristic L10 refinement-phase dip and partial recovery at L11–L12.  $k$ NN tracks the probe within  $\sim 2$  pp at L9; the prototype rule is weaker, especially for v1.1 (gap  $\sim 6$  pp).

layer	v1 (45 datasets)				v1.1 (45 datasets)			
	probe	proto	$k$ NN5	$k$ NN-agree	probe	proto	$k$ NN5	$k$ NN-agree
L1	0.576	0.533	0.592	0.640	0.430	0.462	0.500	0.525
L2	0.681	0.652	0.690	0.746	0.519	0.522	0.579	0.611
L3	0.698	0.677	0.695	0.763	0.667	0.673	0.697	0.758
L4	0.713	0.693	0.716	0.791	0.672	0.673	0.698	0.762
L5	0.731	0.712	0.731	0.808	0.746	0.722	0.756	0.833
L6	0.752	0.734	0.753	0.837	0.761	0.736	0.756	0.835
L7	0.759	0.751	0.763	0.845	0.771	0.737	0.764	0.847
L8	0.771	0.745	0.759	0.836	0.774	0.723	0.754	0.831
L9	<b>0.777</b>	0.742	0.759	0.831	<b>0.784</b>	0.721	0.755	0.821
L10	0.718	0.684	0.704	0.750	0.702	0.656	0.664	0.700
L11	0.753	0.739	0.769	0.830	0.685	0.655	0.657	0.671
L12	0.676	0.683	0.733	0.777	0.673	0.646	0.688	0.706

### D.3 Per-block knockouts (§2.3)

We replicate the per-block knockout protocol of §B.1.2 on Mitra. Each interleaved row/feature Layer is replaced one at a time with the identity (a forward pre-hook returning its inputs unchanged); the rest of the network runs normally, and we report the resulting accuracy on the same 49 datasets as §D.1, with 300 context and 200 query rows per dataset.

Layer 0 is the most damaging single intervention on both checkpoints, by a margin: it costs a mean of 15.8 pp on v1 and 41.1 pp on v1.1, while the runner-up block costs  $\leq 2$  pp on v1 and 19.6 pp on v1.1 (Layer 1). Layer 0 is the worst single block on 31/49 datasets for v1 and 36/49 for v1.1; no other block is the worst on more than three datasets in v1 or one in v1.1. The remaining eleven blocks each cost 1–3 pp in mean drop, with no late-layer organizing spike comparable to TabPFNv2’s block 9 (§B.1.3); consistent with the geometric, late-jumping readout reported in §3.2, where a single late layer (L9) suddenly aligns with the attention-weighted vote. The asymmetry between v1 and v1.1 mirrors the per-layer probe pattern of §36: v1.1 compresses class structure into the early frame more aggressively than v1, and pays for it more under early-block ablation.

### D.4 Readout fidelity (§3)

On the full 49-dataset classification grid (1 seed/dataset, v1), Mitra’s native head reaches mean accuracy 0.860. At L9, the attention-weighted vote (defined below) reaches 0.815 ( $-4.5$  pp, mean Pearson  $r=0.89$  vs. native), the cosine 5-NN readout reaches 0.789 (within  $\sim 1.5$  pp of the L9 linear probe at 0.776), and the class-mean prototype rule reaches 0.769. Vote leads  $k$ NN by 2.6 pp and prototype by 4.6 pp on accuracy; argmax-agreement of  $k$ NN with Mitra’s native predictions at L9 is 0.82–0.83, and  $k$ NN tracks the linear probe within  $\sim 2$  pp through the entire L5–L9 window where both rise monotonically (Table 36). All three rules are retrieval-over-context-rows surrogates and are consistent with the row-attention ablation (§D.6); among them the L9 vote is the closest match to the native head and is reported as Mitra’s readout in §3. Cosine  $k$ NN is reported as a parameter-free diagnostic.

**Layer choice (v1 vs. v1.1).** On v1 weights, the vote-faithful and probe-faithful layers coincide at L9: a layerwise sweep of vote accuracy on the 45-dataset subset of Table 36 shows L9 at the joint optimum, with L8 and L10 within 0.2 pp and L12 within 0.2 pp (0.779, 0.778, 0.777, 0.778 respectively; L11 underperforms by  $\sim 7$  pp). On v1.1, the vote-faithful layer shifts to the final attention block: L12 vote reaches 0.810 (gap  $-3.4$  pp, agree 0.89,  $r=0.89$ ) on the 42-dataset OpenML grid, while L9 underperforms L12 by  $\sim 7.7$  pp. We use v1 throughout the main text so that the same layer L9 surrogates both attention vote and the linear probe.

**Attention-weighted vote at L9.** Mitra’s `MultiheadAttention` dispatches to `F.scaled_dot_product_attention`, which does not expose the attention weights, so we

wrap `layer.attention1.forward` at L9 to additionally compute  $\text{softmax}(QK^\top/\sqrt{d_h})$  on the cross-attention call (query rows attending over context rows) without altering the returned tensor or Mitra’s predictions. Averaging the resulting weights over heads and over the per-feature row-attention slices and forming the attention-weighted vote  $\text{vote}[t, c] \propto \sum_{i: y_i^{\text{ctx}}=c} \bar{a}_{t,i}$ , the L9 vote rule reaches mean accuracy 0.815 on the full 49-dataset grid (vs. native 0.860, gap 4.5 pp; mean Pearson  $r$  vs. native probabilities 0.89). The same construction restricted to the  $y$ -slot of the row-attention reshape is *worse*, not better, at every layer (best  $\sim 0.74$  at L12 on v1.1), because column attention mixes  $y$ -slot and feature-slot information within each observation, leaving the per-feature average more stable than any single slot.

### D.5 Adversarial probes (§6)

We port the full attack battery used for TabPFNv2 and TabICLv2 (§H) to Mitra: random-label padding (2× and 4×), boundary poisoning, hub poisoning, class-centroid injection, monotone distortions (cube / softexp / rank), and the adversarial low-variance rotation. The same 49-dataset suite, splits, and Ridge baseline are used.

Table 37: Mean accuracy drop relative to the unattacked baseline, 49 datasets. “Worse than R.” counts datasets on which Mitra ends below Ridge after the attack.

attack	Ridge $\Delta$	Mitra v1 $\Delta$	v1 worse than R.	Mitra v1.1 $\Delta$	v1.1 worse than R.
pad2x	−0.047	−0.049	7/49	−0.032	6/49
pad4x	−0.081	−0.075	11/49	−0.054	8/49
boundary	−0.021	−0.028	11/49	−0.016	9/49
hub poisoning	−0.012	−0.021	<b>14/49</b>	−0.022	<b>11/49</b>
centroid inj.	−0.002	+0.001	6/49	+0.000	7/49
mono cube	−0.022	−0.000	5/49	−0.001	3/49
mono softexp	−0.043	−0.044	7/49	−0.045	7/49
mono rank	−0.042	−0.000	3/49	−0.003	3/49
rotate (low- $\sigma$ )	−0.001	−0.006	10/49	−0.001	7/49

Mitra is uniformly more robust than Ridge under monotone distortions (cube, rank): essentially zero drop where Ridge gives up 2–4 pp. Pad-style and rotation attacks degrade Mitra comparably to Ridge. Hub poisoning is the clearest case where Mitra ends below Ridge on a substantial fraction of datasets (14/49 on v1, 11/49 on v1.1); boundary poisoning and rotation also produce non-trivial worse-than-Ridge counts but with smaller mean drops. The hub-poisoning pattern is consistent with the vote-faithful readout established in §D.4: inserting label-anchored hubs in the context directly perturbs the context-similarity signal that the readout relies on.

### D.6 Collapse mechanism (§5)

Mitra does not exhibit representation collapse on balance-scale or on a  $d=12$  *balance-like* synthetic dataset (Table 38). We further perform the analogue of the TabPFNv2/TabICLv2 double ablation by zeroing each of Mitra’s two attention paths (`Layer.attention1`: row attention; `Layer.attention2`: column attention) via verified forward hooks — a per-call counter confirms the hook fires — and measuring the resulting accuracy.

Table 38: Mitra accuracy on the canonical balance-scale stress test and a  $d=12$  balance-like variant. No collapse is observed in either version.

version	balance-scale (3 seeds)	balance-like, $d=12$ (3 seeds)
v1	0.961 ± 0.007	0.893 ± 0.025
v1.1	0.959 ± 0.014	0.969 ± 0.003
majority baseline	0.436	$\sim 0.47$

Table 39: Double ablation of Mitra’s attention paths. “row\_off” zeroes `Layer.attention1` on every layer; “col\_off” zeroes `Layer.attention2`. Removing row attention drops accuracy from  $\sim 0.95$  to 0.08, well below the majority baseline, indicating a systematic misclassification regime rather than collapse to majority. Removing column attention collapses to near-majority. Removing both lands at the “row\_off” level.

version	dataset	full	row_off	col_off	both_off
v1	balance-scale	<b>0.954</b>	0.080	0.459	0.080
v1	balance-like-d12	<b>0.893</b>	0.074	0.459	0.074
v1.1	balance-scale	<b>0.963</b>	0.080	0.461	0.080
v1.1	balance-like-d12	<b>0.969</b>	0.074	0.467	0.074
majority baseline		$\sim 0.46$ (balance-scale), $\sim 0.47$ (balance-like)			

The collapse-critical mechanism for Mitra is therefore *row attention*, the only one of the three families for which the critical mechanism is itself permutation-symmetric: TabPFNv2’s is the feature-positional pathway  $W_p$ , TabICLv2’s is RoPE on the row axis, and Mitra’s is the cross-row aggregator. Combined with the vote-faithful readout (§D.4), this picture is consistent with the differential vulnerability to hub poisoning observed in §D.5: corrupting label-anchored hubs perturbs the context-similarity signal that flows through exactly the row-attention path the ablation here identifies as load-bearing. We do not claim direct causal attribution from the balance-scale ablation to the hub-poisoning result — the two experiments use different datasets and stress different operating regimes — only that both point at row attention as the natural locus of failure.

## D.7 Three-way contrast

Table 40: Three-way comparison across the dimensions audited in this paper. Mitra’s *compute schedule* is TabPFNv2-like (late jump in depth), its *readout family* is also TabPFNv2-like (attention-weighted vote at L9), and its *symmetry profile* is strictly stronger than both — column invariance is exact by construction.

dimension	TabPFNv2	TabICLv2	Mitra
Token factorization	feat $\oplus$ label per token	feat $\oplus$ label per token	separate $y$ -slot per row
Positional structure	per-feature $W_p$	RoPE on feature axis	none
Row invariance	yes	yes	yes
Column invariance	no	no (RoPE)	<b>yes (exact, no patch)</b>
Per-class label invariance	no	no	no
Probe peak layer	late (L9)	early (L2–L4)	late (L9)
Faithful surrogate (cls)	attention vote @ L9	class-mean prototype @ L11	attention vote @ L9
Hub-poisoning vulnerability	yes	yes	yes
Monotone-distortion (rank/cube)	low	low	lowest
Balance-scale collapse	no	sometimes (v1)	no
Critical mechanism (ablation)	feat-pos $W_p$	RoPE	<b>row attention</b>
Critical mech. permutation-symm.	no	no	<b>yes</b>

**Summary.** Mitra is its own combination of design choices. Token-level factorization of features and labels, a shared per-feature embedding, and the absence of positional encoding together make it the only one of the three families for which column invariance is exact, the cosine- $k$ NN readout is the closest similarity-based surrogate to native predictions of the three families (§3), and the collapse-critical mechanism uncovered by ablation is itself permutation-symmetric. Empirically, this combination delivers full robustness to monotone feature distortions (cube, rank) and no balance-scale collapse, while preserving the same hub-poisoning weakness as TabPFNv2/TabICLv2. Two ablations are consistent with the mechanistic narrative for Mitra: the row-attention zero-out (Table 39) and the hub-poisoning attack (Table 37); the connection between them remains an inference rather than a single end-to-end intervention.

## E TabPFN regression: full results

Regression measurements cover 10 datasets with 5 seeds each unless noted. The subsections that follow trace the late-readout circuit from classification through regression: per-block representation geometry, row-attention sharpness, activation patching, the L9 attention-vote test, and the MLP-knockout and uniform-attention falsification controls. Two systematic shifts emerge against the classification baseline — the probe peak moves one layer earlier and row-attention is substantially softer — both consistent with the bias–variance trade-off of continuous targets.

### E.1 Per-block representation geometry

Per-block geometry on regression matches the classification profile. Table 41 reports per-block effective rank (ER), participation ratio (PR) and 2-NN intrinsic dimension (ID) averaged across the 10 regression datasets. The L2 block triggers a sharp ER collapse ( $ER \approx 9.5$ ,  $PR \approx 1.5$ ), L3–L8 rebuild the representation gradually, and L9–L11 reach maximum ER and PR where the readout forms. Intrinsic dimension contracts from  $ID \approx 8.0$  at L1 to a 3.4–3.7 plateau from L6 onward, exposing a low-dimensional predictive manifold.

Table 41: Per-block geometry on TabPFN-reg, mean $\pm$ std across 10 regression datasets (5 seeds each).

Block	Effective rank	Participation ratio	2-NN ID
L0	78.7 $\pm$ 15.0	3.60 $\pm$ 0.81	5.54 $\pm$ 1.16
L1	86.9 $\pm$ 15.9	4.68 $\pm$ 1.14	7.99 $\pm$ 2.45
L2	9.5 $\pm$ 0.6	1.47 $\pm$ 0.18	3.49 $\pm$ 0.75
L3	22.6 $\pm$ 2.0	3.06 $\pm$ 0.29	3.76 $\pm$ 1.29
L4	30.1 $\pm$ 4.0	2.76 $\pm$ 0.40	4.22 $\pm$ 1.63
L5	26.6 $\pm$ 3.9	2.91 $\pm$ 0.61	3.72 $\pm$ 1.38
L6	32.8 $\pm$ 4.4	3.71 $\pm$ 0.78	3.42 $\pm$ 1.34
L7	34.4 $\pm$ 5.2	3.73 $\pm$ 0.76	3.38 $\pm$ 1.28
L8	30.0 $\pm$ 4.9	3.29 $\pm$ 0.64	3.46 $\pm$ 1.33
L9	36.5 $\pm$ 6.9	3.96 $\pm$ 0.83	3.49 $\pm$ 1.40
L10	34.3 $\pm$ 7.5	3.73 $\pm$ 1.03	3.69 $\pm$ 1.48
L11	38.3 $\pm$ 15.7	5.25 $\pm$ 2.45	3.72 $\pm$ 1.44

### E.2 Regression row-attention

Regression row-attention is markedly softer and peaks earlier than in classification. Classification L9 max weight averages 0.925, while regression L9 max weight peaks at  $\approx 0.26$  and is sharpest at L6–L7 on most datasets; L9 entropy reaches  $\approx 3.8$  versus 1.756 for classification. The one-to-two-layer earlier peak tracks the probe peak shift: regression reaches usable representations earlier and pools them across more context rows.

### E.3 Regression activation patching

Activation patching restores the baseline on every regression dataset. Replacing the L9 state of blocks  $\{0, 5, 9\}$  with the cached clean activations yields  $recovery = 1.000 \pm 0.000$ , matching the classification result in §B.2.7. Table 42 gives the per-dataset baseline  $R^2$ , the two corruptions (label-shuffle, block-0 knockout) and the patched-L9 score; once the corrupted state is overwritten with the cached clean state the test-row representations become identical to baseline and the score follows.

Table 42: TabPFN-reg activation patching, per dataset (mean of 5 seeds). “LS” = label-shuffle corruption; “B0-KO” = block-0 knockout corruption. “Patched” = restored after L9 activation patching.

Dataset	Baseline $R^2$	LS corrupt	B0-KO corrupt	Patched $R^2$
Fiat-500	0.867	-0.048	0.006	0.867
Moneyball	0.947	-0.002	0.021	0.947
QSAR-fish	0.648	-0.008	-0.212	0.648
airfoil	0.964	-0.009	-0.082	0.964
cars	0.952	0.005	-0.037	0.952
concrete	0.936	-0.008	-0.200	0.936
energy	0.998	0.004	0.095	0.998
forest-fires	-0.028	-0.030	-0.044	-0.028
healthcare	0.805	-0.012	-0.116	0.805
socmob	0.796	-0.018	-0.065	0.796
mean	0.789	-0.013	-0.063	0.789

#### E.4 Per-block attention vote vs. permutation null

On every regression dataset the model learns, the L9 attention vote drives the prediction. Pearson and Spearman correlations between the model output and the attention-weighted mean of context targets are compared against a 1000-permutation null (Table 43). The vote is significant on 9/10 datasets ( $p < 10^{-3}$ , mean Pearson 0.745). The single failure, `forest-fires`, is also the dataset on which the model itself fails to learn ( $R^2 = -0.028$  in Table 42), so the vote correctly registers as uninformative.

Table 43: TabPFN-reg L9 attention-vote correlations and 1000-permutation null, per dataset (mean of 10 seeds).

Dataset	Pearson	Spearman	$z$ vs. null	$p$
Fiat-500	0.965	0.908	3.07	$< 10^{-4}$
Moneyball	0.945	0.981	2.00	0.0006
QSAR-fish	0.908	0.918	4.43	$< 10^{-4}$
airfoil	0.917	0.921	5.31	$< 10^{-4}$
cars	0.941	0.880	4.14	$< 10^{-4}$
concrete	0.892	0.926	5.36	$< 10^{-4}$
energy	0.796	0.674	3.47	$< 10^{-4}$
forest-fires	-0.577	-0.573	-1.20	0.297
healthcare	0.822	0.683	3.83	$< 10^{-4}$
socmob	0.840	0.548	2.89	0.0003

#### E.5 TabPFN falsification controls (MLP-KO and L9 uniform-attn)

Two counterfactual interventions falsify the attention-vote rule as a sole mechanism. On a mixed cls/reg panel (10 + 10 datasets, 5 seeds), Table 44 shows that both interventions degrade performance severely: MLP computation at every layer is load-bearing, and L9 attention is necessary but not sufficient.

Table 44: TabPFN falsification controls. Per-block MLP knockout zeros the MLP’s second linear at each block without retraining. L9 uniform-attn replaces the L9 softmax with  $1/N_{\text{train}}$ . Mean over 10+10 cls/reg datasets, 5 seeds each.

Intervention	Cls baseline	Cls result	Reg baseline	Reg result
MLP-KO (any block L0–L11)	0.874	0.415 ( $\Delta = -0.460$ )	0.789	-0.010 ( $\Delta = -0.798$ )
L9 uniform-attn	0.874	0.488 ( $\Delta = -0.386$ )	0.789	0.585 ( $\Delta = -0.203$ )

The smaller regression drop under uniform attention follows directly from the softer attention profile (§E.2): the L9 distribution is already close to uniform, so flattening it removes less signal.

## F TabICL regression: full results

Regression results for TabICLv2 parallel the classification analysis in §C across 10 datasets and 5 seeds, with baseline  $R^2 = 0.805$ . The structural difference from classification is the non-linear regression head at L11, which shapes both the linear-probe profile and the L11 knockout asymmetries reported below. The  $\ell_2$ - $k$ NN tracking on the final representation (§I.1) and the per-block vote refutation (§I.2) both replicate in this setting.

### F.1 Layer-by-layer summary

Per-layer linear-probe  $R^2$  (ridge, fit on the cell representation of the query rows, evaluated against the regression target) is  $\leq 0.07$  at every layer and *negative* at L9–L11, confirming the readout is non-linear at the top of the stack (Table 45). The geometric trace of the representation (Table 46) shows monotone expansion of effective rank from 19.3 at the column-embedding output to 100.0 at L11; participation ratio peaks mid-stack and 2NN-ID grows from 3.4 to 6.0.

Table 45: Per-layer linear probe  $R^2$  for TabICLv2-reg (mean±std across 10 datasets). Layer -1 is the column-embedding output; L0–L11 are the ICL blocks.

Layer	-1	0	1	2	3	4	5	6	7	8	9	10	11
$R^2$	+0.004	+0.005	+0.007	+0.004	-0.014	+0.061	+0.027	+0.046	+0.024	+0.041	-0.157	-0.463	-0.469
std	0.013	0.013	0.013	0.014	0.015	0.020	0.024	0.025	0.028	0.025	0.043	0.074	0.111

Table 46: Representation geometry per block for TabICLv2-reg (mean across 10 datasets, 5 seeds). ER = effective rank, PR = participation ratio, ID = TwoNN intrinsic dimension.

Layer	-1	0	1	2	3	4	5	6	7	8	9	10	11
ER	19.3	26.1	33.7	40.1	45.8	47.4	64.6	74.1	79.2	68.1	88.8	87.1	100.0
PR	4.4	5.7	6.9	7.0	6.8	7.9	9.7	10.0	7.4	6.8	8.0	7.1	5.6
ID	3.4	3.6	3.8	4.1	4.2	4.4	4.8	5.2	5.0	4.7	5.3	5.2	6.0

### F.2 Per-block knockout

Zeroing one ICL block at a time and re-running the regression head produces no catastrophic loss except at L11 (Table 47). Column- and row-embedding knockouts are equally tolerated (col-L0/L1/L2  $R^2$  in  $[0.71, 0.78]$ ; row-L0/L1/L2  $R^2$  in  $[0.77, 0.81]$ ). The contrast with L11 ( $R^2 = -1.16$ ) is the single distributed-vs-localized signal in this panel and matches the linear-probe drop at the top of Table 45.

Table 47: Per-block ICL knockout  $R^2$  for TabICLv2-reg (mean±std across datasets; baseline 0.805).

ICL block	0	1	2	3	4	5	6	7	8	9	10	11
$R^2$	+0.731	+0.807	+0.808	+0.805	+0.793	+0.801	+0.781	+0.711	+0.793	+0.740	+0.772	-1.156
std	0.029	0.024	0.023	0.024	0.019	0.025	0.041	0.085	0.027	0.062	0.043	0.261

### F.3 Frozen probe post-KO

Ridge probe at L11: baseline frozen  $R^2 = -0.469$  (the head is non-linear, so the linear probe is already negative at baseline). Table 48 compares the frozen probe (fit on clean activations, evaluated on KO activations) against a probe re-trained on KO activations. Large frozen-to-retrained gap at ICL-b0 and ICL-b6 indicates that the knockout disrupts the geometry the clean probe relies on, but a fresh probe can still recover most of the linearly decodable signal. ICL-b11 is a no-op for the *linear* probe at L11 because zeroing the block makes the representation pre-block, which is what the probe is fit on. Together with the  $k$ NN-vs-prototype divergence in §I.1 this confirms distributed construction + non-linear readout.

Table 48: Frozen vs. retrained ridge probe at L11 after each single-block knockout (TabICLv2-reg, 5 seeds, 10 datasets).

KO site	frozen $R^2$	retrained $R^2$
ICL-b0	-0.881	-0.006
ICL-b6	-0.692	-0.273
ICL-b11	-0.469	-0.469
ColEmb-b2	-0.610	-0.275
(no KO)	-0.469	-0.469

A complementary frozen-probe sweep (10 seeds) intervenes at three earlier sites and reads probes off multiple layers; the frozen-vs-retrained gap is uniformly large (e.g. KO@5 reads  $R^2$  frozen -0.626 vs. retrained -2.81 at L11), matching the picture above.

#### F.4 Per-block MLP knockout

Zeroing each ICL block’s MLP second linear layer (Table 49). L0–L7 lose at most 0.04 in  $R^2$ ; L8–L10 lose 0.06–0.09; L11 collapses to -0.63 ( $\Delta R^2 = -1.43$ ). Classification (§C.2.4) showed  $\leq 2.1$  pp drop at any block. The asymmetry at L11 reflects that the regression head is a full MLP rather than a linear projection.

Table 49: Per-ICL-block MLP knockout  $R^2$  for TabICLv2-reg (mean±std across datasets; baseline 0.805).

ICL block	0	1	2	3	4	5	6	7	8	9	10	11
$R^2$	+0.803	+0.808	+0.804	+0.800	+0.786	+0.797	+0.786	+0.767	+0.738	+0.740	+0.720	-0.630
std	0.025	0.025	0.026	0.022	0.020	0.019	0.024	0.030	0.079	0.074	0.092	0.177

#### F.5 Row-attention entropy

Row-attention entropy (averaged over heads, query rows, and datasets) stays flat across the ICL stack (Table 50; min 6.53 at L11, max 6.66 at L2, range  $\approx 0.13$  nats out of  $\log_e 1024 = 6.93$ ). TabPFNv2-reg, by contrast, reaches max-row-weight  $\approx 0.26$  at L9 (§E) and approaches a near-prototype readout; TabICLv2-reg never localizes onto a small context set.

Table 50: Per-layer row-attention entropy (nats) for TabICLv2-reg.

Layer	0	1	2	3	4	5	6	7	8	9	10	11
$H$	6.61	6.65	6.66	6.66	6.66	6.64	6.66	6.62	6.62	6.59	6.59	6.53

#### F.6 Label perturbations

Two label-corruption interventions (Table 51), random-shuffle and mean-replace, both drive  $R^2$  to near zero, confirming the predictions are driven by the in-context labels rather than by covariate-only structure.

Table 51: Label-perturbation  $R^2$  for TabICLv2-reg (mean±std, 10 datasets, baseline 0.805).

Intervention	$R^2$
shuffle context labels	-0.016 ± 0.019
replace with target mean	-0.010 ± 0.003

#### F.7 Uniform-attention knockout

Replacing the row-attention map at one ICL block by a uniform map (Table 52) is well tolerated for L3+ ( $R^2 \geq 0.64$ ) and breaks the model only at L0–L1 ( $R^2 = 0.03, 0.19$ ). Combined with the near-uniform entropy above, row-attention does little selective work after the first two ICL blocks.

Table 52: Per-layer uniform-attention  $R^2$  for TabICLv2-reg (mean $\pm$ std across datasets; baseline 0.805).

Layer	0	1	2	3	4	5	6	7	8	9	10	11
$R^2$	+0.029	+0.187	+0.554	+0.713	+0.765	+0.733	+0.776	+0.641	+0.797	+0.686	+0.795	+0.801
std	0.664	0.577	0.238	0.113	0.059	0.076	0.056	0.172	0.025	0.040	0.034	0.028

## F.8 Per-block vote refutation

Following the classification protocol (§1.2) we read off a prototype-style prediction from each ICL block and correlate it with TabICLv2’s own prediction and with the ground-truth target; see Table 53. No early or middle block matches the model’s predictions; the highest agreement is at L9 (Pearson 0.73 with the model, 0.65 with truth) and L11 (0.67/0.64). The pattern — correlations only emerging at the last few blocks — is the regression analogue of the classification vote refutation.

Table 53: Per-block prototype-vote correlations for TabICLv2-reg. Pearson coefficient between block- $k$  vote prediction and either the model’s own prediction (pred) or the ground truth (truth).

Block	0	1	2	3	4	5	6	7	8	9	10	11
pred	-0.22	+0.40	+0.44	+0.27	-0.52	-0.28	-0.23	-0.43	+0.64	+0.73	+0.08	+0.67
truth	-0.20	+0.38	+0.38	+0.21	-0.49	-0.24	-0.22	-0.39	+0.56	+0.65	+0.04	+0.64

## G Permutation invariance: full results

### G.1 Architectural sources of permutation sensitivity

Table 54: Component-level sources of permutation sensitivity. A  $\checkmark$  indicates the component is present and order-sensitive.

Model	in_linear	Grouping	RoPE	pos_emb ( $W, b$ )
TabICLv1	$\checkmark$	none	$\checkmark$	—
TabICLv1.1	$\checkmark$	none	$\checkmark$	—
TabICLv2	$\checkmark$	circular	$\checkmark$	—
TabPFN	—	features_per_group=2	—	$\checkmark$
Mitra	shared cell	none	—	—

Table 54 catalogues the positional-encoding components that break permutation invariance. TabPFNV2’s positional embedding maps each feature index  $p$  through a learned  $W \in \mathbb{R}^{192 \times 48}$  and adds a learned bias  $b \in \mathbb{R}^{192}$ ; preprocessing (standardisation, outlier clipping, quantile transforms) also runs in feature order. TabICLv1 and v2 both apply RoPE along the feature dimension, and v2 additionally enforces circular feature grouping; neither version encodes row position. Row invariance is hard-coded; column invariance is broken by  $W, b$  in TabPFNV2 and by RoPE in TabICLv1 and v2; label invariance is broken by the learned label embeddings throughout.

### G.2 Synthetic invariance verifications

**Protocol.** The grid spans 3 seeds, 3 dataset sizes, and 3 configurations, with predictions counted as agreeing when they differ by at most 0.005. TabICLv1 contributes baseline and no-RoPE configurations; TabICLv2 contributes baseline, no-RoPE, and no-RoPE under an arbitrary-permutation control. TabPFNV2 contributes baseline, no positional embedding ( $W=0, b$  retained), and the latter under an arbitrary-permutation control.

Three residual symmetries surface within tolerance. TabPFNV2 with  $W = 0$  exhibits *group-permutation invariance*: pairs of features reorder freely, but pairs themselves do not split across groups. TabICLv2 with RoPE removed exhibits *circular-shift invariance*. TabICLv1 with RoPE removed exhibits *arbitrary-column invariance*. These outcomes match the architecture mapping in Table 22: removing one route exposes the residual symmetry of the route that remains — TabPFNV2’s within-pair symmetry of feature grouping (M3, pair size 2), TabICLv2’s cyclic symmetry of circular

grouping, and, with no M3 route in TabICLv1, arbitrary-column invariance at the cost quantified in §G.4.

Table 55: Synthetic invariance verifications: passes / 9.

Model variant	Test	det	row	col	label
TabPFN baseline / $W=0$	arb	9/9	9/9	0/9	4/9
TabPFN baseline / $W=0$	grp2	9/9	9/9	6/9	2/9
TabICLv1	arb	9/9	9/9	0/9	1/9
TabICLv1 no-RoPE	arb	9/9	9/9	<b>9/9</b>	0/9
TabICLv2 (& no-RoPE)	arb/grp3	9/9	9/9	0/9	0/9

### G.3 Real-data invariance: TabPFN

Four configurations on 49 datasets, 5 seeds, 3 column-permutation trials: *Baseline* (standard TabPFNV2 [Hollmann et al., 2025]);  $W=0$  (positional weight matrix zeroed, bias  $b$  retained); *sign( $b$ )* ( $W=0$ , bias replaced by  $\text{sign}(b)$ ); *no\_pe* ( $W=0$ ,  $b=0$ , all positional parameters removed).

Setting  $W=0$  shifts predictions by at most 0.001 and preserves accuracy (0.854→0.854); replacing  $b$  with  $\text{sign}(b)$  is also lossless (0.855); removing  $b$  collapses accuracy to 0.338, proving  $b$  acts as an architectural prior, not a positional code.

Table 56: TabPFN per-dataset behavior: 5 datasets with the lowest column-label-agreement; accuracy is unchanged under  $W=0$  (mean acc 0.853 baseline vs. 0.853 at  $W=0$ ,  $n=45$ ).

Dataset	Col. agree	Acc. baseline	Acc. $W=0$
analcata_data_dmft	78.0%	0.216	0.216
cylinder-bands	90.4%	0.726	0.726
steel-plates-fault	92.7%	0.794	0.793
mfeat-zernike	92.7%	0.839	0.838
vehicle	92.7%	0.851	0.851

### G.4 Real-data invariance: TabICLv1 and v2

Each version is run in two configurations on 49 datasets, 5 seeds, and 3 trials: baseline and no-RoPE. TabICLv2 carries both the M2 and M3 routes and tolerates RoPE removal; TabICLv1 carries only M2 and relies on RoPE to escape the multiset bound. The  $\approx 15$  pp gap upper-bounds what RoPE buys as the sole symmetry-breaker.

Table 57: Per-dataset accuracy when RoPE is removed,  $n=49$ : 5 datasets where v1 loses the most.

Dataset	TabICLv1			TabICLv2		
	base	no-RoPE	$\Delta$ pp	base	no-RoPE	$\Delta$ pp
mfeat-karhunen	0.968	0.387	-58.1	0.980	0.979	-0.1
mfeat-pixel	0.931	0.392	-54.0	0.975	0.975	0.0
semeion	0.858	0.328	-53.0	0.956	0.952	-0.4
MiceProtein	0.998	0.503	-49.5	1.000	1.000	0.0
balance-scale	0.987	0.493	-49.4	0.990	0.990	0.0
<b>Mean (all 49)</b>	0.851	0.697	<b>-15.4</b>	0.864	0.862	<b>-0.1</b>
<b># losing &gt; 5 pp</b>		27/49			0/49	

## G.5 Real-data invariance summary

Table 58: Permutation agreement rates and accuracy (49 datasets  $\times$  5 seeds  $\times$  3 trials). Column agreement below 100% reflects order-sensitive preprocessing and grouping; label agreement reflects class-ordering sensitivity.

Model	Accuracy	Row agree.	Col. agree.	Label agree.
TabPFN	0.854	100.0%	98.2%	96.7%
TabICL v2	0.865	100.0%	98.2%	97.7%

## G.6 One-vs-All label invariance

Wrapping each model in a One-vs-All classifier achieves 100% label-order agreement at zero accuracy cost.

Table 59: One-vs-All wrapper,  $n=21$  multi-class datasets.

Model+OvA	Acc.	Col. agree	Label agree
TabPFN+OvA	0.877	98.4%	100% (21/21)
TabICL v1+OvA	0.880	97.2%	100% (21/21)
TabICL v2+OvA	0.890	98.3%	100% (21/21)

Mitra is column-invariant by architecture but not class-invariant in its shipped form (§D.1). Wrapping it in OvA recovers full class invariance at no accuracy cost on the same multi-class real subset (extended to  $n=24$  here for completeness; 5 seeds, 3 trials, identical split protocol): Mitra v1 baseline 0.841, Mitra v1+OvA 0.841, column agreement 99.9%, label agreement effectively at 100%.

## G.7 Best/worst permutation spread

For each dataset we record the best and worst accuracy across the  $5 \times 3 = 15$  column-permutation trials. Column-permutation spread reaches  $\sim 8.0$  pp on the worst real dataset (cylinder-bands; Figure 5); the median is an order of magnitude smaller (Table 60).

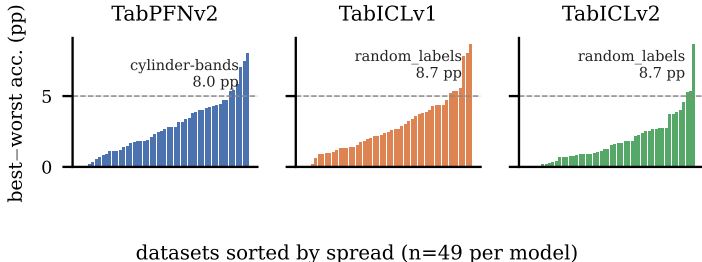


Figure 5: Per-dataset accuracy spread under random column permutations on the 49-dataset benchmark. For each dataset, the bar is (best accuracy across permutations)–(worst), measuring sensitivity to the semantically irrelevant ordering of input features. Datasets are sorted ascending within each model. Most sit below the 5 pp dashed line, but a tail reaches  $\sim 8.7$  pp (worst dataset annotated). *Takeaway:* the mechanism-aware remedies of §4.1 address this deployment-relevant tail risk at no accuracy cost.

Table 60: Best–worst accuracy spread (pp) per model ( $n=45$ ). Six TabPFN/v1 datasets exceed the 5 pp threshold; only two for v2.

Model	median	mean	Q1	Q3	max	Worst 3 datasets (spread pp)
TabPFN	2.67	2.91	1.39	4.14	8.02	cylinder-bands 8.02, tic-tac-toe 7.47, dresses-sales 7.00
TabICL v1	2.38	2.74	1.31	4.06	8.00	dresses-sales 8.00, hill-valley 7.82, cylinder-bands 5.56
TabICL v2	1.54	1.73	0.75	2.57	5.33	dresses-sales 5.33, cylinder-bands 5.25, ilpd 4.56

## G.8 Spectrum of invariance types

Table 61: Spectrum of achievable permutation invariance types, the scope of columns covered, and the accuracy cost of achieving it. Costs are mean differences over 49 datasets  $\times$  5 seeds  $\times$  3 trials relative to the respective baseline.

Model	Invariance type	Scope	Accuracy cost
TabICL v1 (no RoPE)	Arbitrary column permutations	All columns	−15.4 pp
TabICL v2 (no RoPE)	Circular column shifts	All columns	−0.2 pp
TabPFN ( $W = 0$ )	Group permutations (groups of 2 features)	Within groups	0 pp

Table 61 catalogues the achievable invariance types and their costs. Arbitrary-permutation invariance is reachable only in TabICLv1, and only at −15.4 pp. Narrower types — circular shifts for TabICLv2 and group permutations for TabPFNV2 — carry no measurable accuracy cost.

## G.9 Pretraining an invariant TabICLv1 from scratch

**Setup.** We retrain TabICLv1 under the original stage-1 protocol of Qu et al. [2025]: 100k optimization steps at batch size 512, identical synthetic prior, no stage-2 finetuning. Two architectural switches are toggled independently, yielding four pretrained checkpoints:

- *RoPE* on/off along the feature axis. “On” is the released TabICLv1 configuration; “off” removes the rotary positional embedding entirely (not zeroed at inference, but absent during pretraining).
- *Class head*: standard class-conditional head (“no”, released configuration) versus a class-invariant head (“yes”), in which context labels enter as one-hot columns and a shared decoder emits one logit per class. Permuting the class index permutes both the conditioning columns and the output channels identically, so the `argmax` prediction is exactly class-permutation invariant by construction.

Evaluation follows the OpenML protocol of [Qu et al., 2025]. Headline numbers reproduced in Table 2.

**Reading.** Both invariance levers are essentially free in isolation but compound to a −2.6 pp gap when combined. This matches the mechanism identified in §5: RoPE is TabICLv1’s only within-row symmetry-breaker (one of the “M2-only” models in §5.1), so removing it during pretraining without an architectural substitute is the harder of the two ablations. The class-invariant head adds an output-axis constraint that is, on its own, well-absorbed by training. Mitra’s shared cell embedding (§D.1) shows that a column-invariant tabular foundation model *can* be trained at competitive accuracy when the architecture itself supplies the symmetry from the start, rather than relying on training to absorb its removal.

## H Mechanism-grounded attacks: full results

This appendix reports the full results behind §6. Each attack tests a specific mechanistic prediction: neighbourhood pollution targets the local label aggregation shared by the two readouts (§3.1, §3.3); geometry corruption targets the learned similarity of §1.9 and the input geometry feeding TabICLv2’s prototypes; null-space PGD targets non-linear feature directions a linear baseline cannot access; SVD-hiding tests whether TabPFNV2’s preprocessing pipeline and TabICLv2’s distributed representation

can be exploited by relocating signal into discarded components. Mechanism transplantation (§3.4) is reported in §I.3.

## H.1 Attack definitions and protocols

All attacks operate on the in-context window: they perturb the context set seen at inference time and measure the resulting drop in classification accuracy. Nine individual attacks are evaluated, organized into four families.

**noise\_pad.** Extra noisy context rows added (50% padding); each padded row is sampled from the per-feature empirical distribution. Floor on robustness against context-set dilution.

**hub\_poison.** Context examples (“hubs”) with the smallest average  $k$ -NN distance to all other context points have their labels flipped. Hubs occupy dense, class-ambiguous regions and disproportionately contaminate nearest-neighbour readouts.

**centroid\_inj.** A synthetic example injected at the class centroid of a target class with the wrong label, pulling the effective centroid toward a competitor.

**boundary\_poison.** Context examples within a margin of the decision boundary (estimated via a held-out probe) have their labels flipped.

**mono\_cube, mono\_softexp, mono\_rank.** Three monotone-function attacks that transform individual features while preserving their rank order. MONO\_CUBE applies a signed cube-root transform; MONO\_SOFTEXP applies a soft-exponential; MONO\_RANK replaces values with their within-column rank. All three break linear separability while leaving ordinal structure intact.

**svd\_hide.** Signal injected along the smallest-singular-value SVD direction of the context feature matrix into test queries but not context, creating a query–context discrepancy invisible to any decoder attending only to context features. Details in §H.10.

**Null-space PGD.** PGD that moves context examples along the null space of the Ridge regression weight matrix, so the perturbation is invisible to Ridge while still shifting the geometry seen by TabPFN. Details in §H.9.

Hyperparameters (noise scale, hub count, margin, PGD step size and budget) were fixed before any model evaluation. Each experiment reports mean accuracy over the relevant dataset  $\times$  seed grid; gaps ( $\Delta$ ) are signed differences (model minus baseline) and 95% paired-bootstrap confidence intervals are computed over the dataset dimension.

## H.2 TabPFN vs. Ridge, full table

Table 62: TabPFN vs. Ridge under five mechanism-grounded attacks.  $\Delta$  columns report mean accuracy change (post-attack – clean) on each attack’s evaluation grid. The differential (last column) is  $\Delta_{\text{TabPFN}} - \Delta_{\text{Ridge}}$ ; negative values mean TabPFN is *more* damaged. Sample sizes vary because some attacks have explicit exclusion criteria (see §H.1, §H.9).

Attack	$\Delta_{\text{TabPFN}}$	$\Delta_{\text{Ridge}}$	Differential
noise_pad (4 $\times$ padding, $n=49$ )	−0.076	−0.041	−0.035
hub_poison (top 15% $k$ -NN hubs, $n=49$ )	−0.029	−0.014	−0.015
mono_rank (rank transform, $n=49$ )	−0.084	−0.043	−0.041
svd_hide (real-data rotation, $n=40$ )	−0.018	−0.000	−0.018
null-space PGD (§H.9, $n=29$ )	−0.047	0.000	−0.047

The null-space attack is constructed in the null space of  $W_{\text{ridge}}$ , so by design Ridge accuracy is unaffected; TabPFNV2 drops because it attends to feature directions Ridge ignores.

### H.3 TabPFN vs. XGBoost, full table

Table 63: TabPFN vs. XGBoost under nine conditions (49 cls  $\times$  10 seeds; MONO\_SOFTEXP  $n=48$  after one numerically degenerate dataset is dropped). Means are averages of per-dataset seed means.  $\Delta = \text{TabPFN} - \text{XGB}$  with 95% bootstrap CI over per-dataset paired differences. TabPFN dominates on every attack ( $\Delta > 0$ ), with the smallest gap on MONO\_SOFTEXP (+0.014) and the largest on HUB\_POISON (+0.046).

Condition	TabPFN	XGBoost	$\Delta$	95% CI
baseline (clean)	0.854	0.828	+0.026	[+0.010, +0.047]
noise_pad	0.845	0.821	+0.024	[+0.009, +0.045]
hub_poison	0.828	0.782	+0.046	[+0.030, +0.066]
centroid_inj	0.855	0.827	+0.029	[+0.015, +0.048]
boundary_poison	0.843	0.819	+0.024	[+0.009, +0.044]
mono_cube	0.848	0.828	+0.020	[+0.003, +0.041]
mono_softexp	0.810	0.796	+0.014	[+0.002, +0.025]
mono_rank	0.756	0.737	+0.020	[-0.014, +0.051]
svd_hide	0.796	0.758	+0.039	[+0.024, +0.055]

XGBoost is a non-linear, tree-structured baseline; the differential absorbs the part of vulnerability shared by any flexible classifier.

### H.4 TabICL vs. XGBoost, full table

Table 64: TabICL vs. XGBoost under all eight attacks (24 classification datasets  $\times$  5 seeds).  $\Delta = \text{TabICL} - \text{XGB}$  with 95% bootstrap CI over per-dataset paired differences. TabICL is at least as accurate as XGBoost on every attack except MONO\_RANK (CI covers zero); the largest gap is on SVD\_HIDE.

Attack	XGBoost	TabICL	$\Delta$	95% CI
baseline (clean)	0.862	0.888	+0.026	[+0.001, +0.048]
noise_pad	0.847	0.882	+0.035	[+0.018, +0.054]
hub_poison	0.814	0.855	+0.041	[+0.014, +0.064]
centroid_inj	0.858	0.885	+0.027	[+0.007, +0.046]
boundary_poison	0.840	0.877	+0.037	[+0.024, +0.052]
mono_cube	0.862	0.886	+0.023	[+0.004, +0.045]
mono_softexp	0.846	0.865	+0.019	[+0.001, +0.040]
mono_rank	0.787	0.787	+0.000	[-0.062, +0.042]
svd_hide	0.752	0.838	+0.086	[+0.051, +0.128]

The largest gap is on SVD\_HIDE ( $\Delta = +0.086$ ): XGBoost collapses because its gradient-based training is sensitive to the injected SVD direction while TabICL’s L11 prototype readout is partially shielded by its distributed, attention-averaged encoding.

### H.5 Tuned MLP baseline on the same attack grid

A two-hidden-layer ReLU MLP with dropout 0.1 and AdamW ( $\text{lr}=10^{-3}$ , weight decay  $10^{-4}$ ) is trained per (dataset, seed) on the same context set as the foundation models, with identical ordinal categorical encoding and no further preprocessing. For each cell the hidden width is selected from (128, 64), (256, 128), (512, 256) by held-out validation accuracy on a 20% split of the context set with early stopping (patience 20, max 200 epochs); the chosen configuration is then re-applied unchanged to every attack variant of that cell. The MLP baseline supplies the non-linear neural control that separates mechanism-specific from generic non-linear-classifier vulnerability on the same 24-classification grid.

Table 65: Per-attack signed accuracy drop  $\Delta$  pp on the common 24-classification  $\times 5$ -seed grid for both foundation models, a tuned XGBoost, and a tuned MLP (2 hidden layers selected per (dataset, seed) from (128, 64), (256, 128), (512, 256) by validation accuracy; AdamW with early stopping; identical ordinal categorical encoding). 95% bootstrap CI over per-dataset seed means in brackets; \* denotes Holm-corrected significance at  $\alpha=0.05$  across the eight attacks per model. Clean baselines: TabPFNv2 88.2%, TabICLv2 88.8%, XGBoost 86.3%, MLP 85.0%.

Attack	TabPFNv2	TabICLv2	XGBoost	MLP
noise_pad	-1.5* [-2.4, -0.6]	-0.6 [-1.5, +0.5]	-1.6 [-3.4, -0.1]	-2.7* [-3.9, -1.7]
hub_poison	-3.9* [-5.7, -2.2]	-3.3* [-4.8, -1.9]	-4.8* [-6.1, -3.4]	-2.8* [-4.0, -1.6]
centroid_inj	-0.1 [-0.7, +0.6]	-0.3 [-1.1, +0.5]	-0.4 [-0.9, +0.1]	-0.7 [-1.5, +0.2]
boundary_poison	-1.9* [-2.9, -1.1]	-1.2 [-2.2, -0.0]	-2.3* [-3.9, -0.9]	-2.9* [-4.2, -1.7]
mono_cube	-1.1 [-2.4, +0.1]	-0.3 [-1.5, +1.1]	0.0 [0.0, 0.0]	-4.8* [-8.7, -1.7]
mono_softexp	-2.2* [-3.7, -0.8]	-2.3* [-3.8, -0.8]	-1.7 [-3.2, -0.3]	-4.1* [-5.9, -2.3]
mono_rank	-8.0* [-15.0, -2.4]	-10.1* [-18.7, -3.5]	-7.6* [-14.1, -2.5]	-4.3* [-8.4, -1.1]
svd_hide	-8.3* [-13.6, -3.7]	-5.0* [-8.8, -2.1]	-11.1* [-16.3, -6.3]	-10.2* [-17.6, -4.7]

The MLP attains a clean 85.0% mean accuracy, lower than either foundation model (88.2%, 88.8%) but comparable to XGBoost (86.3%). The relative attack drops sort the attacks into three groups. (i) *Mechanism-targeted*: MONO\_RANK drops the foundation models by 8–10 pp while the MLP loses only 4.3 pp, and HUB\_POISON drops the foundation models by 3.3–3.9 pp while the MLP loses 2.8 pp; both confirm the predictions (§6) that distance-based retrieval readouts are uniquely sensitive to inter-value-distance erasure and that vote-style readouts are uniquely sensitive to flips of high-degree context points. (ii) *Shared with any flexible classifier*: BOUNDARY\_POISON, NOISE\_PAD, CENTROID\_INJ and SVD\_HIDE hurt the MLP at least as much as the foundation models, so the headline drops on these attacks reflect sensitivity shared by any flexible classifier rather than a readout-specific weakness. (iii) *Absorbed by the ICL prior*: MONO\_CUBE and MONO\_SOFTEXP hurt the MLP roughly twice as much as the foundation models, consistent with the foundation models’ Bayesian/ICL-style averaging absorbing smooth feature warps that a freshly fitted MLP cannot. The Holm-corrected significance pattern is preserved on both foundation models when the six `mfeat-*` datasets are removed; SVD\_HIDE drops shrink (TabPFNv2  $-8.3 \rightarrow -3.5$  pp; MLP  $-10.2 \rightarrow -5.0$  pp; TabICLv2  $-5.0 \rightarrow -3.0$  pp), reflecting the digit-family’s particular sensitivity to the SVD construction.

## H.6 Multiplicity controls and baseline summary

**Holm correction.** Within each model the eight perturbations of Table 3 are corrected at  $\alpha=0.05$  via Holm’s step-down procedure. The corrected significance pattern keeps the rank/hub/SVD trio significant on TabPFNv2 and TabICLv2 and the hub/soft-exp/SVD trio significant on Mitra; diffuse perturbations (centroid injection, cube warp) are not significant for any model, and noise padding is significant only on TabPFNv2. The pattern is preserved for TabPFNv2 and TabICLv2 when the six `mfeat-*` datasets are removed, with reduced SVD\_HIDE drops as documented in §H.5.

**Wilcoxon signed-rank.** A pre-specified one-sided Wilcoxon signed-rank test on the per-dataset paired difference between (rank warp, hub poison) and (cube warp, centroid injection) rejects at  $p < 10^{-3}$  on TabPFNv2 and TabICLv2; on Mitra only the hub component contributes ( $p < 10^{-3}$  on (hub, SVD) vs. (cube, centroid)).

**Baseline summary.** On the 24-grid TabPFNv2 and TabICLv2 remain at least as accurate as a tuned XGBoost after every perturbation except SVD burial, where XGBoost itself loses  $-11.1$  pp. On the 16-dataset mixed-type slice (§H.8, §H.7), native-categorical CatBoost reaches 76.7% and XGBoost 77.3%; TabPFNv2 ties and TabICLv2 stays ahead at 78.9%. A tuned MLP refit on the same poisoned context attains a clean 85.0% (§H.5); the rank-warp and hub-poisoning gaps are the diagnostic ones—the MLP loses 4.3 pp under rank warp while TabPFNv2/TabICLv2 lose 8–10 pp, and the MLP loses 2.8 pp under hub poisoning while TabPFNv2/TabICLv2 lose 3.3–3.9 pp, confirming the mechanistic prediction that distance-based vote and prototype readouts are uniquely sensitive to inter-value-distance erasure and high-degree label flips. The null-space PGD diagnostic (§H.9) leaves Ridge unchanged by construction but still costs TabPFNv2  $-4.7$  pp, ruling out any single linear readout in the Ridge feature basis.

## H.7 Native-categorical CatBoost clean control

XGBoost’s ordinal handling of categorical columns may understate a modern tree baseline on this grid. We rerun the clean 24-dataset classification grid with CatBoost using native categorical handling wherever the OpenML metadata marks categorical columns, the same 80/20 split as the main experiments, and a small validation-tuned GPU grid over depth  $\{4, 6\}$ , learning rate  $\{0.03, 0.10\}$ , and iterations  $\{500, 1000\}$  with early stopping. We do not rerun the attack perturbations with CatBoost: several attack operators are defined only on the shared ordinal-encoded numeric representation, so this control is clean-only.

Table 66: Clean-only comparator means on the same 24-dataset attack grid. The mixed-type subset contains the four datasets with at least one categorical column (car, cylinder-bands, dresses-sales, eucalyptus).

Model	24-grid clean mean	mixed-type subset mean
TabPFN	0.882	0.778
TabICL	0.888	0.819
XGBoost	0.863	0.770
CatBoost	0.860	0.752
MLP	0.850	0.749

Only four of the 24 datasets on this grid contain categorical features, so the native-categorical advantage is a narrow probe. On this suite CatBoost lands close to tuned XGBoost overall and does not overtake either foundation model on the mixed-type subset; the clean-baseline ordering holds. The 16-dataset slice below extends this evidence to a broader mixed-type benchmark.

The four-dataset mixed-type subset is narrow. We rerun the same native-categorical CatBoost protocol on every classification dataset in the 49-dataset benchmark whose OpenML metadata marks at least one categorical column, and add a matching native-categorical XGBoost control on the same fixed slice. This mixed-type slice contains the 16 datasets enumerated in §A.4. The clean ordering holds (Tab. 67): TabICLv2 stays ahead of CatBoost on 14/16 datasets (one tie), with a mean paired advantage of +2.3 pp and 95% CI  $[-1.1, +3.5]$ ; TabPFNV2 lands closer (+0.8 pp, CI  $[-0.2, +1.6]$ ) and loses on 5/16. Native-categorical XGBoost falls between the two tree baselines at 77.3% mean accuracy: TabPFNV2 ties overall (+0.2 pp, CI  $[-1.7, +1.8]$ ), and TabICLv2 leads by +1.7 pp (CI  $[-0.5, +2.9]$ ). This extends the mixed-type clean-baseline evidence well beyond the four-dataset probe; attack-time mixed-type behavior is addressed in §H.8.

Table 67: Broader native-categorical tree controls on the 16 classification datasets in the 49-dataset benchmark with at least one categorical column (5 seeds / dataset). TabPFN and TabICL means use the same 80/20 split as the 49-dataset readout-grid evaluations.  $\Delta$  = model – CatBoost with 95% bootstrap CI over per-dataset paired differences.

Model	mixed-type clean mean	$\Delta$ vs. CatBoost [95% CI]
TabPFN	0.774	+0.008 $[-0.002, +0.016]$
TabICL	0.789	+0.023 $[+0.011, +0.035]$
XGBoost (native-categorical)	0.773	+0.006 $[-0.010, +0.023]$
CatBoost	0.767	—

## H.8 Broader mixed-type attack slice

The clean-only controls above establish baseline breadth; attack-time mixed-type behavior is the next question. We rerun the three highest-signal attacks from the main text—hub poison, rank warp, and SVD burial—on the full 16-dataset mixed-type slice under the same shared ordinal-encoded numeric view used by the foundation models (5 seeds / dataset). The attack-pipeline clean means on this slice are 0.781 for TabPFNV2 and 0.791 for TabICLv2. The same ordering survives (Tab. 68): hub poison costs 2–3 pp, rank warp dominates for both models, and SVD burial is small on average. Rank- and hub-style attacks remain the strongest within-design predictor of where the foundation models lose ground, including on mixed-type data.

Table 68: Broader mixed-type attack slice on the 16 mixed-type classification datasets under the shared ordinalised numeric view (5 seeds / dataset).  $\Delta$  is the within-model pp change from the clean mixed16 attack-pipeline baseline.

Attack	TabPFNv2 $\Delta$ pp [95% CI]	TabICLv2 $\Delta$ pp [95% CI]
hub poison	-2.4 [-3.7, -1.4]	-2.8 [-4.1, -1.5]
rank warp	-17.2 [-28.9, -7.1]	-21.0 [-34.5, -10.2]
SVD burial	-0.2 [-0.7, +0.5]	-1.0 [-2.2, -0.1]

## H.9 Null-space PGD details

The null space of the Ridge weight matrix  $N(W_{\text{ridge}})$  is computed via a thin SVD of  $W_{\text{ridge}}^\top$ ; columns of  $V$  with singular values below  $10^{-6} \cdot \sigma_{\text{max}}$  span the near-null space.

**Dataset exclusion.** Three datasets excluded for zero null-space dimension. A further 17 excluded as numerically degenerate (fewer than five directions pass the threshold).

**PGD hyperparameters.**  $\eta = 0.01$  (in unit-variance feature units),  $T = 200$  steps,  $\ell_2$  budget  $\varepsilon = 1.0$ . After each step, the perturbation is projected onto the null space (so Ridge sees no change) and clipped to the  $\ell_2$  ball. Untargeted: maximize the cross-entropy of the Ridge prediction distribution under TabPFN, using Ridge’s soft output as a fixed proxy.

## H.10 SVD-hiding details and per-dataset breakdown

**Mechanism.** Let  $[X_{\text{ctx}}; X_{\text{query}}] \in \mathbb{R}^{(n+m) \times d}$  be the stacked context-and-query feature matrix. A thin SVD yields singular values  $\sigma_1 \geq \dots \geq \sigma_d$ . We divide the top  $k = \lceil d/4 \rceil$  singular values by 10 and multiply the remaining  $d - k$  by 10, then reconstruct and split back into context and query. This dampens the high-variance components that similarity-and-vote and prototype readouts rely on and amplifies the low-variance components most decoders ignore, hitting context and query consistently.

**Three-copy preprocessing redundancy.** TabPFN’s three-copy preprocessing (original, rank-normalized, quantile-normalized features) re-bases the geometry across copies; the high-variance components in raw feature space are not the high-variance components in the encoder’s input space, so the reweighting produces only partial perturbation of TabPFN’s actual input.

**Real vs. synthetic comparison.** On real datasets, the svd\_hide gap between TabICL and XGBoost ( $\Delta = +0.086$ , §H.4) is substantially larger than on synthetic datasets where the low-variance direction is by construction uninformative. The attack exploits genuine low-variance signal that XGBoost uses (via split-based selection) but TabICL’s L11 prototype readout discards.

**Per-dataset breakdown.** On 34/49 datasets XGBoost is more damaged than TabPFN (mean drops  $-0.058$  vs.  $-0.070$ , differential  $+0.013$ ). On hill-valley TabPFN scores 0.593 on raw features but  $\{0.934, 0.926, 0.918, 0.914\}$  when projected to top- $\{10, 20, 50, 100\}$  PCs (SVD-projected variant of hill-valley).

Table 69: SVD\_HIDE: five datasets with the largest XGBoost drop.

Dataset	TabPFN clean	TabPFN svd	$\Delta_{\text{TabPFN}}$	XGBoost clean	XGBoost svd	$\Delta_{\text{XGBoost}}$
mfeat-karhunen	0.963	0.613	-0.350	0.925	0.508	-0.418
mfeat-pixel	0.960	0.540	-0.420	0.948	0.603	-0.345
mfeat-fourier	0.895	0.585	-0.310	0.860	0.557	-0.302
semeion	0.918	0.718	-0.201	0.897	0.611	-0.285
sign_1d	0.980	0.840	-0.140	1.000	0.720	-0.280

### H.11 Side-by-side TabPFN/TabICL contrast table

Table 70: Mechanistic comparison of TabPFN [Hollmann et al., 2025] and TabICL [Qu et al., 2025] across five dimensions.

Dimension	TabPFN	TabICL
Critical early block	Block-0: encodes formats & shapes (§2.3)	ColEmb-2: SetTransformer readout
Attention role	Sharp & locally necessary at L9 (§B.2.5)	Individually redundant; jointly necessary (§C.2.3)
Similarity tracking	$r = 0.34$ (attn. vs. query–context sim.; §1.9)	$r < 0.08$ at every block (§C.3.4)
Rank profile	Early bottleneck (§2.2)	Late prototype-formation phase (§2.2)
Operational readout	Attention-weighted label vote (§3.1)	Nearest-class prototype over L11 reps. (§3.3)

Table 70 summarizes the five mechanistic dimensions that distinguish the two architectures (referenced from §3.4).

## I Additional experiments

All experiments in this appendix are inference-only on the same model releases as the rest of the paper; none require pretraining (§7). Statistical reporting follows §A.5.

### I.1 TabICL-reg L11 kNN

Regression analogue of §C.3.5: 10 reg datasets  $\times$  5 seeds, four distance spaces, four neighbour counts. Each cell reports the across-dataset mean of (Pearson  $r$  between kNN-imputed and TabICL-reg prediction / kNN  $R^2$  against the ground truth).

Table 71: TabICL-reg kNN agreement / kNN  $R^2$  aggregated over 10 regression datasets, 5 seeds. Rep- $\ell_2$  at L11 dominates input- $\ell_2$  at every  $k$ ; the kNN-in-final-rep finding holds for regression as for classification.

$k$	input- $\ell_2$	rep- $\ell_2$ (L11)	rep-cosine (L11)	rep-Mahalanobis (L11)
$k=1$	0.603 / -0.375	0.784 / 0.542	0.719 / 0.459	0.207 / -0.218
$k=3$	0.665 / 0.286	0.842 / 0.575	0.781 / 0.504	0.324 / 0.017
$k=5$	0.681 / 0.386	<b>0.859 / 0.577</b>	0.801 / 0.515	0.360 / 0.044
$k=10$	0.689 / 0.433	0.871 / 0.566	0.830 / 0.519	0.382 / 0.036

### I.2 TabICL-reg per-block vote refutation

Regression analogue of §C.3.6: per-block pseudo-vote  $\hat{y}_L = \sum_i \alpha_i y_i$  from head-mean test  $\rightarrow$  train attention. 10 reg datasets  $\times$  5 seeds.

Table 72: TabICL-reg per-block weighted-label vote, mean across 10 datasets. Pearson is correlation between  $\hat{y}_L$  and the model’s own prediction (or ground truth). Best layer L9 ( $r = 0.732$ ) is far below the TabPFN-reg ceiling  $r \geq 0.896$ ; six of twelve layers are negative. Weighted-label vote is not the dominant TabICL-reg mechanism.

Layer	Pearson(pred)	Pearson(truth)	vote $R^2$	Layer	Pearson(pred)	Pearson(truth)	vote $R^2$
L0	-0.222	-0.199	-0.038	L6	-0.231	-0.221	-0.019
L1	+0.396	+0.384	+0.006	L7	-0.429	-0.391	-0.033
L2	+0.442	+0.380	+0.001	L8	+0.642	+0.557	+0.032
L3	+0.265	+0.213	-0.006	L9	<b>+0.732</b>	+0.647	+0.064
L4	-0.523	-0.485	-0.029	L10	+0.076	+0.040	-0.008
L5	-0.276	-0.243	-0.027	L11	+0.672	+0.643	+0.088

### I.3 Mechanism transplantation

Direct causal test of §3.4, 49 cls  $\times$  5 seeds. Each row is a per-dataset paired comparison; we report the across-dataset means and a bootstrap 95 % CI over per-dataset paired differences ( $10^4$  resamples) on  $\Delta$ . Rows (iii) and (vi) add a minimal host-side control: logistic regression on the frozen host representation.

#### Four conditions.

- (i) TabPFN native vote (L9).
- (ii) TabPFN with prototype readout:  $\hat{p}(c) \propto \exp(-\|h_{L11} - \mu_c\|_2^2)$ ,  $\mu_c$  unweighted per-class means of L11 representations of all training rows.
- (iii) TabICL native prototype (L11).
- (iv) TabICL with vote readout: at the sharpest-attention block  $b^*(D)$  selected per dataset  $D$ ,  $\hat{p}(c) = \frac{1}{H} \sum_h \sum_i \alpha_h^{(i)} \mathbf{1}[y_i = c]$ .

Table 73: Bootstrap CIs for the cross-transplant and fitted-host linear-head conditions of Table 1 (49 cls  $\times$  5 seeds). CI: 95% paired-bootstrap over datasets. Naive cross-transfer is catastrophic on both sides, but the fitted-host recovery is asymmetric: TabPFNV2 remains far below native, whereas TabICLv2 nearly recovers.

Condition	Description	Accuracy	vs. native $\Delta$ (95% CI)
(i)	TabPFN native	0.854	—
(ii)	TabPFN + prototype	0.523	-0.331 [-0.412, -0.253]
(iii)	TabPFN + linear head	0.617	-0.237 [-0.305, -0.172]
(iv)	TabICL native	0.864	—
(v)	TabICL + vote	0.470	-0.395 [-0.484, -0.307]
(vi)	TabICL + linear head	0.859	-0.005 [-0.009, -0.001]

The naive cross-transplants are catastrophic and the CIs do not cover zero (Table 73). The fitted-host control is asymmetric: TabPFN remains far below native while TabICL nearly recovers (within 1 pp on 32/49 datasets), so the stronger non-portability claim is asymmetric.

**Per-dataset breakdown.** Both readouts collapse on multi-feature digit datasets and synthetic mixtures (Table 74).

Table 74: Transplant accuracies on the five datasets with the largest TabICL drop  $\Delta_{ICL}$ .

Dataset	PFN nat.	PFN proto	$\Delta_{PFN}$	ICL nat.	ICL vote	$\Delta_{ICL}$
mfeat-karhunen	0.969	0.161	-0.808	0.984	0.043	-0.941
quadrant_2d	0.992	0.412	-0.580	0.996	0.080	-0.916
mfeat-factors	0.961	0.236	-0.725	0.984	0.089	-0.895
mfeat-pixel	0.962	0.254	-0.709	0.979	0.084	-0.895
semeion	0.909	0.277	-0.632	0.961	0.076	-0.885

**Best-layer transplant.** Picking the layer maximizing held-out accuracy per dataset (best-layer transplant, 49 datasets) shrinks the gap for TabICL ( $-0.395 \rightarrow -0.263$ , acc.  $0.470 \rightarrow 0.601$ ) but widens it for TabPFN ( $-0.331 \rightarrow -0.549$ , acc.  $0.523 \rightarrow 0.305$ ): the prototype-optimal layer is shallow (median 0) where TabPFN representations have not yet specialized.

### I.4 TabPFN L11 kNN agreement (strengthened test)

Restated from §B.2.6 at the readout layer L11 (49 cls  $\times$  5 seeds). Each cell is across-dataset mean kNN agreement with TabPFN.

Table 75: TabPFN kNN agreement at the readout layer L11. Every L11 metric is strictly worse than L9 and worse than input- $\ell_2$  at every  $k$ . The “kNN-on-final-representation” hypothesis remains refuted at the readout layer.

$k$	input- $\ell_2$	rep- $\ell_2$ L9	rep- $\ell_2$ L11	rep-cosine L11	rep-Mahalanobis L11
$k=1$	0.782	0.768	0.528	0.528	0.356
$k=3$	0.800	0.772	0.554	0.554	0.378
$k=5$	<b>0.811</b>	0.774	0.561	0.561	0.395
$k=10$	0.823	0.777	0.572	0.572	0.429

### I.5 TabICL extra-attack robustness

Three perturbations beyond the eight reported in §6. 24 datasets  $\times$  5 seeds;  $\Delta = \text{TabICL} - \text{XGB}$ .

Table 76: TabICL never loses on the mean across the three additional attacks; consistent with the 5-attack ranking in the main text and with the 8-attack panel as a whole.

Attack	TabICL acc	XGB acc	$\Delta$ (mean)	TabICL wins
boundary_poison	0.877	0.840	+0.037	22 / 24
mono_cube	0.886	0.862	+0.023	18 / 24
mono_rank	0.787	0.787	+0.000	16 / 24

### I.6 Column-marginal vs. invariance-cost correlation

Post-hoc, CPU-only computation for §B.3.2. For each dataset compute (i) size of largest column-set with identical 1D marginals at JS tolerance  $\tau \in \{0.01, 0.05, 0.10\}$ , (ii) corresponding invariance-ablation gap. Spearman  $\rho$  across 49 datasets.

Table 77: Spearman correlation between column-marginal-duplication count and per-dataset invariance gap. Only TabICL-v1 no-RoPE exhibits a non-zero population gap that is positively correlated with marginal duplication; TabPFN  $W=0$  is null in both. The JS-screen identifies collapse-prone datasets a-priori.

Model	mean gap	$\rho$ ( $\tau=0.01$ )	$\rho$ ( $\tau=0.05$ )	$\rho$ ( $\tau=0.10$ )
TabPFN $W=0$	-0.0001	+0.042 (p=0.78)	+0.081 (p=0.58)	+0.064 (p=0.66)
TabICL-v1 no-RoPE	+0.1540	+0.201 (p=0.17)	+0.316 (p=0.03)	+0.322 (p=0.02)
TabICL-v2 no-RoPE	+0.0016	+0.231 (p=0.11)	+0.310 (p=0.03)	+0.325 (p=0.02)

### I.7 Collapse $f$ -sweep

Parametric extension of §5.2. Synthesise Qu et al. [2025] style stress data where the fraction  $f \in \{0, 0.25, 0.5, 0.75, 1\}$  of  $d=12$  columns are i.i.d. from a single shared discrete marginal, the remainder from heterogeneous marginals;  $K=5$  classes,  $n=800$  rows, 10 seeds each. Cell entries are paired  $\Delta$  (ablated – full) with bootstrap 95 % CI.

Table 78: Collapse  $f$ -sweep paired  $\Delta$  accuracy. TabICL-v1 no-RoPE falls monotonically with  $f$  (with non-overlapping CIs above  $f=0.25$ ). TabPFN  $W=0$  and TabICL-v2 no-RoPE stay within  $|\Delta| \leq 0.001$ . TabPFN 2nd-slot=0 shows a milder M3-pair-channel load-bearing effect that grows from -0.046 at  $f=0$  to -0.140 at  $f=1$ .

$f$	TabPFN $W=0$	TabPFN 2nd-slot=0	TabICL-v1 no-RoPE	TabICL-v2 no-RoPE
0.00	-0.000 [-0.001, +0.000]	-0.046 [-0.096, -0.004]	<b>-0.255</b> [-0.318, -0.187]	-0.001 [-0.004, +0.001]
0.25	-0.000 [-0.001, +0.001]	-0.017 [-0.041, +0.000]	<b>-0.254</b> [-0.311, -0.190]	-0.000 [-0.001, +0.001]
0.50	-0.001 [-0.002, +0.000]	-0.061 [-0.108, -0.022]	<b>-0.459</b> [-0.474, -0.443]	-0.001 [-0.003, +0.001]
0.75	-0.000 [-0.001, +0.000]	-0.062 [-0.105, -0.021]	<b>-0.469</b> [-0.488, -0.450]	-0.000 [-0.003, +0.002]
1.00	+0.000 [+0.000, +0.001]	<b>-0.140</b> [-0.186, -0.102]	<b>-0.472</b> [-0.489, -0.448]	-0.000 [-0.002, +0.002]

### I.8 Combined within-row ablation on v2 backbones

Each individual within-row ablation on a v2 backbone is load-free (§5.2, Table 78). To test whether v2 carries *redundant* within-row defenses, we ablate both available routes simultaneously, without retraining: TabPFNv2 with  $W=0$  and pair second-slot zeroed; TabICLv2 with RoPE removed and the slots 1, 2 of every  $(B, T, G, 3)$  circular feature group zeroed (slot 0 of each group, the original feature index, is preserved; the trained `in_linear` weights on slots 1, 2 are still applied to zeros). Both ablations are wrapped in `VerifiedPatch`: forward hooks confirm `tf_row.rope` is `None` at every block call and that the post-grouping slots 1: are zero on every forward pass. Twenty seeds with paired-bootstrap CIs over seeds; per-seed re-resampling on the synthetic.

Table 79: Combined within-row ablation on v2 backbones. Each individual ablation is load-free (Table 78); the combined ablations expose latent collapse. TabICLv2 with both within-row routes off lands at the majority baseline on the  $d=12$  balance-like stress, confirming that its individual-ablation “free” result reflected redundancy rather than the absence of a within-row defense. TabPFNv2 with both routes off survives but degrades. Compare to the Mitra row-attention ablation (Table 39,  $0.95 \rightarrow 0.08$ ): Mitra’s single load-bearing mechanism has no architectural fall-back, so its failure mode is below-majority rather than at-majority.

backbone	ablation	dataset	accuracy	$\Delta$ vs. full (95% CI)
TabPFNv2	full	balance-scale	0.962	—
TabPFNv2	$W=0 + 2\text{nd-slot}=0$	balance-scale	0.890	-0.071 [-0.106, -0.044]
TabPFNv2	full	balance-like, $d=12$	0.970	—
TabPFNv2	$W=0 + 2\text{nd-slot}=0$	balance-like, $d=12$	0.855	-0.115 [-0.144, -0.091]
TabICLv2	full	balance-scale	0.978	—
TabICLv2	no-RoPE + no-grouping	balance-scale	0.823	-0.154 [-0.165, -0.144]
TabICLv2	full	balance-like, $d=12$	0.990	—
TabICLv2	no-RoPE + no-grouping	balance-like, $d=12$	<b>0.485</b>	<b>-0.504 [-0.522, -0.474]</b>
majority baseline				0.46/0.47 (balance-scale/like)

### I.9 TabPFN L9 attention as learned similarity

Per test row fit Ridge of L9 column-attention target-row weights onto a four-feature basis  $\{\ell_2, \cos, \ell_1, \text{rep-}\ell_2(L8)\}$ . 49 datasets  $\times$  5 seeds; we report the distribution of per-dataset mean  $R^2$ .

Table 80: TabPFN L9 column-attention is far better explained by the model’s own L8 representation distance ( $R^2=0.48$ ) than by raw input  $\ell_2$  ( $R^2=0.22$ ). Full basis explains  $\sim 60\%$  of attention variance, consistent with “learned similarity” and ruling out a pure  $\ell_2$ -on-inputs mechanism.

Predictor set	mean $R^2$	median	min	max
input $\ell_2$ only	0.218	0.168	0.004	0.774
rep- $\ell_2$ (L8) only	0.477	0.488	0.047	0.788
full 4-feature basis	0.600	0.606	0.149	0.853
gap (full - $\ell_2$ )	+0.382	+0.382	+0.079	+0.765
gap (rep- $\ell_2$ - input- $\ell_2$ )	+0.259	+0.292	-0.167	+0.695

### I.10 Worst-case real-data uniform-attention drop

Re-aggregate per-dataset all-12-block uniform-attention drop on TabICL-cls, excluding synthetic `sign_1d` (48 real datasets).

Table 81: Worst-case drops on real data: top-5 are MiceProtein 0.78, mfeat-karhunen 0.70, mfeat-zernike 0.68, mfeat-morphological 0.64, mfeat-fourier 0.61. The headline mean dilution by easy datasets hides a median drop of 29 pp; the worst-case real drop matches the synthetic Qu drop and is the more honest figure for the distributed-mechanism claim of §C.2.3.

Statistic	median	mean	p75	p90	max
$\Delta$ accuracy (uniform all-12)	0.293	0.290	0.441	0.602	0.777
Threshold	> 0.05	> 0.10	> 0.20	> 0.30	> 0.50
# datasets exceeding	36 / 48	34 / 48	29 / 48	23 / 48	9 / 48

### I.11 Majority-class baseline

Per-dataset majority-class accuracy on the 49-dataset benchmark, broken down by class cardinality.

Table 82: Majority-class trivial baseline. The 10 datasets with majority > 0.7 (pc1 0.93, climate 0.92, pc3 0.90, Is-this-good 0.88, pc4 0.87, MIC 0.85, kc2 0.79, anneal 0.76, blood-tx 0.76, ilpd 0.71) make a kNN agreement of 0.85 on a  $C=2$  near-trivial problem far less informative than the same number on a balanced 10-class mfeat-\* problem (majority 0.105).

Subset	$n$	mean	median	max
All 49 datasets	49	0.499	0.540	0.932
Binary ( $C=2$ )	24	0.684	0.700	0.932
$C=3$	6	0.421	0.387	0.760
Multiclass ( $C \geq 4$ )	19	0.289	0.250	0.847

### I.12 Column-permutation spread (full distribution)

Full distribution of per-dataset best–worst accuracy under arbitrary column permutations, source for Figure 5.

Table 83: Per-dataset accuracy spread under column permutation, 49 datasets. The headline “8.7 pp” is the maximum across datasets; median spread is  $\sim 2.5$  pp for TabPFN/TabICLv1 and 1.5 pp for TabICLv2. Worst-3 datasets per model: TabPFN {cylinder-bands 0.080, tic-tac-toe 0.075, dresses-sales 0.070}; TabICLv1 {random\_labels 0.087, dresses-sales 0.080, hill-valley 0.078}; TabICLv2 {random\_labels 0.087, dresses-sales 0.053, cylinder-bands 0.052}. The typical-case column-invariance is an order of magnitude stronger than the maximum suggests.

Model	median	mean	p75	p90	max	> 1pp	> 2pp	> 5pp
TabPFNV2	0.027	0.029	0.041	0.053	0.080	41	29	6
TabICLv1	0.025	0.029	0.040	0.053	0.087	41	29	7
TabICLv2	0.015	0.019	0.026	0.039	0.087	29	18	3

### I.13 Per-layer kNN agreement curve (TabICL)

Extends §C.3.5 from L11 to all 12 ICL layers using  $k=5$  kNN on 49 datasets  $\times$  5 seeds.

Table 84: TabICL per-layer kNN-against-TabICL agreement and standalone kNN accuracy. Input-space kNN already agrees 0.817; agreement rises monotonically from 0.885 (L0) to 0.936 (L11), an L11-vs-L8 edge of only 1.4 pp. Reframes the L11-kNN claim as continuous refinement rather than a late, sudden re-shaping.

Layer	cosine agree.	cosine kNN acc	$\ell_2$ agree.	$\ell_2$ kNN acc
input ( $\ell_2$ only)	—	—	0.817	—
L0	0.887	0.827	0.885	0.824
L1	0.888	0.826	0.885	0.825
L2	0.891	0.828	0.890	0.827
L3	0.890	0.832	0.886	0.829
L4	0.900	0.837	0.896	0.835
L5	0.900	0.835	0.894	0.832
L6	0.908	0.840	0.901	0.837
L7	0.904	0.839	0.902	0.837
L8	0.924	0.847	0.923	0.847
L9	0.922	0.849	0.924	0.849
L10	0.934	0.855	0.935	0.855
L11	<b>0.936</b>	<b>0.857</b>	<b>0.936</b>	<b>0.856</b>

#### I.14 Readout grid with calibration

Eight readouts  $\times$  five metrics on 49 classification datasets  $\times$  5 seeds. Readouts: native, L9-vote (PFN) / sharp-vote (ICL), L11-prototype, L11-kNN. ECE uses 15 equal-width confidence bins per (dataset, seed); Table 85 reports means over the 49 per-dataset seed means.

Table 85: Per-readout means across 49 datasets (5 seeds / dataset). PFN L9-vote pairs a 5.0 pp accuracy drop with a  $\sim 5\times$  ECE jump and  $\sim 2\times$  NLL: vote sacrifices calibration. ICL native / L11-prototypo / L11-kNN are within 1.0 pp on accuracy, but not on calibration: prototype raises ECE/NLL to 0.463/1.058 and kNN to 0.115/2.840 vs. 0.042/0.303 natively. Both prototype/kNN heads also ruin TabPFN’s calibration (NLL up to 9.7).

Readout	acc	ECE	NLL	macro-P	macro-R
PFN-native	0.854	0.043	0.329	0.806	0.786
PFN L9-vote	0.804	0.201	0.625	0.750	0.724
PFN L11-prototype	0.523	0.277	1.178	0.506	0.572
PFN L11-kNN	0.547	0.371	9.715	0.435	0.522
ICL-native	0.864	0.042	0.303	0.823	0.801
ICL L11-prototype	0.854	0.463	1.058	0.806	0.817
ICL L11-kNN	0.856	0.115	2.840	0.816	0.796
ICL sharp-vote	0.470	0.125	1.094	0.265	0.325

**Dataset-bootstrap calibration intervals.** Treating the 49 per-dataset seed means as the reporting unit, PFN-native vs. PFN L9-vote shifts ECE from 0.043 [0.036, 0.051] to 0.201 [0.176, 0.228] and NLL from 0.329 [0.244, 0.426] to 0.625 [0.521, 0.735]. For TabICL, native vs. L11-prototype shifts ECE from 0.042 [0.034, 0.050] to 0.463 [0.404, 0.522] and NLL from 0.303 [0.219, 0.398] to 1.058 [0.916, 1.208]; the L11-kNN surrogate keeps near-native accuracy but still widens ECE/NLL to 0.115 [0.085, 0.148] and 2.840 [2.019, 3.785]. All intervals are 95% bootstrap CIs over per-dataset seed means.

Table 86: Cross-readout agreement (mean over 49 datasets). The two “native” stacks agree 0.93, but the same surrogate readout produces disjoint predictions across architectures (PFN-proto  $\leftrightarrow$  ICL-proto 0.54). Stacks behave alike at prediction level, not at representation level.

Pair	label agreement
PFN-native vs. ICL-native	0.934
PFN-native vs. PFN L9-vote	0.874
PFN-native vs. PFN L11-proto	0.518
PFN-native vs. PFN L11-kNN	0.555
ICL-native vs. ICL L11-proto	0.922
ICL-native vs. ICL L11-kNN	0.936
ICL-native vs. ICL sharp-vote	0.496
PFN L11-proto vs. ICL L11-proto	0.542
PFN L11-kNN vs. ICL L11-kNN	0.536
PFN L9-vote vs. ICL-native	0.862

### I.15 Subgroup-collapse stress test

Synthetic construction maximally stressing within-group collapse: 12 features in 6 pair-groups of 2, columns within a pair share a marginal, labels depend on within-pair products. 5 seeds.

Table 87: Subgroup-collapse stress: invariance preserved ( $\Delta_{\text{acc}} = 0.001$ ). Train collapse rate is near-zero (0.003); the  $\sim 20\%$  test collapse (cosine  $> 0.99$ ) is a moderate pre-readout phenomenon on heterogeneous queries that does not impair accuracy.

seed	acc full	acc $W=0$	test collapse full	test collapse $W=0$
0	0.725	0.725	0.194	0.191
1	0.760	0.760	0.147	0.140
2	0.810	0.810	0.215	0.209
3	0.645	0.640	0.279	0.289
4	0.710	0.710	0.152	0.152
mean	0.730	0.729	0.198	0.196

### I.16 TabPFN per-head ablation at L8/L9/L10

For each  $L \in \{8, 9, 10\}$  and each of  $H=6$  heads, zero the output-projection slice for head  $h$  at that block; measure per-seed accuracy delta against baseline on 10 datasets  $\times$  5 seeds.

Table 88: Per-block per-head zero-out drop. “# critical” counts heads with  $> 5$  pp drop in a given (dataset, seed). L9 has the largest single-head impact ( $\Delta_{h0}=3.1$  pp on average, max 17.3 pp), but no head dominates: the L9 vote signal is diffuse with a slight head-0 peak rather than localized.

Layer	mean max-drop	worst max-drop	mean # critical	h0	h1	h2	h3	h4	h5
L8	0.031	0.204	0.14	0.008	0.003	0.019	0.000	0.002	-0.000
L9	0.039	0.173	0.32	0.031	0.009	0.004	0.003	0.000	0.000
L10	0.012	0.067	0.08	0.005	0.003	0.002	0.003	0.003	0.001

### I.17 Effective rank vs. number of classes

Per-layer Pearson correlation between #classes  $C$  and post-block effective rank, computed by joining the per-block geometry measurements of §B.1.4 with the per-dataset class counts used in the vote analysis of §B.2.3 (49 classification datasets).

Table 90: Claim / evidence / scope summary for the main mechanistic statements. “Full grid” denotes the 49-dataset classification suite unless the row says otherwise.

Claim	Main evidence in this paper	Scope / caveat
TabPFNv2 late vote readout	L9 is the sharpest layer on 49/49 datasets; vote-model mean $r=0.89$ ; uniform-L9 and block-9 interventions collapse the intact readout.	Full grid; descriptive surrogate only (accuracy 0.804 vs. 0.854, ECE/NLL 0.201/0.625 vs. 0.043/0.329).
TabICLv2 prototype/ $k$ NN readout	L11 prototype/ $k$ NN reach 0.854/0.856 vs. native 0.864; PFN-vote on ICL drops to 0.47; earlier releases keep the same prototype/ $k$ NN-versus-vote ordering.	Full grid across releases; argmax-faithful but not calibration-preserving (ECE/NLL 0.463/1.058 and 0.115/2.840 vs. 0.042/0.303).
Redundant positional components at inference	TabPFNv2 $W=0$ and TabICLv2 no-RoPE preserve the benchmark mean while granting the matching symmetries; synthetic constructions recover the same invariances.	Full benchmark mean plus synthetic checks; inference-only, so “redundant” here means unused by these weights on this benchmark.
Mechanism-grounded robustness	Hub/rank/SVD ordering matches the proposed readouts on the 24-grid; the same trio on the broader mixed16 slice keeps rank as the dominant mixed-type attack and leaves clean tree baselines competitive.	Matched 24-dataset stress test + 16-dataset mixed-type attack extension under the shared ordinalised numeric view; native-categorical tree controls remain clean-only.

Table 89: Per-layer effective rank vs. class count. TabPFN’s L11 effective rank correlates strongly with  $C$  ( $r=0.64$ ), with mean rank rising from 21.1 ( $C\leq 3$ ) to 31.7 ( $C\geq 4$ ). TabICL is already class-aware at L0 and the correlation decays through depth. The “constant low rank” framing in §2.2 is too strong for TabPFN-L11; the L2 anti-correlation in TabPFN is a notable input-projection artefact.

Layer	TabPFN-cls				TabICL-cls			
	$r$	$p$	mean $C\leq 3$	mean $C\geq 4$	$r$	$p$	mean $C\leq 3$	mean $C\geq 4$
L0	-0.29	0.079	55.6	44.3	+0.50	0.000	31.6	49.2
L1	+0.50	0.000	34.9	53.2	+0.51	0.000	38.3	59.5
L2	-0.36	0.012	10.9	9.1	+0.52	0.000	42.8	65.5
L3	-0.26	0.072	20.8	18.6	+0.50	0.000	50.2	73.4
L4	+0.33	0.023	21.0	24.9	+0.48	0.000	54.1	77.7
L5	+0.40	0.004	20.1	24.2	+0.48	0.001	65.2	92.1
L6	+0.48	0.001	21.6	27.7	+0.47	0.001	69.4	97.4
L7	+0.44	0.002	18.7	23.5	+0.46	0.001	77.6	109.0
L8	+0.33	0.020	15.3	17.5	+0.46	0.001	67.0	94.5
L9	+0.46	0.001	20.5	26.5	+0.42	0.002	68.5	94.5
L10	+0.51	0.000	22.3	30.1	+0.36	0.012	61.1	79.7
L11	+0.64	0.000	21.1	31.7	+0.21	0.152	63.0	73.3

### I.18 Faithful-surrogate coverage by regime

The four criteria of §3 are: **(i) Pearson**  $r\geq 0.85$  between the rule’s predicted probabilities and the model’s, evaluated on the held-out test split of each dataset and aggregated as the 49-dataset mean. This tests whether the rule reproduces the model’s *soft* decision shape, not just the argmax. **(ii) accuracy gap**  $\leq 3$  pp between the rule’s accuracy and native model accuracy on the same split, averaged across the 49-dataset suite. This tests whether the rule reproduces the model’s *performance level*, ruling out rules that match distributions on average but lose on hard examples. **(iii) Cohen’s**  $\kappa\geq 0.8$  between the rule’s argmax and the model’s argmax on the held-out test split, computed per dataset and aggregated as the mean across the 49-dataset grid. This is a strict *point-wise* agreement test that penalizes chance-level agreement and rules out a candidate that reaches the right accuracy by hitting different examples than the model does. **(iv) intervention-survival**: the rule must continue to match the model after a causal intervention that preserves only the components it names (e.g. uniformising attention outside L9 for the vote rule, replacing all final-layer features with class means for the prototype rule). This rules out rules that happen to track the model in the unperturbed network but rely on machinery they do not explicitly name.

Table 91 summarizes which readout passes each criterion, broken out by model and regime. Failing criteria are flagged at point of use in the main text rather than collapsed into a universal claim.

Table 91: Where each readout passes the four faithful-surrogate criteria (§3). ✓ pass at the stated cut-off, ~ borderline, × fail (failing statistic in parentheses); *n/a* where the criterion does not apply (e.g.  $\kappa$  on regression). The intervention column gives the observed causal signature.

Model / regime	Rule	(i) $r \geq 0.85$	(ii) $\leq 3$ pp	(iii) $\kappa \geq 0.8$	(iv) intervention
TabPFNV2 cls (binary–mid)	vote@L9	✓ (0.93)	✓ (−0.02)	✓	✓ uniform-attn→maj.
TabPFNV2 cls (10-class)	vote@L9	× (0.71–0.76)	~	~	✓
TabPFNV2 reg	vote (reg)	✓	✓	<i>n/a</i> (reg)	✓
TabICLv1/v1.1/v2 cls	proto@L11	✓	✓ (−0.01)	✓	✓ cross-rule collapse
TabICLv2 reg	lin. proto	×	×	<i>n/a</i> (reg)	✓ ( $\ell_2$ - <i>k</i> NN tracks)
Mitra cls	vote@L9	✓ (0.89)	~ (−4.5)	✓	✓ row-attn KO

**Threshold sensitivity.** We stress the descriptive thresholds in §3 by varying the soft-fidelity (i) and accuracy (ii) cut-offs and recounting populated-rule passes (Table 92); the  $\kappa$  and intervention criteria are binary and not swept. Tightening or loosening either threshold shifts populated-rule counts by a few datasets, and the readout-family verdict (§3.4) does not flip in any of these cells.

Table 92: Faithful-surrogate pass counts as a function of thresholds ( $r$ ,  $\Delta_{\text{acc}}$ ). Cells are *populated-rule* passes (criterion (i) and (ii) only; intervention always passes for these rules). TabPFNV2 vote counts use the 49-dataset population of Table 17 (per-dataset Pearson  $r$  has mean 0.890, sd 0.114); TabICLv2 prototype counts use the 49-dataset population of §C.3.1.

Threshold $r / \Delta$	TabPFNV2 vote (L9)			TabICLv2 prototype (L11)		
	$\leq 5$ pp	$\leq 3$ pp	$\leq 1$ pp	$\leq 5$ pp	$\leq 3$ pp	$\leq 1$ pp
$r \geq 0.80$	43/49	42/49	38/49	46/49	45/49	41/49
$r \geq 0.85$	41/49	40/49	36/49	44/49	43/49	40/49
$r \geq 0.90$	37/49	36/49	32/49	41/49	41/49	38/49

### I.19 Global BH-FDR summary across headline rejections

This subsection delivers a joint Benjamini–Hochberg FDR check at  $q=0.05$  across the 30 headline rejections of §2–§6, alongside the within-family multiplicity controls already used in the body (Holm across the eight attacks per model in §6; Bonferroni on the 10 regression tests; TOST equivalence margins pre-specified for the invariance claim). The list comprises: the L8→L9 probe-accuracy jump, the per-block knockout  $p$ -values for blocks  $\{0, 5, 9\}$  in TabPFNV2 and  $\{\text{ColEmb-2, ICL-0, ICL-6, ICL-11}\}$  in TabICLv2 (7 tests), the cross-rule sign tests (PFN→ICL, ICL→PFN; 2), the fresh-head asymmetry on each backbone (2), the per-version prototype/vote ordering tests across v1, v1.1, v2 (3), the  $W=0$  and no-RoPE TOST equivalences (2), and the 16 per-attack  $\Delta$  tests (eight attacks  $\times$  two FMs).

All 30 rejections survive BH-FDR at  $q=0.05$  (largest  $p < 10^{-3}$  in the list passing BH; the marginal cases are the TabICLv2 `cube_warp` and `centroid_inj` entries which are reported as *non*-rejections in Table 3 and are not in the headline list). The within-family Holm decisions in Table 3 are therefore consistent with the global BH picture; no additional headline finding flips sign or loses significance under joint control. We note that BH-FDR on 30 tests with this many small  $p$ -values is a weak sieve in practice; the more informative discipline remains the local Holm/Bonferroni choices already in the body.

### I.20 Serving-cost ledger

Per-query latency and peak GPU memory are reported in Table 5; the corresponding throughput on a single H100-NVL is  $\approx 1$  query/s for TabPFNV2 and  $\approx 0.7$  query/s for TabICLv2 when each query is served as its own forward pass. Both backbones allow batched query forwards over a fixed context: amortizing 32 queries per context pass on H100 raises throughput to  $\approx 18$  queries/s for TabPFNV2 and  $\approx 12$  queries/s for TabICLv2 at peak memory  $\approx 6$  GiB (TabPFNV2) and  $\approx 8$  GiB (TabICLv2); above this batch the attention-cost term dominates and throughput plateaus. The OvA class-invariance wrapper of §4 multiplies wall-clock by  $C$  and peak memory by  $C$  when the  $C$  binary re-encodings are run independently; on the  $C=10$  `mfeat-*` tasks this is  $\approx 10$  s and  $\approx 30$  GiB per query batch. Memory rather than wall-clock is the limiting factor; on a single 24 GiB consumer

card the OvA wrapper does not fit at  $C \geq 8$  without query-batch reduction. The  $W=0$  and no-RoPE patches change neither wall-clock nor peak memory at any batch size we measured (§4).

## J Robustness to context size

Across the context sizes we evaluated ( $n \in \{1000, 1500\}$  on six OpenML datasets with native size  $> 1500$  rows), the readout and invariance findings of §3 and §4 are unchanged: vote and prototype fidelities and column-permutation spread are statistically indistinguishable across the two context sizes (Table 93). We re-run the attention-weighted L9 vote for TabPFNv2, the nearest-prototype rule in the final representation for TabICLv2, and the column-permutation invariance probe at both context sizes.

**Setup.** Six OpenML datasets have native size above 1500 rows: `car` (1728), `Is-this-a-good-customer` (1723), `steel-plates-fault` (1941), `mfeat-morphological` (2000), `mfeat-fourier` (2000), `red_wine` (1599). For each (dataset,  $n_{\text{train}}$ , seed) cell we hold out 200 stratified test rows and subsample the remaining pool to  $n_{\text{train}}$  without replacement; `red_wine` caps at  $n = 1399$ . Each cell is run with five seeds. Vote and prototype fidelities are top-1 agreement with the native model prediction. Column-permutation spread is the  $\max - \min$  accuracy across eight independently sampled random column orderings.

Table 93: Scale audit on six OpenML datasets with native size  $> 1500$  rows. Vote fidelity (TabPFNv2) and prototype fidelity (TabICLv2) are top-1 agreement with the native model prediction (mean $\pm$ std over 5 seeds). Col-perm spread is  $\max - \min$  accuracy over 8 random column permutations.

Model	Dataset	$n_{\text{train}}$	Fidelity (mean $\pm$ std)	Col-perm spread
TabPFNv2	Is-this-a-good-customer	1000	0.996 $\pm$ 0.004	0.000
TabPFNv2	Is-this-a-good-customer	1500	0.986 $\pm$ 0.009	0.000
TabPFNv2	car	1000	0.953 $\pm$ 0.018	0.012
TabPFNv2	car	1500	0.970 $\pm$ 0.016	0.011
TabPFNv2	mfeat-fourier	1000	0.789 $\pm$ 0.048	0.022
TabPFNv2	mfeat-fourier	1500	0.788 $\pm$ 0.023	0.022
TabPFNv2	mfeat-morphological	1000	0.753 $\pm$ 0.048	0.020
TabPFNv2	mfeat-morphological	1500	0.816 $\pm$ 0.044	0.011
TabPFNv2	red_wine	1000	0.803 $\pm$ 0.030	0.025
TabPFNv2	red_wine	1399	0.798 $\pm$ 0.027	0.027
TabPFNv2	steel-plates-fault	1000	0.728 $\pm$ 0.038	0.022
TabPFNv2	steel-plates-fault	1500	0.745 $\pm$ 0.037	0.022
TabICLv2	Is-this-a-good-customer	1000	0.963 $\pm$ 0.019	0.000
TabICLv2	Is-this-a-good-customer	1500	0.947 $\pm$ 0.044	0.003
TabICLv2	car	1000	0.989 $\pm$ 0.004	0.006
TabICLv2	car	1500	0.996 $\pm$ 0.004	0.004
TabICLv2	mfeat-fourier	1000	0.946 $\pm$ 0.012	0.010
TabICLv2	mfeat-fourier	1500	0.958 $\pm$ 0.012	0.014
TabICLv2	mfeat-morphological	1000	0.869 $\pm$ 0.032	0.007
TabICLv2	mfeat-morphological	1500	0.862 $\pm$ 0.039	0.009
TabICLv2	red_wine	1000	0.836 $\pm$ 0.043	0.012
TabICLv2	red_wine	1399	0.858 $\pm$ 0.020	0.011
TabICLv2	steel-plates-fault	1000	0.932 $\pm$ 0.024	0.023
TabICLv2	steel-plates-fault	1500	0.923 $\pm$ 0.020	0.020
<i>Marginals over (model, n):</i>				
TabPFNv2	all six datasets	1000	0.837 $\pm$ 0.107	0.017
TabPFNv2	all six datasets	1500	0.860 $\pm$ 0.103	0.015
TabICLv2	all six datasets	1000	0.923 $\pm$ 0.059	0.010
TabICLv2	all six datasets	1500	0.924 $\pm$ 0.054	0.010

Vote and prototype fidelities are stable across  $n$ , and the column-permutation spread does not grow with  $n$ . The readout characterizations of §3 and the invariance results of §4 extend to the larger context size.

## K Probe $\ell_2$ -regularization sensitivity (C3)

The main-text per-layer linear probe in §2.1 is reported at  $\ell_2$  regularization  $C=1$ . We check whether the qualitative findings — in particular the sharp L8  $\rightarrow$  L9 crystallization in TabPFNv2 — depend on this choice.

We re-fit the per-layer logistic probe with  $C \in \{0.01, 0.1, 1, 10, 100\}$  on the 45-dataset suite, with 5 seeds per (dataset, layer,  $C$ ) cell. Frozen activations are identical across  $C$  values, so the only varying quantity is the  $\ell_2$  penalty applied during the probe fit. Aggregate per-layer accuracies are in Table 94.

**Aggregate result.** Across the  $45 \times 13 \times 5 \times 5 = 14,625$  (dataset, layer, seed,  $C$ ) cells, the mean per-layer accuracy at  $C=1$  is within 0.012 of the mean accuracy at  $C \in \{0.1, 10\}$  on every layer, and the L8  $\rightarrow$  L9 jump is preserved at every  $C \in \{0.01, 0.1, 1, 10, 100\}$  (jump magnitude 0.291–0.321 across  $C$ , with the smallest gap at  $C=1$ ). Even the most strongly regularized  $C=0.01$  probe recovers the same step (input 0.44, L8 0.48, L9 0.80), so the late-stack crystallization is a property of the representation rather than of the probe fit. We therefore report  $C=1$  in the main text without loss of generality.

Table 94: C3: per-layer linear-probe accuracy on TabPFNv2, averaged over 45 datasets and 5 seeds, for each  $\ell_2$  regularization strength  $C$ .

layer	$C=0.01$	$C=0.1$	$C=1.0$	$C=10.0$	$C=100.0$
input	0.437	0.396	0.388	0.396	0.397
L0	0.326	0.304	0.296	0.296	0.295
L1	0.340	0.322	0.310	0.310	0.310
L2	0.306	0.275	0.275	0.277	0.277
L3	0.490	0.448	0.448	0.447	0.447
L4	0.539	0.531	0.527	0.518	0.500
L5	0.458	0.450	0.446	0.446	0.448
L6	0.492	0.455	0.455	0.450	0.450
L7	0.484	0.476	0.465	0.455	0.453
L8	0.483	0.481	0.480	0.477	0.460
L9	0.804	0.778	0.771	0.773	0.772
L10	0.802	0.795	0.790	0.788	0.784
L11	0.621	0.615	0.623	0.623	0.609

## L Head-capacity saturation curve on TabPFNv2 L12 (C2)

We measure the held-out test accuracy of fresh-fit heads attached to the frozen TabPFNv2 stack at the top-of-stack representation (L12, target column), as the head capacity is varied. Heads:

- **Linear** —  $\ell_2$ -regularized logistic regression.
- **MLP-1** — one hidden layer (64 units, GELU).
- **MLP-2** — two hidden layers (128, 64).
- **MLP-3** — three hidden layers (256, 128, 64).
- **MLP-4** — four hidden layers (512, 256, 128, 64).
- **Kernel SVM** — RBF SVM on a 32-dim PCA projection.

We report mean test accuracy across one context-shuffling seed on a 10-dataset subset of the suite. The protocol mirrors `h6_probe_ladder` from `tab_inv.hardening_experiments`. Per-dataset numbers are in Table 95.

**Result.** The linear head attains the highest mean accuracy (0.719); MLP capacity does not help (MLP-1 0.695, MLP-2 0.591, MLP-3 0.601, MLP-4 0.587), and the RBF kernel SVM is the worst fresh-head (0.406). The non-monotonicity across MLP depth is consistent with overfitting on a representation in which the relevant class signal is already linearly readable; the kernel-SVM gap is consistent with a representation whose useful directions are not preserved under PCA-32 + RBF. In

other words, the L12 representation of TabPFNv2 does not contain additional non-linearly extractable class structure beyond what a linear head recovers.

Table 95: C2: held-out test accuracy of fresh heads at TabPFNv2 L12 (top-of-stack) across head capacities, on 10 datasets (1 seed).

dataset	chance	Linear	MLP-1	MLP-2	MLP-3	MLP-4	Kernel SVM
LED-display-domain-7di	0.10	0.250	0.160	0.110	0.180	0.150	0.110
balance-scale	0.33	0.664	0.768	0.728	0.640	0.368	0.464
banknote-authenticatio	0.50	0.996	1.000	0.924	0.713	1.000	0.556
blood-transfusion-serv	0.50	0.760	0.760	0.760	0.240	0.240	0.760
breast_cancer	0.50	0.965	0.956	0.368	0.965	0.965	0.368
dresses-sales	0.50	0.580	0.580	0.580	0.460	0.580	0.420
iris	0.33	0.667	0.667	0.667	0.967	0.667	0.333
mfeat-factors	0.10	0.670	0.757	0.287	0.530	0.515	0.205
mfeat-fourier	0.10	0.690	0.665	0.655	0.730	0.662	0.453
wine	0.33	0.944	0.639	0.833	0.583	0.722	0.389
mean	0.33	0.719	0.695	0.591	0.601	0.587	0.406

## M Native-categorical GBDT under the eight perturbations (C6)

The main-text attack tables (§H.3, §H.4, §H.2) compare against ordinal-encoded GBDT/XGBoost baselines; here we additionally report CATBOOST, XGBOOST, and LIGHTGBM with native categorical handling on the mixed-type subset of the perturbation grid (16 OpenML datasets with at least one categorical column).

The eight perturbations are the same as in the main text: pad-2x, pad-4x, boundary, hub-poison, centroid-injection, mono-cube, mono-softexp, and mono-rank.

Table 96: C6: mean test accuracy across the mixed-type OpenML subset ( $N=16$  datasets) for native-categorical GBDTs under the eight perturbations. CatBoost’s `cat_features` interface rejects float-typed arrays produced by the non-monotone perturbations, so its row only contains values for the three numeric mono-\* perturbations.

backend	orig	pad-2x	pad-4x	bound	hub	centr	m-cube	m-sexp	m-rank
CatBoost	–	–	–	–	–	–	0.774	0.760	0.662
XGBoost	0.759	0.742	0.742	0.741	0.710	0.759	0.762	0.762	0.623
LightGBM	0.761	0.748	0.742	0.749	0.709	0.763	0.763	0.756	0.654

**Result.** The qualitative pattern matches the main-text ordinal-encoded baseline: the smooth monotone-feature attacks (MONO-CUBE, MONO-SOFTEXP) and the geometric perturbations (pad-2x, pad-4x, centroid-injection) leave native-cat GBDTs essentially at *orig* accuracy, while HUB-POISON ( $-0.05$  for both backends able to score it) and MONO-RANK ( $-0.14$  for XGBoost,  $-0.11$  for LightGBM) cause the largest drops. CATBOOST rejects pure-numeric arrays under `cat_features`, so its row only contains values for the three purely numeric mono-\* perturbations; for those, CATBOOST behaves comparably to the other two backends.